Current Biology

Article

A 50-million-year-old, three-dimensionally preserved bat skull supports an early origin for modern echolocation

Graphical abstract

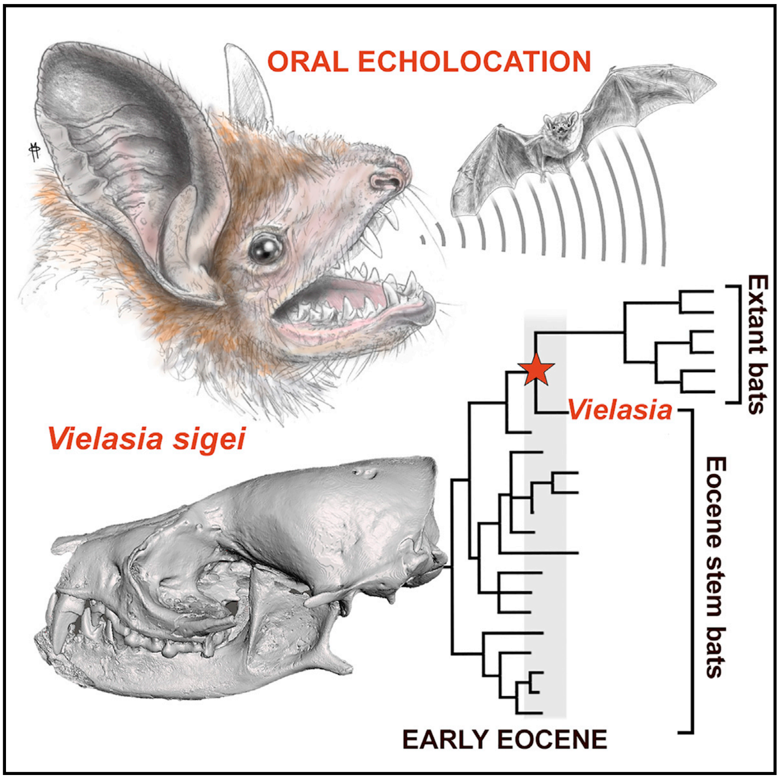

Highlights

- A new bat species is described from a 50-million-year-old cave deposit in France
- Its well-preserved fossils include the oldest uncrushed skull of a bat yet known
- This stem bat appears to have been capable of advanced (laryngeal) echolocation
- The fossils suggest that advanced echolocation predates the crown bat radiation

Authors

Suzanne J. Hand, Jacob Maugoust, Robin M.D. Beck, Maeva J. Orliac

Correspondence

r.m.d.beck@salford.ac.uk

In brief

When and how echolocation first evolved in bats is contentious. Hand et al. report on an uncrushed, 50-million-year-old bat skull that provides significant new data to inform the debate. Measurements of the inner ear of the French stem bat *Vielasia* suggest that advanced (laryngeal) echolocation may have evolved before the crown bat radiation.

Hand et al., 2023, Current Biology *33*, 4624–4640
November 6, 2023 © 2023 The Author(s). Published by Elsevier Inc.
https://doi.org/10.1016/j.cub.2023.09.043

CellPress
OPEN ACCESS

Current Biology

Article

A 50-million-year-old, three-dimensionally preserved bat skull supports an early origin for modern echolocation

Suzanne J. Hand,[1,4] **Jacob Maugoust,**[2] **Robin M.D. Beck,**[3,5,6,*] **and Maeva J. Orliac**[2]
[1]ESSRC, School of Biological, Earth and Environmental Sciences, University of New South Wales, Sydney, NSW 2052, Australia
[2]Institut des Sciences de l'Evolution, UMR 5554 CNRS, IRD, EPHE, Université de Montpellier, Place Eugène Bataillon, 34095 Montpellier Cedex 5, France
[3]School of Science, Engineering and Environment, University of Salford, Manchester M5 4WT, UK
[4]Senior author
[5]X (formerly Twitter): @robinmdbeck
[6]Lead contact
*Correspondence: r.m.d.beck@salford.ac.uk
https://doi.org/10.1016/j.cub.2023.09.043

SUMMARY

Bats are among the most recognizable, numerous, and widespread of all mammals. But much of their fossil record is missing, and bat origins remain poorly understood, as do the relationships of early to modern bats. Here, we describe a new early Eocene bat that helps bridge the gap between archaic stem bats and the hyperdiverse modern bat radiation of more than 1,460 living species. Recovered from ~50 million-year-old cave sediments in the Quercy Phosphorites of southwestern France, *Vielasia sigei*'s remains include a near-complete, three-dimensionally preserved skull—the oldest uncrushed bat cranium yet found. Phylogenetic analyses of a 2,665 craniodental character matrix, with and without 36.8 kb of DNA sequence data, place *Vielasia* outside modern bats, with total evidence tip-dating placing it sister to the crown clade. *Vielasia* retains the archaic dentition and skeletal features typical of early Eocene bats, but its inner ear shows specializations found in modern echolocating bats. These features, which include a petrosal only loosely attached to the basicranium, an expanded cochlea representing ~25% basicranial width, and a long basilar membrane, collectively suggest that the kind of laryngeal echolocation used by most modern bats predates the crown radiation. At least 23 individuals of *V. sigei* are preserved together in a limestone cave deposit, indicating that cave roosting behavior had evolved in bats by the end of the early Eocene; this period saw the beginning of significant global climate cooling that may have been an evolutionary driver for bats to first congregate in caves.

INTRODUCTION

Bats are one of the most speciose and ecologically diverse mammalian orders, representing one-fifth of all mammals alive today (>1,460 species[1]). They are the only mammals to use powered flight, and many bats (but not flying-foxes or Old World fruit bats) use echolocation calls produced in the larynx to orientate in darkness and find food. These two key biological innovations make bats morphologically highly distinctive in their skeletons and skulls, and molecular data suggest they diverged from other mammals more than 60 million years ago (mya).[2–6]

When and how flight and echolocation evolved in bats is contentious. It has been argued that powered flight evolved before echolocation in bats,[7–9] that echolocation came first,[10] or that powered flight and echolocation evolved in tandem.[11] Today, all bats fly, but not all bats echolocate. Old World fruit bats and flying-foxes (Pteropodidae, suborder Yinpterochiroptera) do not use laryngeal echolocation, unlike the other ~86% of extant bats, which utilize high-frequency sounds produced by the larynx to echolocate. There is debate about when and how laryngeal echolocation evolved in bats, with two specific hypotheses debated: (1) that laryngeal echolocation evolved independently within the two bat suborders Yinpterochiroptera and Yangochiroptera (e.g., Teeling et al.[12] and Nojiri et al.[13]) or (2) that laryngeal echolocation evolved once in the common ancestor of extant bats but was subsequently lost in some yinpterochiropterans (i.e., pteropodids; e.g., Simmons et al.,[9] Springer et al.,[14] Teeling,[15] and Liu et al.[16]). A range of morphological, genomic, anatomical, phylogenetic, developmental, physiological, and behavioral data has been used to support both alternatives (e.g., Nojiri et al.,[13] Liu et al.,[16] Eick et al.,[17] Veselka et al.,[18] Davies et al.,[19] Teeling et al.,[20] Wang et al.,[21] and Thiagavel et al.[22]).

The bat fossil record also provides significant evolutionary insights, although it is one of the poorest of any mammalian order, with ~80% of the record estimated to be missing.[8,23,24] The world's oldest known bat fossil consists of a single, 56 mya lower molar from Portugal.[25–27] Another fifty other early to middle Eocene bats are known globally.[24] These are referred to several extinct families, but most are known from fragmentary dental remains, and their relationships to modern bats remain poorly understood. Current evidence indicates that these early bats fall outside the crown clade,[28–33] with the first definitive representatives of modern bat families appearing in the fossil record from ~50 mya (MP10).[30,34,35]

A few early and middle Eocene stem bats are represented by whole-bodied remains preserved in oil shales from lacustrine Konservat-Lagerstätten such as Green River, Wyoming, USA, and Grube Messel, Darmstadt, Germany. Although flattened, they provide fine details of the cranium, postcranium, and soft tissues.[9,36–40] For these rare early bats, a range of echolocation capabilities has been argued on the basis of cochlea size, the shape of the orbicular process of the malleus, and stylohyal morphology[9,18,40–47]—from the absence of laryngeal echolocation in the 52 mya *Onychonycteris finneyi*[9,48] (but see Veselka et al.[18]) to near-modern capabilities in 48 mya *Hassianycteris* and *Palaeochiropteryx* species.[47] However, it has also been suggested, on the basis of inner ear embryology in extant bats, that stem bats may have used a primitive type of echolocation different from the sophisticated system used by modern echolocating bats.[13] For early Eocene bat fossils, common preservation artifacts, such as flattening, fracturing, disarticulation, and deformation, complicate interpretations of the spatial relationships of delicate bones and, in turn, echolocation abilities.[18,48]

Here we describe a new, three-dimensionally preserved fossil bat recovered from 50-million-year-old limestone cave sediments at Vielase, in the Quercy Phosphorites, southwestern France. The fossil fauna from the Vielase deposit is biocorrelated as late early Eocene in age, European reference level MP10,[49–53] which is ~2 million years younger than the Green River bats and ~1 million years older than those from Messel.[53] It is the first stem bat described from cave (rather than lake, river, or estuarine) sediments, a depositional environment that has resulted in three-dimensional (3D), unflattened preservation of its remains. The new bat is described on the basis of a damaged but uncrushed skull preserving the petrosal, as well as a rostrum, premaxilla, maxillae, dentaries, isolated teeth, and skeletal elements. Morphological and total evidence phylogenetic analyses consistently place the new taxon outside modern (= crown group) bats, with our dated total evidence analysis (the result of which we consider to be the most robust[54,55]) placing it sister to the crown bats. This fossil taxon provides significant new information about the echolocation capabilities of an early Eocene stem bat and the early evolutionary history of modern bat echolocation.

RESULTS AND DISCUSSION

Systematic paleontology

Order Chiroptera Blumenbach, 1779

Family indeterminate

Vielasia gen. nov.

Type species. *Vielasia sigei* sp. nov.

Generic diagnosis. As for the type species until others are recognized.

Generic etymology. From the type locality Vielase.

Geological setting. Vielase is among the oldest fossil deposits identified in the karstic terrane of the Quercy Phosphorites, southwestern France.[50,56,57] The Vielase fossils were extracted from a russet-colored bone breccia and a light-colored limestone by acid processing.[50,58] More than 400 bat specimens referable to *Vielasia sigei* were recovered, with the most complete specimens (including the holotype cranium UM-VIE-250) being extracted from the light-colored limestone (B. Marandat, personal communication). Taphonomically, these bat fossils are consistent with *in situ* accumulation in a cave;[59,60] the remains are well preserved but dissociated and include 3D-preserved cranial and postcranial specimens representing multiple individuals, with teeth and bones unworn and without rounding or size filtering indicative of transport, nor evidence of digestion or accumulation by (e.g.) predatory birds. Much rarer rodent, primate, and carnivorous mammal fossils recovered from the site[50] have been used to biocorrelate the deposit as reference level MP10 in the European Palaeogene mammal biostratigraphy.[49–52]

Vielasia sigei sp. nov. [urn:lsid:zoobank.org:pub:C9B0AACD-3581-45A3-BB31-36505D03C788]

Synonymy. Archaeonycteridae gen. et sp. indet. in Sigé[58] and in Legendre et al. (see figure 7)[50]

Type locality and age. Vielase locality, Quercy Phosphorites, southwestern France; late Ypresian, early Eocene (MP10, ~50–49 mya).[50–53]

Holotype. Université de Montpellier (formerly Université de Montpellier 2), UM-VIE-250, near-complete cranium with left P3–M3, right P4–M3, root of LC1, and right petrosal; length 18.29 mm (Figures 1, 2, 3, 4, and S1; Table 1; Data S1A and S1F).

Paratypes and referred specimens (Figures 1, 2, 4, and S1; Table 1; Data S1A). Paratypes: UM-VIE-251, rostrum with right (R) C1–M3 and left (L) P3–M2; UM-VIE-252, right maxilla with C1, P3–M3, and alveolus for P2; UM-VIE-668, left premaxilla with I1-2; UM-VIE-254, partial left dentary with c1, p3–m3, and alveoli for i1-3 and p2; UM-VIE-255, left dentary with p3–m3 and ascending ramus; UM-VIE-614, left p2; UM-VIE-669, left petrosal; UM-VIE-670, left petrosal; UM-VIE-671, left scapula fragment; UM-VIE-672, right proximal humerus; UM-VIE-673, left distal humerus; UM-VIE-674, left proximal radius; VIE-675, left proximal femur; UM-VIE-676, right distal radius; UM-VIE-677, left proximal femur. Additionally, UM-VIE-17, right dP4; UM-VIE-02, right dp4; UM-VIE-20, right m1 or m2; UM-VIE-19, left M1 (figured by Sigé,[58] see figures 1–4 therein). Referred specimens: UM-VIE-270–UM-VIE-566, UM-VIE-605, UM-VIE-608, and isolated teeth (see STAR Methods and Data S1A). Paratype and referred specimens are known only from the type locality.

Specific etymology. In honor of French paleontologist Dr Bernard Sigé, in recognition of his outstanding contribution to the study of fossil bats, including the Vielase bat described here.

Diagnosis. Cranium small (length without prexmaxilla = 18.29 mm), dorsoventrally flat profile, and without anteriorly inflated braincase; premaxilla proclivous, loosely attached (unfused) to maxilla, nasal process present, and palatine process not well developed; weak but present anterolateral rostral inflations, supraorbital ridges, and postorbital processes; supraorbital foramina opening into two anteriorly directed grooves; sagittal crest low anteriorly and reaching maximum height at posteriormost point; lambdoidal crest distinct; rostrum narrows anteriorly from level of C1–P4; large infraorbital foramen dorsal to P4; orbit large and deeply excavated anteriorly; basisphenoid pit(s) absent; petrosal loosely attached, cochlea relatively expanded, ratio of cochlear width to basicranial width ~0.25,

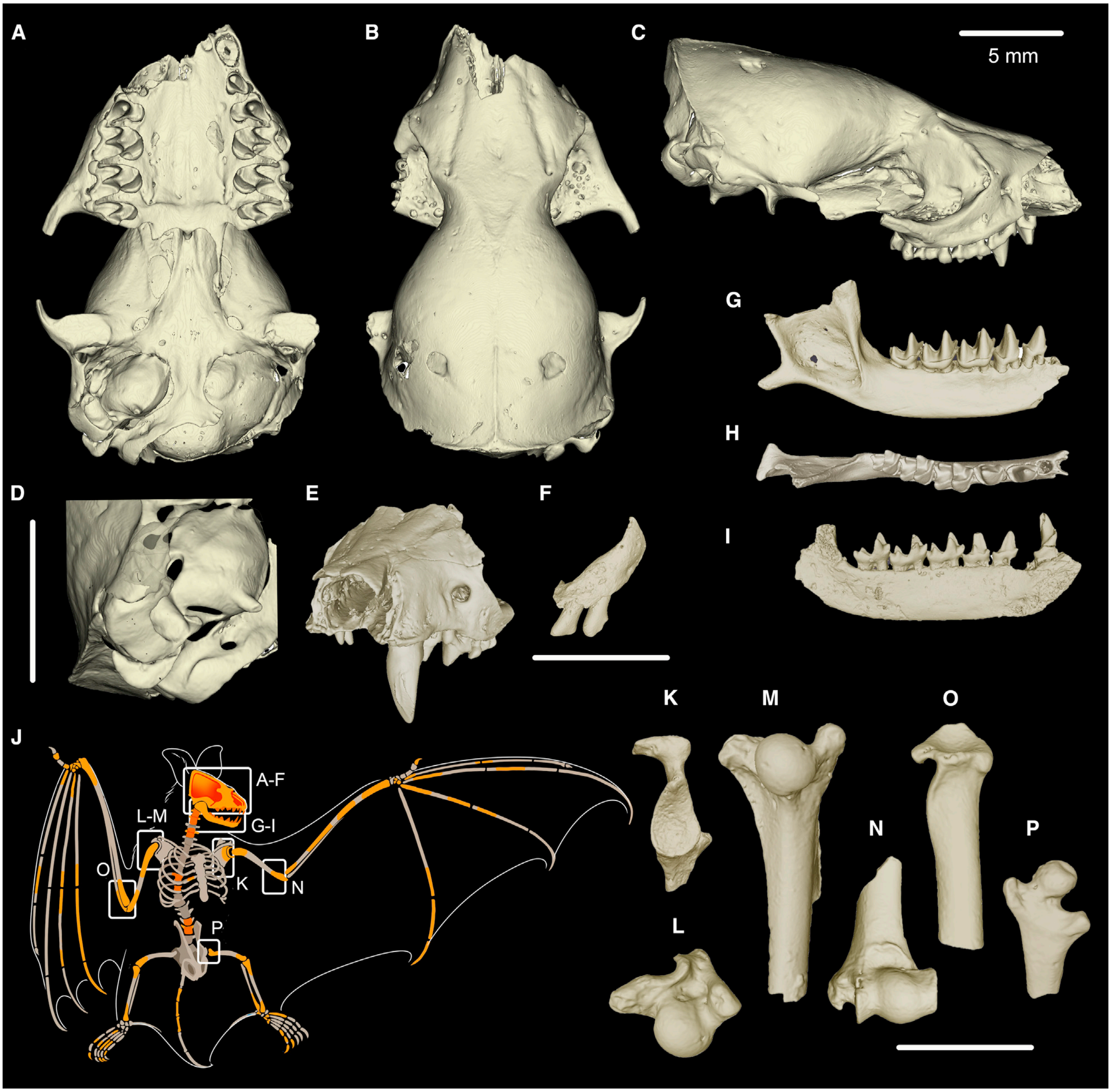

Figure 1. ***Vielasia sigei*** **n. gen. et sp.**
(A–D) UM-VIE-250, holotype, ventral, dorsal, lateral, and petrosal region.
(E) UM-VIE-251, rostrum.
(F) UM-VIE-668, premaxilla with upper incisors.
(G and H) UM-VIE-254, dentary, buccal, and occlusal views.
(I) UM-VIE-255, dentary and lingual view.
(J) Indicative skeletal elements represented in the fossil sample (orange); letters refer to figured specimens.
(K) UM-VIE-671, scapula, glenoid fossa.
(L and M) UM-VIE-672, proximal humerus.
(N) UM-VIE-673, distal humerus.
(O) UM-VIE-674, proximal radius.
(P) UM-VIE-275, proximal femur.
All scale bars, 5 mm.
Diagram by N.P. Archer.
See also Figure S1 and Data S1.

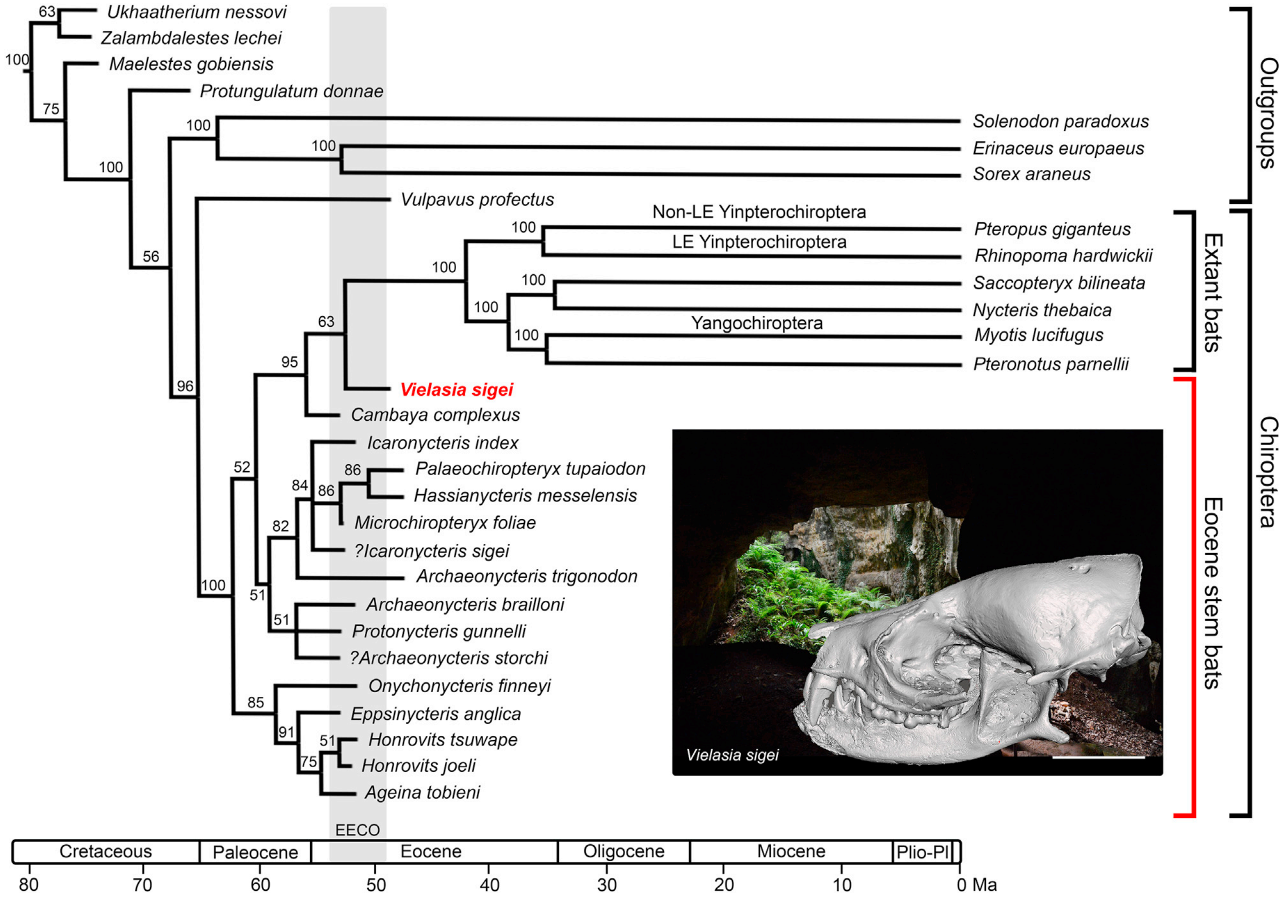

Figure 2. Phylogenetic relationships of *Vielasia sigei* among bats

Consensus tree of post-burn-in trees from Bayesian-dated total evidence analysis of 2,665 craniodental characters plus 36,860 base pairs of DNA sequence data from 27 nuclear loci from O'Leary et al.[61] Values at nodes represent Bayesian posterior probabilities. 3D model of *Vielasia sigei* cranium (compiled from UM-VIE-250, 251, and 268) and mandible (from UM-VIE-254 and 255), see STAR Methods.

Abbreviations: EECO, early Eocene climate optimum (53.26–49.14 mya[62]); LE, laryngeally echolocating; mya, million years ago.

Background photo, Causses du Quercy, P. Lasvenes.

Scale bar, 5 mm.

See also Figure S2 and Data S1 and S2.

2.25 turns in the cochlea, cochlear canal decipherable through petrosal bone, and secondary bony lamina extending almost to canal apex; mastoid not completely covered by paroccipital and supraoccipital; mandible with tall ascending ramus, anterior margin of coronoid process nearly vertical, and height at least twice tooth crown height; angular process at level of tooth alveoli, digit-shaped, and slightly flared laterally; condylar process well dorsal to tooth row; horizontal ramus uniform in depth; anterior mental foramen ventral to incisors, very large, and round; lateral mental foramen large and ventral to p2 or c1–p2; and mandibular foramen ventral to tooth row, elongate.

Relatively complete, unspecialized dentition, with molariform dP4/4. Adult dental formula I2/3 C1/1 P2/3 M3/3; I1-2 tall, stiletto-like, without cingula, and weakly bilobed; C1 anteroposteriorly elongate, with single vertical cusp, rounded buccal and subplanar lingual faces separated by crests, cingulum discontinuous, and attenuated buccally; P2 usually absent (peg-like if present, as in UM-VIE-252); P3 large, with single cusp, and three roots; P4 with three roots, wider than long, T-shaped in occlusal view, with tall paracone, and low expanded lingual lobe with small protocone; M1–M2 wider than long, with large protocone, lingually expanded heel, deep and wide single ectoflexus between parastyle and metastyle, lacking cuspidate mesostyle and hypocone, and paraloph and metaloph variably present; M3 with paracone, small metacone and protocone, three buccal crests only (lacking postmetacrista), and similar in width to M2; lower incisors small, tri-lobed; c1 with posteriorly extended heel, cingulum well-developed lingually, absent buccally, and small cingular cuspid posteriorly; p4 > p3 > p2; p4 with small but distinct metaconid and paraconid, with tall entocristid-like crest from metaconid to posterolingual cingulid and cuspid, and short talonid with narrow groove or basin perpendicular to tooth row; m1–m3 nyctalodont (postcristid links hypoconid directly to hypoconulid, isolating entoconid), talonid cusps all cuspidate, trigonid cusps taller than talonid cusps, protoconid and metaconid similar in height, and trigonid and talonid similar in width; cristid obliqua joins postvallid (posterior face of

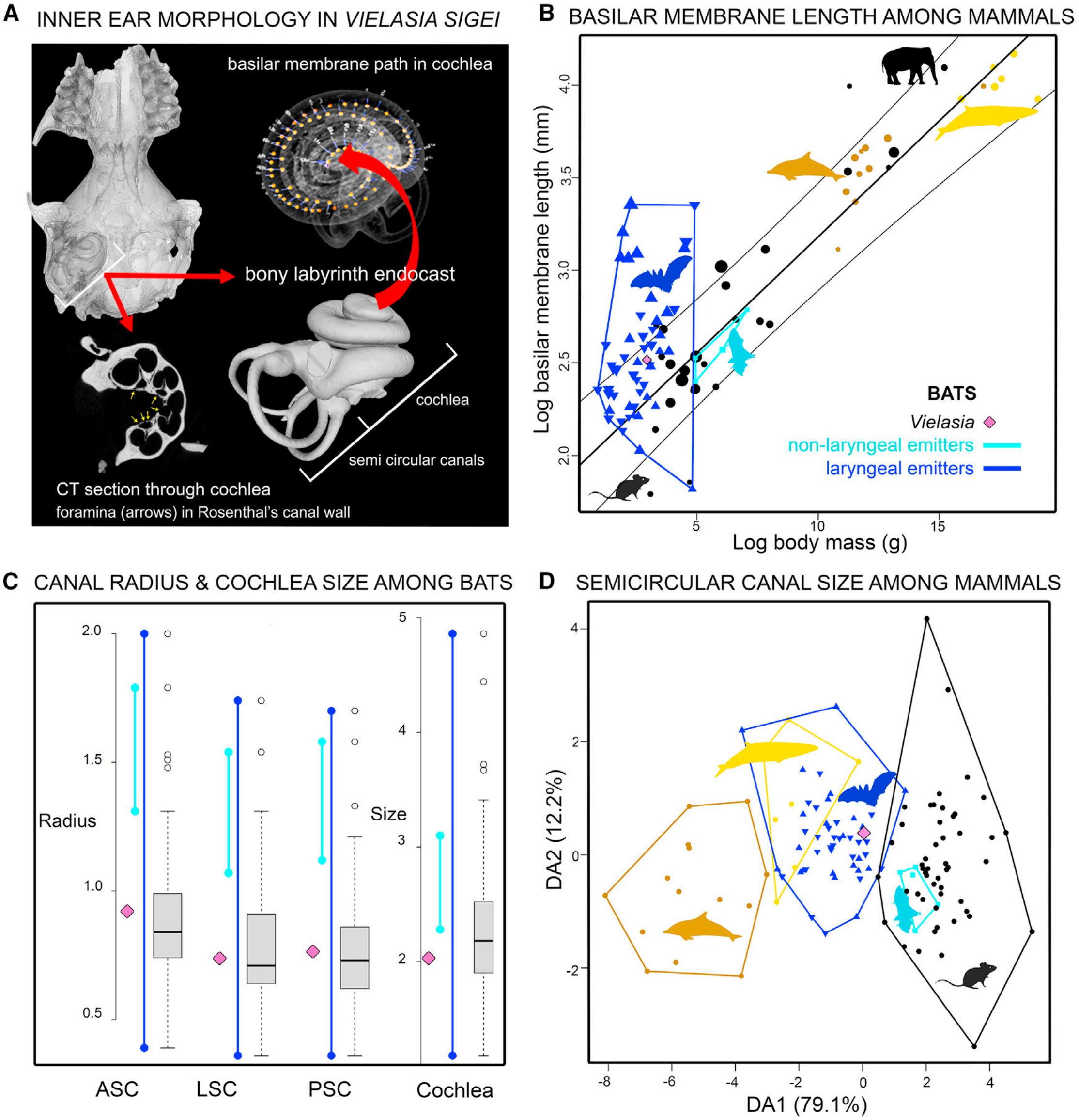

Figure 3. Inner ear attributes in *Vielasia sigei* compared with extant bats and other mammals

(A) Virtual models of *Vielasia sigei* (clockwise from top left): ventral cranium with right petrosal *in situ*; basilar membrane path within cochlea; endocast of right bony labyrinth; and CT slice through modiolar section of cochlea showing foramina (arrows) in bony wall of Rosenthal's canal.

(B) Log basilar membrane length (mm) vs. log body mass (g) in extant mammals, with symbol size proportional to the degree of cochlear coiling; phylogenetic generalized least squares (PGLS) regression line with 95% prediction intervals for mammals (Data S1G; see also Figure S3A).

Color key for (B)–(D): aqua, non-laryngeally emitting bats (pteropodids); dark blue, laryngeally emitting bats (triangles, nasal emitters; inverted triangles, oral emitters); tan, high-frequency-hearing cetaceans; yellow, low-frequency-hearing cetaceans; black, other mammals; pink diamond, *Vielasia sigei*.

(C) Semicircular canal radius of curvature and cochlea size in extant bats (data from Davies et al.[63]) and in *Vielasia* (STAR Methods; Data S1M). Box plots. ASC, anterior semicircular canal; LSC, lateral semicircular canal; PSC, posterior semicircular canal; cochlea size.[64]

(D) Plot of mammal species including bats on first two axes of linear discriminant analysis (LDA) of PGLS regression residuals of each semicircular canal log size against cochlear log size; percentages represent average between-groups variance explained (see also Figure S3B).

Mammal silhouettes from PhyloPic (http://www.phylopic.org): pteropodid https://www.phylopic.org/images/1dda6a3d-e407-47fb-add8-fb6b0572f688/pteropus-medius by Margot Michaud, CC0 1.0 Universal Public Domain Dedication; yangochiropteran https://www.phylopic.org/images/18bfd2fc-f184-4c3a-b511-796aafcc70f6/corynorhinus-townsendii by Yan Wong, CC0 1.0 Universal Public Domain Dedication; mouse http://www.phylopic.org/image/92989e35-4e68-4a2d-b3a2-191ba9da671a/, *Mus musculus*, by Kamil S. Jaron, Public Domain Dedication 1.0 license; elephant http://www.phylopic.org/image/7c9ab182-175d-4f02-96d0-09c1e5212bff/, *Elephas maximus*, by T. Michael Keesey, Creative Commons Attribution 3.0 Unported license; whale (http://www.phylopic.org/image/374accb5-16d5-4cb9-a67a-e881ddfec114/, *Balaenoptera acutorostrata*, by T. Michael Keesey, Creative Commons Attribution 3.0 Unported license; dolphin http://www.phylopic.org/image/3caf4fbd-ca3a-48b4-925a-50fbe9acd887/, *Delphinus capensis*, by T. Michael Keesey, Creative Commons Attribution 3.0 Unported license.

See also Data S1.

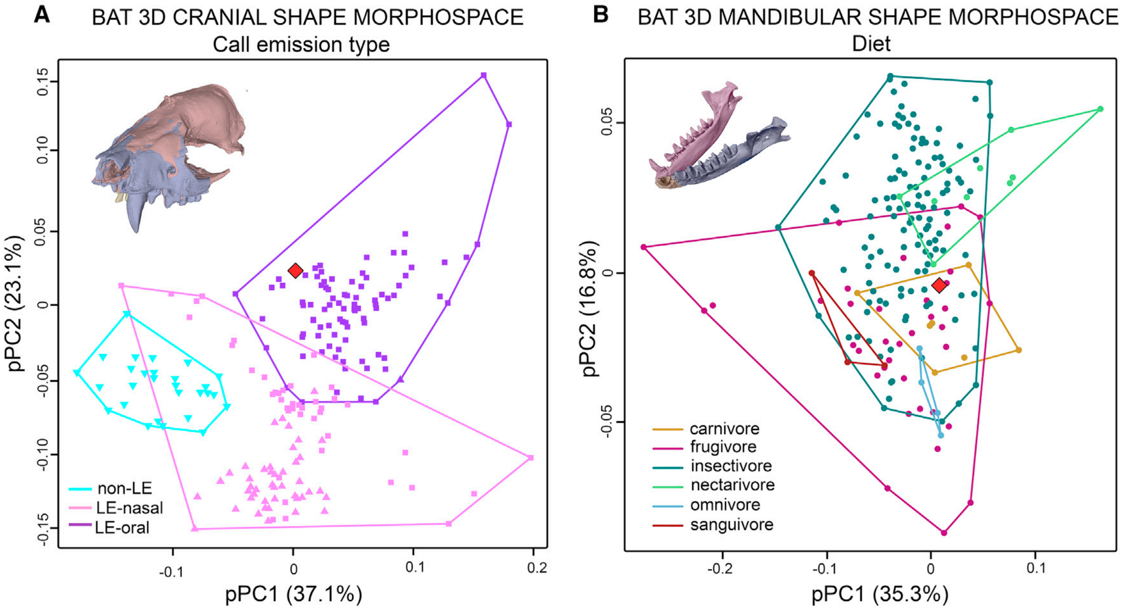

Figure 4. Skull and mandible shape in *Vielasia sigei* compared with extant bats

(A) Cranial morphospaces of bats based on phylogenetic principal component analysis (pPCA) score (phylogenetic principal component [pPC] 1 vs. pPC2) and position of *Vielasia* (red diamond) in morphospace with respect to echolocation call emission type: non-LE, no laryngeal emission; LE-nasal, nasal laryngeal-emitters; LE-oral, oral laryngeal-emitters; squares, yangochiropterans; triangles, LE yinpterochiropterans; inverted triangles, non-LE yinpterochiropterans. Reconstructed composite cranial model of *Vielasia sigei*, colors indicate the three virtually assembled elements UM-VIE-250, UM-VIE-251, and UM-VIE-668.

(B) Mandibular morphospace of bats based on pPCA score (pPC1 vs. pPC2) and position of *Vielasia* (red diamond) in morphospace with respect to diet. Reconstructed composite mandible model of *Vielasia sigei*, colors indicate the two virtually assembled elements UM-VIE-254 and UM-VIE-255 (and mirror). Comparative data from Arbour et al.[65]

See also STAR Methods, Figure S5, and Data S1.

trigonid) at center; m1–m2 with complete buccal cingulid; and m3 talonid reduced but hypoconulid distinct.

Postcranium relatively unspecialized among bats. Glenoid fossa of scapula with only rudimentary dorsal articulation facet for greater tuberosity of humerus; proximal humerus with hemispherical head, greater tuberosity extending just proximal to head, shallow fossa for supraglenoid tuberosity of scapula, distal humerus articular surface only slightly offset with respect to shaft, central capitulum spherical, epitrochlea broad, distal spinous process separate from trochlea, not reaching distal articular surface; proximal radius epiphyseal surface triangular, rounded apices, and without conspicuous ridge separating articular facets for capitulum and trochlea; head of proximal femur large, spherical, directed anteromedially, with fovea capitis and neck, trochanters large, widely spread, lesser trochanter not extending proximally beyond base of head, greater trochanter extending to half head height, proximal shaft straight, and slightly flattened.

For differential diagnosis and expanded description, see STAR Methods and Figure S1.

Body mass estimate. Long bone shaft diameter provides the most accurate estimate of body mass in bats.[66–69] In the absence of exact-midshaft measurements for *Vielasia sigei*, we used the proxies of lower last premolar (p4), first molar (m1), and upper first molar (M1) areas[66] (18.31, 17.39, and 20.04 g, respectively), as well as humerus minimum and maximum diameter closest to mid-shaft (1.44 and 1.70 mm, giving mass estimates of 16.09 and 23.71 g, respectively). The geometric mean of these proxies indicates a body mass of 18.94 g for *Vielasia*. This compares with the median value of 13.8 g for 905 extant bat species and a range of 9–90 g for Eocene stem bats.[67–69] Among stem bats, *Vielasia sigei* is smaller in skull and toothrow length (18.3 and 7.9 mm, respectively; Table 1) than *Icaronycteris index* (21.2 and 8.3 mm, see tables 1 and 2 of Jepsen[37]) but larger than *Palaeochiropteryx tupaiodon* (12.5–17 and 7.5 mm, see table 3 of Russell and Sigé[70]). Body mass estimates based on long bone shaft diameter for the two latter species are 24–27 and 9–16 g, respectively,[67] and our intermediate estimate of 18.94 g for *Vielasia sigei* is not inconsistent with these reconstructions.

Phylogenetic relationships of *Vielasia sigei* and identity as a stem bat

To formally test the relationship of *Vielasia sigei* n. gen. et sp. to crown Chiroptera, we used a matrix of 2,665 craniodental characters (925 parsimony informative, 433 variable but non-parsimony informative; MorphoBank Project 4407, http://morphobank.org/permalink/?P4407), based on that of O'Leary et al.,[61] that includes *V. sigei* and 21 other bat ingroup terminals (6 extant taxa representing the major extant lineages within the crown clade, plus 15 Eocene fossil taxa), plus 8 non-bat eutherian outgroup terminals (3 extant, 5 fossil; see STAR Methods). *Vielasia sigei* could be meaningfully scored (i.e., excluding unknown and inapplicable characters) for 1,421 characters, rendering it 53.3% complete and hence the most complete of all the fossil bats included in our matrix (Data S1B), with the others ranging in completeness from 45.9% (*Icaronycteris* index) to 5.7% (*Microchiropteryx foliae*).

Table 1. Measurements (mm) for holotype and paratypes of *Vielasia sigei* n. gen. et sp

	Mandibular					
Cranial parameters	UM-VIE-250	UM-VIE-251	UM-VIE-252	Parameters	UM-VIE-254	UM-VIE-255
Cranium L	18.29	–	–	dentary L	–	(15.24)[a]
Cranium W (mast)	9.01	–	–	dentary D	2.108	2.131
Cranium W (zygmax)	12.30	–	–	dentary H	–	5.950
Cranium W (zygmin)	10.0	–	–	Rc1–m3	8.816	–
Interorbital W	4.24	–	–	Rp4–m3	5.888	5.762
Rostrum W	7.62	–	–	c1L	1.172	–
Rostrum H (M2)	6.34	–	–	c1W	0.895	–
Braincase H	6.65	–	–	p2L	–	–
RC1–M3	(7.90)	–	–	p2W	–	–
RP4–M3	5.30	–	–	p3L	1.114	1.097
RP3L	1.03	1.028	–	p3W	0.691	0.706
RP3W	0.798	0.810	–	p4L	1.210	1.276
RP4L	1.56	–	–	p4W	0.971	0.880
RP4W	1.640	–	–	m1L	1.680	1.735
RM1L	1.71	1.730	–	m1WT	1.521	1.525
RM1W	2.342	2.387	–	m1Wt	1.316	1.343
RM2L	1.63	1.687	–	m2L	1.624	1.676
RM2W	2.612	2.571	–	m2WT	(1.335)	1.523
RM3L	1.0	–	–	m2Wt	1.052	1.060
RM3W	2.284	–	–	m3L	1.589	1.575
LC1–M3	–	7.860	(7.937)	m3WT	1.065	1.018
LP4–M3	5.28	5.370	5.448	m3Wt	0.749	0.786
LC1L	–	1.45	1.495	–	–	–
LC1W	–	0.977	1.033	–	–	–
LP3L	–	1.018	1.060	–	–	–
LP3W	–	0.808	0.862	–	–	–
LP4L	1.53	1.649	1.635	–	–	–
LP4W	1.637	1.558	1.616	–	–	–
LM1L	1.71	1.741	1.720	–	–	–
LM1W	2.381	2.429	2.359	–	–	–
LM2L	1.64	1.676	1.685	–	–	–
LM2W	2.622	2.512	2.554	–	–	–
LM3L	1.0	1.032	1.040	–	–	–
LM3W	2.258	2.294	2.393	–	–	–

Abbreviations: C, canine; P, premolar; M, molar; upper case, upper toothrow; lower case, lower toothrow; mast, across mastoid; L, length; W, width; WT, trigonid width; wt, talonid width; zyg, width across zygomatic arch; numbers in parentheses indicate estimates.

[a] Estimate from aligned meshes of UM-VIE-254 and UM-VIE-255.

Given the widely recognized beneficial impact in phylogenetics of combining and analyzing morphological and molecular data simultaneously,[71–76] and the extensive DNA sequence data available for our extant terminals, we used a total evidence approach, combining our craniodental matrix with 36.9 kb of DNA sequence data from 27 nuclear loci, taken directly from O'Leary et al.[61] The inclusion of temporal information has also been shown to increase phylogenetic accuracy,[54] and so our focal analysis was a dated Bayesian analysis of our total evidence dataset using a fossilized birth-death model implemented in MrBayes,[77,78] with all tips and selected nodes assigned age priors and with separate Independent Gamma Rates clock models applied to the morphological and molecular partitions (see STAR Methods). The topology that resulted from this analysis is shown in Figure 2.

In this analysis, *Vielasia* was relatively weakly placed (Bayesian posterior probability [BPP] = 0.63) as sister to crown bats, but there was much stronger support (BPP = 0.95)—the strongest of any grouping outside the crown clade—for a clade comprising crown bats, *Vielasia* and *Cambaya* (Figure 2). However, there was also maximal support (BPP = 1.00) for monophyly of the crown clade, excluding *Vielasia* and *Cambaya*. Thus, *Vielasia* is placed as a close relative of, but outside, crown Chiroptera. The remaining fossil bats formed a paraphyletic assemblage outside this clade, with Onychonycteridae as the first family to diverge, which is congruent with previous suggestions.[9,28,67] Several relationships outside the crown clade are weakly supported (BPP < 0.75), as expected given that they involve fossil taxa represented by morphological data only,[79–82] and particularly because most of these fossil taxa are known from dental remains only and hence suffer from high incompleteness (see Data S1B); a similar result was found in another recent study of fossil bats.[36] Thus, although this analysis provides strong support for the position of *Vielasia* within Chiroptera, confident resolution of relationships among other stem bats will likely require the discovery of more complete specimens.

Assuming the topology presented in Figure 2, monophyly of crown Chiroptera to the exclusion of *Vielasia* is supported by 49 unambiguous craniodental synapomorphies (Data S2), and topologies in which *Vielasia* was constrained to fall within crown Chiroptera (as either a yinpterochiropteran or a yangochiropteran) were rejected by Bayes factors calculated using stepping stone analysis ($2\ln(B_{10}) > 200$; Data S1E). In addition to this focal analysis, we also carried out maximum parsimony (MP) analysis of the full craniodental dataset and MP analysis of a ‘‘homoplasy-filtered’’ version of the craniodental dataset in which characters that show homoplasy relative to the current consensus view of extant bat phylogeny (i.e., with monophyletic Yangochiroptera and Yinpterochiroptera; e.g., Shi and Rabosky[83] and Amador et al.[84]) were excluded, and undated Bayesian analysis of the total evidence dataset (see STAR Methods and Figure S2). These subsidiary analyses also support *Vielasia* as a stem bat, and a constrained position of *Vielasia* within the crown clade is rejected by Templeton tests (for the MP analyses) and Bayes factors (for the undated Bayesian analysis; see STAR Methods; Data S1E).

The age of crown bats was poorly constrained in our dated total evidence analysis (Figure 2), stretching from the earliest Eocene to the late middle Eocene (95% highest probability density [HPD] interval: 53.1–38.5 mya). The divergence between *Vielasia* and crown bats was estimated as probably occurring during the early Eocene (95% HPD interval: 56.5–49.5 mya), and the median branch length of 3.8 mya leading to *Vielasia* indicates that it is not a plausible direct ancestor of crown bats. The deepest divergence within Chiroptera, between Onychonycteridae and the other taxa, was estimated as probably occurring within the Paleocene (95% HPD interval: 66.9–58.9 mya), although chiropterans are as yet unknown from this epoch.

Postcranial morphology and flight capabilities

Like all other Eocene stem bats so far known, *Vielasia sigei* appears to have been capable of powered flight: its skeletal elements exhibit specializations for flight found in all bats, extant and extinct,[45,46] although its postcranium is relatively unspecialized among bats, being more similar to species of *Icaronycteris* and *Archaeonycteris* than to extant bats (see STAR Methods). In *Vielasia sigei*, several skeletal features are indicative of considerable rotational movement in the wing joints, with few specialized locking mechanisms, suggesting that it was capable of relatively maneuverable flight.[85–87] These features include, in the shoulder joint, a hemispherical head on the proximal humerus and scapula with correspondingly simple, pear-shaped glenoid cavity, and, in the elbow joint, a distal humerus with spherical central capitulum and broad medial epicondyle with low spinous process, and proximal radius epiphyseal surface without conspicuous ridge separating articular facets for capitulum and trochlea (Figures 1K–1P; STAR Methods).

Petrosal morphology and echolocation capabilities

Vielasia’s petrosal is relatively isolated from the rest of the skull (Figures 1A and 1D), with the enlarged pars cochlearis contacting the basicranium via four tiny bony splints and otherwise presumably loosely attached to the basicranium via ligaments, as in all extant bats known to echolocate laryngeally.[9,88] In non-echolocating pteropodids and *Onychonycteris*, the petrosal is instead fused or sutured to the basicranium, as in other eutherians.[41,42,88] Cochlear width (oblique diameter along second half-turn of coiled cochlea duct[43]; 2.50 mm; Data S1F) relative to basicranial width (across mastoids[43]; 9.01 mm; Data S1F) is greater in *Vielasia* than in non-echolocating pteropodids, and falls within the range for extant laryngeally echolocating (LE) bats (e.g., vespertilionids, emballonurids, rhinopomatids, some phyllostomids, and some hipposiderids) (see figures s8 and s9 of Simmons et al.[9], and figure 12.5.15 of Habersetzer et al.[47]). It is greater than in *Onychonycteris*, *Icaronycteris*, and *Archaeonycteris* spp., and more similar to that reported for *Hassianycteris* and *Palaeochiropteryx* species (see figure 12.5.15 of Habersetzer et al.[47]). Overall cochlea size (calculated as the average of the diameter of the first cochlear turn, the second cochlear turn, and slant height, following Spoor et al.[64] and Davies et al.[63]; Data S1F and S1M) is within the interquartile range for extant LE bats but below the median value for all bats (Figure 3C).

In a virtual endocast of *Vielasia*’s petrosal (Figures 3A and S1F), the coiled cochlea represents 74% of the volume of the labyrinth (Data S1F; see below). The number of turns in the cochlea is 2.25 (Data S1F), a degree of coiling that is found in members of both groups of extant LE bats, namely Yangochiroptera and Yinpterochiroptera; it is greater than in many non-LE pteropodids and some LE carnivorous megadermatids and nycterids (see suppl. table s2 of Davies et al.[19], Habersetzer et al.[47], and Ekdale[89]). *Vielasia* lacks the greatly enlarged cochlear basal turn found in extant bats that use specialized constant frequency (CF) calls (e.g., rhinolophids[90]). In *Vielasia*, the secondary bony lamina in the cochlear canal extends well beyond the basal turn, and almost to the apex, as it does in extant LE bats but not in pteropodids.[41]

Mapping *Vielasia* and extant LE and non-LE bats onto a plot of log basilar membrane length against log body mass for placental mammals (Figure 3B; data from Davies et al.[19]) shows *Vielasia* lying above the mammalian regression line, as do most LE bats. That is, compared with non-echolocating placentals, basilar membrane length tends to be longer than expected for body mass in most LE bats and in *Vielasia*. Supporting this, we found the intercepts of PGLS (phylogenetic generalized least squares) regression lines of bats and of highly specialized mammals (LE bats + high-frequency- and low-frequency-hearing cetaceans) to slightly, but significantly, differ from those of nonspecialized mammals, whereas slopes do not differ (Figure S3A; STAR Methods; Data S1H).

Cochlear coiling and basilar membrane length are correlated with echolocation call parameters and hearing frequencies.[19] Using the regression equations of Davies et al.[19] for extant bats, and based on cochlea coiling (2.25 turns) and basilar membrane length (12.38 mm) in the fossil (Data S1F and S1G), we estimate the call frequency range for *Vielasia sigei* to be ∼30–56 kHz with peak energy of ∼42 kHz. These call frequencies are within the range recorded by Davies et al.[19] for both extant yangochiropterans and LE yinpterochiropterans (see supplemental table s8 of Davies et al.[19]) and overlap the range those authors reconstructed for the hypothetical ancestor of modern bats (∼40–65 kHz with peak energy ∼50 kHz). In terms of hearing, we estimate a high-frequency hearing limit for *Vielasia sigei* of ∼60–105 kHz (at 30 and 60 dB, respectively) and low-frequency hearing limit of ∼0.5–1.5 kHz (at 60 and 30 dB, respectively) (Data S1K–S1L; Figure S4), given our body mass estimate of 18.94 g.

Other neuroanatomical properties related to hearing and echolocation that can be assessed in *Vielasia*'s exceptionally well-preserved inner ear include the connection between the spiral ganglion (housed in Rosenthal's canal) and the cochlear nerve.[91] *Vielasia sigei* exhibits a "foraminal wall" characterized by many small apertures piercing the bony wall of the canal (Figure 3A), a morphology regarded to be the plesiomorphic condition in bats.[91] *Vielasia sigei* shares this cochlear morphology with LE yinpterochiropterans, pteropodids, and other mammals, but not yangochiropterans, in which the perforations in the bony wall are larger ("fenestral wall") and/or the wall is absent ("wall-less"); in yangochiropterans, combinations of these two derived states along the canal are thought to contribute to the high diversity of echolocation strategies seen in those bats.[91]

In *Vielasia* the petrosal's delicate vestibular organ is equally well preserved and can be precisely measured, a unique occurrence in an early Eocene bat fossil. As occurs in all extant LE bats but not in non-LE bats,[88] the three semicircular canals deviate from circularity in *Vielasia* (Figures 3A and S1F; STAR Methods; Data S1F). Davies et al.[63] also found that in LE bats the cochlea was relatively much larger than the semicircular canals, as measured by the radius of their curvature (R).[64] Among mammals, *Vielasia sigei* groups among LE bats according to PGLS regression residuals of semicircular canal size vs. cochlea size (Figure 3D), and when phylogenetic signal is accounted for in the analysis, little separation of LE and non-LE mammalian groups occurs (Figure S3B; Data S1I and S1J). The anterior semicircular canal is larger than that of the lateral and posterior canals (Figure 3C), as it is in all yangochiropterans and pteropodids (Data S1M), rather than the lateral canal being typically largest (as in rhinolophids/CF echolocators).[92]

Eye size in *Vielasia*, estimated here to be less than or equal to ∼2.3 mm diameter (reconstructed using the method of Brooke et al.[93]; STAR Methods), is smaller than the minimum eye size evidently required for aerial pursuit of night-flying insects by extant bats without the assistance of echolocation.[22] It is also smaller than the eye size predicted for the common ancestor of bats (3.13 mm).[22] Relative to body size, *Vielasia*'s estimated eye size is smaller than the smallest modern pteropodid eye, relatively larger than in bats that use CF calls (e.g., rhinolophids and hipposiderids) or DH calls (frequency-modulated, dominant harmonic calls, e.g., vespertilionids and molossids), and similar to many extant bats that use multiharmonic (MH) calls (e.g., emballonurids and phyllostomids) (see figure 5, supplement 1 of Thiagavel et al.[22]).

Echolocation emission and diet

3D geometric morphometric (GM) analysis of *Vielasia sigei*'s cranial shape, compared with 202 extant bat species of known echolocation type[65] (Data S1N and S1P), suggests *V. sigei* emitted its echolocation call through its mouth rather than its nose (Figures 4A and S5A) based on the two first phylogenetic principal component (pPC) axes, which largely reflect cranial elongation (pPC1, 37.1%) and rostral dorsoventral flexion (pPC2, 23.1%). Of the 202 extant bat species compared, *Vielasia* lies closest in pPC1-pPC2 morphospace to the vespertilionid *Myotis keenii*, the molossid *Mops condylurus*, and the natalid *Natalus stramineus*, all of which are oral emitters.[65,94,95] As in extant oral-emitting bats (e.g., vespertilionids, emballonurids, and mormoopids), the hard palate in *Vielasia* is approximately aligned with the basicranium (small positive tilt of the rostrum on the basicranial axis), the foramen magnum is directed posteriorly, and the plane of the lateral semicircular canal is relatively parallel with that of the basicranium.[94,95] Via this arrangement, orofacial and cranial structures are aligned, such that undistorted echolocation calls are emitted from the open mouth directly in the line of flight.[95] *Vielasia* lacks the ventral flexion of the rostrum characterizing Old World nasal emitters (e.g., rhinolophids and hipposiderids) and New World nasal emitters (e.g., phyllostomids).[65,94,95]

Arbour et al.[65] found that mandible shape better reflects diet in extant bats than cranial shape. Compared with 191 extant bat taxa (Data S1O and S1P), *Vielasia* groups in mandibular shape morphospace primarily with insectivorous bat species (Figures 4B and S5B). *Vielasia* is intermediate in anteroposterior elongation of the dentary (pPC1, 35.3%) and mandible body and coronoid height (pPC2, 16.8%), grouping with insectivorous, carnivorous, and frugivorous bats (Figure 4B). However, its intermediate dorsoventral mandible flexure (pPC3, 11.9%) and tooth row length (pPC4, 11.6%) place it within the morphospace occupied by insectivorous bats only (Figure S5B). Stem bats whose gut contents are preserved in other fossil Lagerstätten also appear to have been primarily insectivorous, with Messel bats such as *Palaeochiropteryx* spp. evidently consuming predominantly small moths and caddisflies[40,47] and the larger *Archaeonycteris trigonodon* and *Hassianycteris* spp. interpreted to have included larger moths and beetles in their diet.[40,46,47]

Cave dwelling in a changing world

Bats first appeared in the fossil record directly following the Paleocene/Eocene Thermal Maximum (PETM) at 55.93 mya.[62] They radiated during the Early Eocene Climatic Optimum (EECO, 53.26–49.14 mya[62]; Figure 2) during global "hothouse" conditions,[96] and rapidly appeared on most continents.[28] These early Eocene bats are typically fossilized in fluvio-lacustrine or estuarine deposits and are interpreted to have roosted in trees,[22,31,46,97,98] in the paratropical Eocene forests that once stretched to the poles.[98,99]

Vielasia sigei, however, demonstrates that some bats had moved into caves by the late early Eocene. *Vielasia* is the oldest bat recovered from a cave deposit, with cave dwelling otherwise first recorded in early members of the modern bat family Rhinolophidae in the middle Eocene of China.[34] At least 23 individuals of *V. sigei* occur in the Vielase deposit, including at least one juvenile represented by its molariform deciduous posterior dentition (dP4/4).[58] This dental condition is plesiomorphic for placental mammals and contrasts with the condition in all extant bats in which the entire deciduous dentition (dI1/1 to dP4/4) is uniquely specialized (typically hook-like[100]); the latter enables a newborn bat to cling passively but safely to its mother during flight and suspended roosting. In *Vielasia*, wear facets on dP4/4[58] indicate that juveniles began to hunt insects before weaning, as deduced also from similar dental evidence and confirmed by gut contents in pups of the Eocene bat *Palaeochiropteryx tupaiodon*.[101]

An important evolutionary driver for bats like *Vielasia sigei* to first congregate in caves may have been the transition to globally cooler and less stable conditions, which began around 49 mya between the early and middle Eocene and was preceded by high-amplitude variations in temperature.[62] This marked the end of the hothouse EECO, although under the cooler greenhouse conditions of the early middle Eocene, the world was still much warmer than now.[96]

Alternatively, caves in these middle latitudes could have provided attractive new roosts for evolving bats with advanced echolocation, flight, and metabolic capabilities, as well as changing behavioral and social needs.[98] Among benefits for extant bats, cave roosting offers not only a thermally stable environment but also protection from predators, increased mating opportunities and success in rearing young, foraging, social and behavioral information transfer, and reduced competition for tree roosts from birds and other mammals.[102,103] In higher latitudes today, it facilitates hibernation, reducing energy costs for bats,[104] with cave-dwelling species also generally migrating less far than tree-roosting species.[105] Cave roosting is correlated with increased longevity in bats.[106,107] Today, caves and underground habitats are used by almost half of all bat species.[108]

Early acquisition of echolocation in bats

Based on morphological features including relative cochlear size, shape of the orbicular process of the malleus, and stylohyal morphology,[9,18,40–47] previous paleontological studies have suggested that Eocene stem bats were capable of laryngeal echolocation,[9,18,40–47] with the possible exception of *Onychonycteris finneyi*,[9,48] but see Veselka et al.[18] Relative cochlear size and an articulation between the tympanic bone in the middle ear and a cranially expanded stylohyal bone (part of the hyoid arch that supports the larynx) remain definitive and uncontested hallmarks of laryngeal echolocation in bats.[18,48] The stylohyal and middle ear bones are not yet known for *V. sigei*, but its three-dimensionally well-preserved cranium and petrosal (cochlea and semicircular canals) has enabled this early bat's inclusion in analyses of large datasets of cranial and inner ear attributes related to auditory and echolocation capabilities in extant bats. In these analyses, *V. sigei* grouped with LE rather than non-LE bats, and there is little to suggest that *Vielasia* used a type of echolocation different from that used by modern LE bats. This finding is congruent with previous studies suggesting that some non-crown bats may have had modern or near-modern echolocation capabilities[47] and contrasts with some proposals based on embryological and molecular analyses of extant bats that, if stem bats did use echolocation, it was of a primitive kind (such as tongue-clicking).[13]

At 50 mya, *Vielasia*'s uncrushed, near-complete skull is the oldest yet known, and its description here significantly expands empirical data available for inclusion in chiropteran phylogenetic analyses, evolutionary modeling of the development of bat echolocation, and in embryological and molecular analyses investigating high-frequency hearing and the inner ear of bats.

Conclusions

Our results indicate that all attributes correlated with echolocation that are measurable in the stem bat *Vielasia sigei* fall within the range observed in extant laryngeally echolocating bats, and this similarity in reconstructed hearing capabilities suggests *V. sigei* was also capable of modern laryngeal echolocation. The analyses presented here collectively suggest either that advanced echolocation evolved once in the common ancestor of extant bats (and was used by stem bats such as *Vielasia sigei*) but was lost in pteropodids, or that advanced echolocation evolved independently several times in bats, at least once in non-crown bats and twice in extant bat lineages.

The early Eocene *Vielasia sigei* was a relatively small (∼18.94 g), insect-eating, evidently oral-emitting echolocator, with expanded cochlea, reduced eye size, and capable of maneuverable flight. Our calculations suggest it may have used a multiharmonic echolocation call, with an estimated frequency range of ∼30–56 kHz. It appears to have been a cave-dweller, living in small colonies that included semi-independent young. Given that our preferred phylogenetic hypothesis places *Vielasia* as the closest known relative of crown Chiroptera, at least some of these features may also have characterized the last common ancestor of modern bats.

STAR★METHODS

Detailed methods are provided in the online version of this paper and include the following:

- KEY RESOURCES TABLE
- RESOURCE AVAILABILITY
  - ○ Lead contact
  - ○ Materials availability
  - ○ Data and code availability
- EXPERIMENTAL MODEL AND SUBJECT DETAILS
- METHOD DETAILS
  - ○ Data collection, CT scanning, model reconstruction, and measurements
  - ○ Comparative material
  - ○ Institutional abbreviations
  - ○ Differential diagnosis
  - ○ DESCRIPTION
  - ○ PHYLOGENETIC ANALYSES
  - ○ LINEAR AND GEOMETRIC MORPHOMETRIC ANALYSES
- QUANTIFICATION AND STATISTICAL ANALYSIS

SUPPLEMENTAL INFORMATION

Supplemental information can be found online at https://doi.org/10.1016/j.cub.2023.09.043.

ACKNOWLEDGMENTS

We are grateful to B. Marandat and A.L. Charruault for the preparation of the Vielase fossil material and its μCT-scanning. We acknowledge the MRI platform member of the national infrastructure France-BioImaging supported by the French National Research Agency (ANR-10-INBS-04, «Investments for the future»), the Labex CEMEB (ANR-10-LABX-0004) and NUMEV (ANR-10-LABX-0020), and the facilities and technical assistance of the National Imaging Facility, a National Collaborative Research Infrastructure Strategy (NCRIS) capability, at UNSW Sydney. Funding for Quercy research is from ANR-22-CE02-0014-01 (ENLIVEN, PI M.J.O.), and S.J.H and R.M.D.B. were supported by the Australian Research Council (DP180100792). Access to JASMIN, the UK's collaborative data analysis environment (https://jasmin.ac.uk), was supported by a National Environmental Research Council Standard Grant to R.M.D.B. (NE/T000341/1). We thank M. Archer and the late B. Sigé for their contributions to early research of the Vielase bat; T. Hung and T.J. Myers for their technical and statistical support; and four anonymous reviewers whose suggestions significantly improved the manuscript. This is ISEM publication no. ISEM 2023-003.

AUTHOR CONTRIBUTIONS

Conceptualization, M.J.O., S.J.H., J.M., and R.M.D.B.; methodology, S.J.H., J.M., R.M.D.B., and M.J.O.; investigation, S.J.H., J.M., R.M.D.B., and M.J.O.; writing – original draft, S.J.H., R.M.D.B., and J.M.; writing – review & editing, S.J.H., J.M., R.M.D.B., and M.J.O.; visualization, M.J.O. and J.M.; funding acquisition, S.J.H., R.M.D.B., and M.J.O.; resources, M.J.O. and R.M.D.B.; supervision, M.J.O.

DECLARATION OF INTERESTS

The authors declare no competing interests.

INCLUSION AND DIVERSITY

We support inclusive, diverse, and equitable conduct of research.

Received: September 19, 2022
Revised: July 24, 2023
Accepted: September 18, 2023
Published: October 18, 2023

REFERENCES

1. Simmons, N.B., and Cirranello, A.L. (2023). Bat species of the world: a taxonomic and geographic database. Accessed 17 April 2023. https://batnames.org/.
2. Meredith, R.W., Janečka, J.E., Gatesy, J., Ryder, O.A., Fisher, C.A., Teeling, E.C., Goodbla, A., Eizirik, E., Simão, T.L.L., Stadler, T., et al. (2011). Impacts of the Cretaceous terrestrial revolution and KPg extinction on mammal diversification. Science *334*, 521–524. https://doi.org/10.1126/science.1211028.
3. Phillips, M.J. (2016). Geomolecular dating and the origin of placental mammals. Syst. Biol. *65*, 546–557. https://doi.org/10.1093/sysbio/syv115.
4. Tarver, J.E., dos Reis, M., Mirarab, S., Moran, R.J., Parker, S., O'Reilly, J.E., King, B.L., O'Connell, M.J., Asher, R.J., Warnow, T., et al. (2016). The interrelationships of placental mammals and the limits of phylogenetic inference. Genome Biol. Evol. *8*, 330–344. https://doi.org/10.1093/gbe/evv261.
5. Phillips, M.J., and Fruciano, C. (2018). The soft explosive model of placental mammal evolution. BMC Evol. Biol. *18*, 104. https://doi.org/10.1186/s12862-018-1218-x.
6. Álvarez-Carretero, S., Tamuri, A.U., Battini, M., Nascimento, F.F., Carlisle, E., Asher, R.J., Yang, Z., Donoghue, P.C.J., and dos Reis, M. (2022). A species-level timeline of mammal evolution integrating phylogenomic data. Nature *602*, 263–267. https://doi.org/10.1038/s41586-021-04341-1.
7. Norberg, U.M. (1994). Wing design, flight performance, and habitat use in bats. In Ecological Morphology: Integrative Organismal Biology, P.C. Wainwright, and S.M. Reilly, eds. (University of Chicago Press), pp. 205–239.
8. Teeling, E.C., Springer, M.S., Madsen, O., Bates, P., O'Brien, S.J., and Murphy, W.J. (2005). A molecular phylogeny for bats illuminates biogeography and the fossil record. Science *307*, 580–584. https://doi.org/10.1126/science.1105113.
9. Simmons, N.B., Seymour, K.L., Habersetzer, J., and Gunnell, G.F. (2008). Primitive early Eocene bat from Wyoming and the evolution of flight and echolocation. Nature *451*, 818–821. https://doi.org/10.1038/nature06549.
10. Fenton, M.B. (1985). Communication in the Chiroptera (Indiana University Press).
11. Speakman, J.R. (2001). The evolution of flight and echolocation in bats: another leap in the dark. Mamm. Rev. *31*, 111–130. https://doi.org/10.1046/j.1365-2907.2001.00082.x.
12. Teeling, E.C., Scally, M., Kao, D.J., Romagnoli, M.L., Springer, M.S., and Stanhope, M.J. (2000). Molecular evidence regarding the origin of echolocation and flight in bats. Nature *403*, 188–192. https://doi.org/10.1038/35003188.
13. Nojiri, T., Wilson, L.A.B., López-Aguirre, C., Tu, V.T., Kuratani, S., Ito, K., Higashiyama, H., Son, N.T., Fukui, D., Sadier, A., et al. (2021). Embryonic evidence uncovers convergent origins of laryngeal echolocation in bats. Curr. Biol. *31*, 1353–1365.e3. https://doi.org/10.1016/j.cub.2020.12.043.
14. Springer, M.S., Teeling, E.C., Madsen, O., Stanhope, M.J., and de Jong, W.W. (2001). Integrated fossil and molecular data reconstruct bat echolocation. Proc. Natl. Acad. Sci. USA *98*, 6241–6246. https://doi.org/10.1073/pnas.111551998.
15. Teeling, E.C. (2009). Hear, hear: the convergent evolution of echolocation in bats? Trends Ecol. Evol. *24*, 351–354. https://doi.org/10.1016/j.tree.2009.02.012.
16. Liu, Z., Chen, P., Xu, D.M., Qi, F.Y., Guo, Y.T., Liu, Q., Bai, J., Zhou, X., and Shi, P. (2022). Molecular convergence and transgenic evidence suggest a single origin of laryngeal echolocation in bats. iScience *25*, 104114. https://doi.org/10.1016/j.isci.2022.104114.
17. Eick, G.N., Jacobs, D.S., and Matthee, C.A. (2005). A nuclear DNA phylogenetic perspective on the evolution of echolocation and historical biogeography of extant bats (Chiroptera). Mol. Biol. Evol. *22*, 1869–1886. https://doi.org/10.1093/molbev/msi180.
18. Veselka, N., McErlain, D.D., Holdsworth, D.W., Eger, J.L., Chhem, R.K., Mason, M.J., Brain, K.L., Faure, P.A., and Fenton, M.B. (2010). A bony connection signals laryngeal echolocation in bats. Nature *463*, 939–942. https://doi.org/10.1038/nature08737.
19. Davies, K.T., Maryanto, I., and Rossiter, S.J. (2013). Evolutionary origins of ultrasonic hearing and laryngeal echolocation in bats inferred from morphological analyses of the inner ear. Front. Zool. *10*, 2. https://doi.org/10.1186/1742-9994-10-2.
20. Teeling, E.C., Jones, G., and Rossiter, S.J. (2016). Phylogeny, genes, and hearing: implications for the evolution of echolocation in bats. In Bat Bioacoustics, M. Fenton, A. Grinnell, A. Popper, and R. Fay, eds. (Springer), pp. 25–54. https://doi.org/10.1007/978-1-4939-3527-7_2.
21. Wang, Z., Zhu, T., Xue, H., Fang, N., Zhang, J., Zhang, L., Pang, J., Teeling, E.C., and Zhang, S. (2017). Prenatal development supports a single origin of laryngeal echolocation in bats. Nat. Ecol. Evol. *1*, 21. https://doi.org/10.1038/s41559-016-0021.
22. Thiagavel, J., Cechetto, C., Santana, S.E., Jakobsen, L., Warrant, E.J., and Ratcliffe, J.M. (2018). Auditory opportunity and visual constraint enabled the evolution of echolocation in bats. Nat. Commun. *9*, 98. https://doi.org/10.1038/s41467-017-02532-x.
23. Eiting, T.P., and Gunnell, G.F. (2009). Global completeness of the bat fossil record. J. Mamm. Evol. *16*, 151–173. https://doi.org/10.1007/s10914-009-9118-x.
24. Brown, E.E., Cashmore, D.D., Simmons, N.B., and Butler, R.J. (2019). Quantifying the completeness of the bat fossil record. Palaeontology *62*, 757–776. https://doi.org/10.1111/pala.12426.
25. Tabuce, R., Antunes, M.T., and Sigé, B. (2009). A new primitive bat from the earliest Eocene of Europe. J. Vertebr. Paleontol. *29*, 627–630. https://doi.org/10.1671/039.029.0204.

26. Hooker, J.J. (2010). The mammal fauna of the early Eocene Blackheath Formation of Abbey Wood, London. Monographs of the Palaeontographical Society *164*, 1–153. https://doi.org/10.1080/25761900.2022.12131814.
27. Marandat, B., Adnet, S., Marivaux, L., Martinez, A., Vianey-Liaud, M., and Tabuce, R. (2012). A new mammalian fauna from the earliest Eocene (Ilerdian) of the Corbières (Southern France): palaeobiogeographical implications. Swiss J. Geosci. *105*, 417–434. https://doi.org/10.1007/s00015-012-0113-5.
28. Smith, T., Habersetzer, J., Simmons, N.B., and Gunnell, G.F. (2012). Systematics and paleobiogeography of early bats. In Evolutionary History of Bats: Fossils, Molecules and Morphology, G.F. Gunnell, and N.B. Simmons, eds. (Cambridge University Press), pp. 23–66. https://doi.org/10.1017/CBO9781139045599.003.
29. Ravel, A., Marivaux, L., Tabuce, R., Adaci, M., Mahboubi, M., Mebrouk, F., and Bensalah, M. (2011). The oldest African bat from the early Eocene of El Kohol (Algeria). Naturwissenschaften *98*, 397–405. https://doi.org/10.1007/s00114-011-0785-0.
30. Ravel, A., Adaci, M., Bensalah, M., Charruault, A.-L., Essid, E.M., Ammar, H.K., Marzougui, W., Mahboubi, M., Mebrouk, F., Merzeraud, G., et al. (2016). Origine et radiation initiale des chauves-souris modernes: nouvelles découvertes dans l'Écocène d'Afrique du Nord. Geodiversitas *38*, 355–434. https://doi.org/10.5252/g2016n3a3.
31. Hand, S.J., Sigé, B., Archer, M., Gunnell, G.F., and Simmons, N.B. (2015). A new early Eocene (Ypresian) bat from Pourcy, Paris Basin, France, with comments on patterns of diversity in the earliest chiropterans. J. Mamm. Evol. *22*, 343–354. https://doi.org/10.1007/s10914-015-9286-9.
32. Jones, M.F., Coster, P.M.C., Licht, A., Métais, G., Ocakoğlu, F., Taylor, M.H., and Beard, K.C. (2019). A stem bat (Chiroptera: Palaeochiropterygidae) from the late middle Eocene of northern Anatolia: implications for the dispersal and palaeobiology of early bats. Palaeobiodivers. Palaeoenviron. *99*, 261–269. https://doi.org/10.1007/s12549-018-0338-z.
33. Jones, M.F., Li, Q., Ni, X., and Beard, K.C. (2021). The earliest Asian bats (Mammalia: Chiroptera) address major gaps in bat evolution. Biol. Lett. *17*, 20210185. https://doi.org/10.1098/rsbl.2021.0185.
34. Ravel, A., Marivaux, L., Qi, T., Wang, Y.-Q., and Beard, K.C. (2014). New chiropterans from the middle Eocene of Shanghuang (Jiangsu Province, Coastal China): new insight into the dawn of horseshoe bats (Rhinolophidae) in Asia. Zool. Scr. *43*, 1–23. https://doi.org/10.1111/zsc.12027.
35. Czaplewski, N.J., Morgan, G.S., Emry, R.J., Gignac, P.M., and O'Brien, H.D. (2022). Three New Early Middle Eocene bats (Mammalia: Chiroptera) from Elderberry Canyon, Nevada, USA (Smithsonian Contributions to Paleobiology), pp. 2–25. https://doi.org/10.5479/si.19874677.
36. Rietbergen, T.B., van den Hoek Ostende, L.W., Aase, A., Jones, M.F., Medeiros, E.D., and Simmons, N.B. (2023). The oldest known bat skeletons and their implications for Eocene chiropteran diversification. PLoS One *18*, e0283505. https://doi.org/10.1371/journal.pone.0283505.
37. Jepsen, G.L. (1966). Early Eocene bat from Wyoming. Science *154*, 1333–1339. https://doi.org/10.1126/science.154.3754.1333.
38. Habersetzer, J., and Storch, G. (1987). Klassifikation und funktionelle Flügelmorphologie paläogener Fledermäuse (Mammalia, Chiroptera). Courier Forschungsinst Senckenberg *91*, 117–150.
39. Storch, G., and Habersetzer, J. (1988). *Archaeonycteris pollex* (Mammalia, Chiroptera), eine neue Fledermaus aus dem Eozän der grube Messel bei Darmstadt. Courier Forschungsinst Senckenberg *107*, 263–273.
40. Habersetzer, J., Richter, G., and Storch, G. (1994). Paleoecology of early middle Eocene bats from Messel, FRG. Aspects of flight, feeding and echolocation. Hist. Biol. *8*, 235–260. https://doi.org/10.1080/10292389409380479.
41. Novacek, M.J. (1985). Evidence for echolocation in the oldest known bats. Nature *315*, 140–141. https://doi.org/10.1038/315140a0.
42. Novacek, M.J. (1987). Auditory features and affinities of the Eocene bats *Icaronycteris* and *Palaeochiropteryx* (Microchiroptera, incertae sedis). Am. Mus. Novit. *2877*, 1–18.
43. Habersetzer, J., and Storch, G. (1992). Cochlea size in extant Chiroptera and middle Eocene microchiropterans from Messel. Naturwissenschaften *79*, 462–466. https://doi.org/10.1007/BF01139198.
44. Hand, S.J., Novacek, M.J., Godthelp, H., and Archer, M. (1994). First Eocene bat from Australia. J. Vertebr. Paleontol. *14*, 375–381. https://doi.org/10.1080/02724634.1994.10011565.
45. Simmons, N.B. (1994). The case for chiropteran monophyly. Am. Mus. Novit. *3103*, 1–54.
46. Simmons, N.B., and Geisler, J.H. (1998). Phylogenetic relationships of *Icaronycteris*, *Archaeonycteris*, *Hassianycteris*, and *Palaeochiropteryx* to extant bat lineages, with comments on the evolution of echolocation and foraging strategies in Microchiroptera. Bull. Am. Mus. Nat. Hist. *235*, 1–182.
47. Habersetzer, J., Rabenstein, R., and Gunnell, G.F. (2018). Bats – highly specialized nocturnal hunters with echolocation. In Messel – an Ancient Greenhouse Ecosystem, K.T. Smith, S.F.K. Schaal, and J. Habersetzer, eds. (Senckenberg Gesellschaft für Naturforschung), pp. 249–261.
48. Simmons, N.B., Seymour, K.L., Habersetzer, J., and Gunnell, G.F. (2010). Inferring echolocation in ancient bats. Nature *466*. E8; discussion E9. https://doi.org/10.1038/nature09219.
49. Schmidt-Kittler, N. (1987). Proceedings of International Symposium on Mammalian Biostratigraphy and Palaeoecology of the European Paleogene-Mainz, February 18th–21st 1987. Münchner Geowiss Abh. A 10. 1–312.
50. Legendre, S., Marandat, B., Sigé, B., Crochet, J.-Y., Godinot, M., Hartenberger, J.-L., Sudre, J., Vianey-Liaud, M., Muratet, B., and Astruc, J.-G. (1992). Mammalian fauna of Vielase (phosphorites of Quercy, in the South of France): paleontological evidence for karst formation in the Quercy area as early as the Early Eocene. N. Jahrb. Geol. Paläontol. Monatsh. *1992*, 414–428. https://doi.org/10.1127/njgpm/1992/1992/414.
51. Legendre, S., Sigé, B., Astruc, J.G., de Bonis, L., Crochet, J.-Y., Denys, C., Godinot, M., Hartenberger, J.-L., Lévêque, F., Marandat, B., et al. (1997). Les phosphorites du Quercy: 30 ans de recherche. Bilan et perspectives. [The phosphorites of Quercy: 30 years of investigations. Results and prospects. Geobios *30*, 331–345. https://doi.org/10.1016/S0016-6995(97)80038-1.
52. Escarguel, G. (1999). Les rongeurs de l'Eocène inférieur et moyen d'Europe occidentale: systématique, phylogénie, biochronologie et Paléobiogéographie des Niveaux-Repères MP 7 à MP 14. Palaeovertebrata *28*, 89–351.
53. Gradstein, F.M., Ogg, J.G., Schmitz, M.D., and Ogg, G.M. (2012). The Geologic Time Scale*2012* (Elsevier). https://doi.org/10.1016/C2011-1-08249-8.
54. Mongiardino Koch, N., Garwood, R.J., and Parry, L.A. (2021). Fossils improve phylogenetic analyses of morphological characters. Proc. Biol. Sci. *288*, 20210044. https://doi.org/10.1098/rspb.2021.0044.
55. Barido-Sottani, J., Pohle, A., De Baets, K., Murdock, D., and Warnock, R.C.M. (2022). Putting the F in FBD analyses: tree constraints or morphological data?. Preprint at bioRxiv. https://doi.org/10.1101/2022.07.07.499091.
56. Astruc, J.G., Hugueney, M., Escarguel, G., Legendre, S., Rage, J.-C., Simon-Coinçon, R., Sudre, J., and Sigé, B. (2003). Puycelci, nouveau site à vertébrés de la série molassique d'Aquitaine. Densité et continuité biochronologique dans la zone Quercy et bassins périphériques au Paléogène. [Puycelci, a new vertebrate-bearing locality in the Aquitaine molassic basin. Density and continuity of the Paleogene biochronologic record in the Quercy and peripheral basins area. Geobios *36*, 629–648. https://doi.org/10.1016/j.geobios.2003.01.001.
57. Sigé, B., and Hugueney, M. (2006). Les micromammifères des gisements à phosphate du Quercy (SW France). Strata *1*, 207–226.
58. Sigé, B. (1991). Morphologie dentaire lactéale d'un chiroptère de l'Eocène inférieur-moyen d'Europe. Geobios *24*, 231–236. https://doi.org/10.1016/S0016-6995(66)80029-3.

59. Simms, M.J. (1994). Emplacement and preservation of vertebrates in caves and fissures. Zool. J. Linn. Soc. *112*, 261–283. https://doi.org/10.1111/j.1096-3642.1994.tb00320.x.

60. Kowalski, K. (1995). Taphonomy of bats (Chiroptera). [Taphonomie de chauves-souris (Chiroptera). Geobios *28*, 251–256. https://doi.org/10.1016/S0016-6995(95)80172-3.

61. O'Leary, M.A., Bloch, J.I., Flynn, J.J., Gaudin, T.J., Giallombardo, A., Giannini, N.P., Goldberg, S.L., Kraatz, B.P., Luo, Z.X., Meng, J., et al. (2013). The placental mammal ancestor and the post-K-Pg radiation of placentals. Science *339*, 662–667. https://doi.org/10.1126/science.1229237.

62. Westerhold, T., Röhl, U., Donner, B., and Zachos, J.C. (2018). Global extent of early Eocene hyperthermal events: a new Pacific benthic foraminiferal isotope record from Shatsky Rise (ODP Site 1209). Paleoceanogr. Paleoclimatol. *33*, 626–642. https://doi.org/10.1029/2017PA003306.

63. Davies, K.T.J., Bates, P.J.J., Maryanto, I., Cotton, J.A., and Rossiter, S.J. (2013). The evolution of bat vestibular systems in the face of potential antagonistic selection pressures for flight and echolocation. PLoS One *8*, e61998. https://doi.org/10.1371/journal.pone.0061998.

64. Spoor, F., Bajpai, S., Hussain, S.T., Kumar, K., and Thewissen, J.G.M. (2002). Vestibular evidence for the evolution of aquatic behaviour in early cetaceans. Nature *417*, 163–166. https://doi.org/10.1038/417163a.

65. Arbour, J.H., Curtis, A.A., and Santana, S.E. (2019). Signatures of echolocation and dietary ecology in the adaptive evolution of skull shape in bats. Nat. Commun. *10*, 2036. https://doi.org/10.1038/s41467-019-09951-y.

66. Gunnell, G.F., Worsham, S.R., Seiffert, E.R., and Simons, E.L. (2009). *Vampyravus orientalis* Schlosser (Chiroptera) from the early Oligocene (Rupelian), Fayum, Egypt - body mass, humeral morphology and affinities. Acta Chiropterol. *11*, 271–278. https://doi.org/10.3161/150811009X485512.

67. Giannini, N.P., Gunnell, G.F., Habersetzer, J., and Simmons, N.B. (2012). Early evolution of body size in bats. In Evolutionary History of Bats: Fossils, Molecules and Morphology, G.F. Gunnell, and N.B. Simmons, eds. (Cambridge University Press), pp. 530–555. https://doi.org/10.1017/CBO9781139045599.017.

68. Safi, K., Meiri, S., and Jones, K.E. (2013). Evolution of body size in bats. In Animal Body Size: Linking Pattern and Process across Space, Time, Taxonomic Group, F.A. Smith, and S.K. Lyons, eds. (University of Chicago Press), pp. 95–115. https://doi.org/10.7208/chicago/9780226012285.003.0005.

69. Moyers Arévalo, R.L., Amador, L.I., Almeida, F.C., and Giannini, N.P. (2020). Evolution of body mass in bats: insights from a large supermatrix phylogeny. J. Mamm. Evol. *27*, 123–138. https://doi.org/10.1007/s10914-018-9447-8.

70. Russell, D.E., and Sigé, B. (1970). Révision des chiroptères lutétiens de Messel (Hesse, Allemagne). Palaeovertebrata *3*, 83–182. https://doi.org/10.18563/pv.3.4.83-182.

71. Wiens, J.J. (2009). Paleontology, genomics, and combined-data phylogenetics: can molecular data improve phylogeny estimation for fossil taxa? Syst. Biol. *58*, 87–99. https://doi.org/10.1093/sysbio/syp012.

72. Gatesy, J., O'Grady, P., and Baker, R.H. (1999). Corroboration among data sets in simultaneous analysis: hidden support for phylogenetic relationships among higher level artiodactyl taxa. Cladistics *15*, 271–313. https://doi.org/10.1111/j.1096-0031.1999.tb00268.x.

73. Gatesy, J., Amato, G., Norell, M., DeSalle, R., and Hayashi, C. (2003). Combined support for wholesale taxic atavism in gavialine crocodylians. Syst. Biol. *52*, 403–422. https://doi.org/10.1080/10635150390197037.

74. Lee, M.S., and Camens, A.B. (2009). Strong morphological support for the molecular evolutionary tree of placental mammals. J. Evol. Biol. *22*, 2243–2257. https://doi.org/10.1111/j.1420-9101.2009.01843.x.

75. Reeder, T.W., Townsend, T.M., Mulcahy, D.G., Noonan, B.P., Wood, P.L., Jr., Sites, J.W., Jr., and Wiens, J.J. (2015). Integrated analyses resolve conflicts over squamate reptile phylogeny and reveal unexpected placements for fossil taxa. PLoS One *10*, e0118199. https://doi.org/10.1371/journal.pone.0118199.

76. Mongiardino Koch, N., and Thompson, J.R. (2021). A total-evidence dated phylogeny of Echinoidea combining phylogenomic and paleontological data. Syst. Biol. *70*, 421–439. https://doi.org/10.1093/sysbio/syaa069.

77. Ronquist, F., Huelsenbeck, J., and Teslenko, M. (2011). MrBayes version 3.2 manual: tutorials and model summaries. https://gensoft.pasteur.fr/docs/mrbayes/3.2.7/Manual_MrBayes_v3.2.pdf.

78. Ronquist, F., Klopfstein, S., Vilhelmsen, L., Schulmeister, S., Murray, D.L., and Rasnitsyn, A.P. (2012). A total-evidence approach to dating with fossils, applied to the early radiation of the Hymenoptera. Syst. Biol. *61*, 973–999. https://doi.org/10.1093/sysbio/sys058.

79. Horovitz, I. (1999). A phylogenetic study of living and fossil platyrrhines. Am. Mus. Novit. *3269*, 1–40. https://digitallibrary.amnh.org/items/49a56b80-c62e-457a-8be5-2d7b6bd6977a.

80. Wilkinson, M. (2003). Missing entries and multiple trees: instability, relationships, and support in parsimony analysis. J. Vertebr. Paleontol. *23*, 311–323. https://doi.org/10.1671/0272-4634(2003)023[0311:MEAMTI]2.0.CO;2.

81. Cobbett, A., Wilkinson, M., and Wills, M.A. (2007). Fossils impact as hard as living taxa in parsimony analyses of morphology. Syst. Biol. *56*, 753–766. https://doi.org/10.1080/10635150701627296.

82. Bapst, D.W. (2013). When can clades be potentially resolved with morphology? PLoS One *8*, e62312. https://doi.org/10.1371/journal.pone.0062312.

83. Shi, J.J., and Rabosky, D.L. (2015). Speciation dynamics during the global radiation of extant bats. Evolution *69*, 1528–1545. https://doi.org/10.1111/evo.12681.

84. Amador, L.I., Moyers Arévalo, R.L., Almeida, F.C., Catalano, S.A., and Giannini, N.P. (2018). Bat systematics in the light of unconstrained analyses of a comprehensive molecular supermatrix. J. Mamm. Evol. *25*, 37–70. https://doi.org/10.1007/s10914-016-9363-8.

85. Vaughan, T.A. (1959). Functional morphology of three bats: *Eumops*, *Myotis*, *Macrotus*. Misc. publ. Univ. Kans. Mus. Nat. Hist. *12*, 1–153.

86. Smith, J.D. (1972). Systematics of the chiropteran family Mormoopidae. Misc. publ. Univ. Kans. Mus. Nat. Hist. *56*, 1–132.

87. Schlosser-Sturm, E., and Schliemann, H. (1995). Morphology and function of the shoulder joint of bats (Mammalia: Chiroptera). J. Zool. Syst. Evol. Res. *33*, 88–98. https://doi.org/10.1111/j.1439-0469.1995.tb00961.x.

88. Henson, O.W. (1970). The ear and audition. In Biology of Bats, W.A. Wimsatt, ed. (Academic Press), pp. 181–263.

89. Ekdale, E.G. (2013). Comparative anatomy of the bony labyrinth (inner ear) of placental mammals. PLoS One *8*, e66624. https://doi.org/10.1371/journal.pone.0066624.

90. Schuller, G., and Pollak, G. (1979). Disproportionate frequency representation in the inferior colliculus of Doppler-compensating greater horseshoe bats: evidence for an acoustic fovea. J. Comp. Physiol. *132*, 47–54. https://doi.org/10.1007/BF00617731.

91. Sulser, R.B., Patterson, B.D., Urban, D.J., Neander, A.I., and Luo, Z.X. (2022). Evolution of inner ear neuroanatomy of bats and implications for echolocation. Nature *602*, 449–454. https://doi.org/10.1038/s41586-021-04335-z.

92. Cox, P.G., and Jeffery, N. (2010). Semicircular canals and agility: the influence of size and shape measures. J. Anat. *216*, 37–47. https://doi.org/10.1111/j.1469-7580.2009.01172.x.

93. Brooke, M.dL., Hanley, S., and Laughlin, S.B. (1999). The scaling of eye size with body mass in birds. Proc. R. Soc. Lond. B *266*, 405–412. https://doi.org/10.1098/rspb.1999.0652.

94. Pedersen, S.C. (1993). Cephalometric correlates of echolocation in the Chiroptera. J. Morphol. *218*, 85–98. https://doi.org/10.1002/jmor.1052180107.

95. Pedersen, S.C. (1998). Morphometric analysis of the chiropteran skull with regard to mode of echolocation. J. Mammal. *79*, 91–103. https://doi.org/10.2307/1382844.

96. Miller, K.G., Browning, J.V., Schmelz, W.J., Kopp, R.E., Mountain, G.S., and Wright, J.D. (2020). Cenozoic sea-level and cryospheric evolution from deep-sea geochemical and continental margin records. Sci. Adv. *6*, eaaz1346. https://doi.org/10.1126/sciadv.aaz1346.

97. Sigé, B., and Legendre, S. (1983). L'histoire des peuplements de chiroptères du bassin méditerranéen: l'apport comparé des remplissages karstiques et des dépôtsfluvio-lacustres. Mém Biospéol *10*, 209–225.

98. Hand, S.J., and Sigé, B. (2018). A new archaic bat (Chiroptera: Archaeonycteridae) from an Early Eocene forest in the Paris Basin. Hist. Biol. *30*, 227–236. https://doi.org/10.1080/08912963.2017.1297435.

99. Collinson, M.E., and Hooker, J.J. (2003). Paleogene vegetation of Eurasia: framework for mammalian faunas. Deinsea *10*, 41–84.

100. Vaughan, T.A. (1970). The skeletal system. In Biology of Bats, *1*, W.A. Wimsatt, ed. (Academic Press), pp. 97–138. https://doi.org/10.1016/B978-0-12-758001-2.50008-3.

101. Sigé, B., Habersetzer, J., and Storch, G. (1998). The deciduous dentition and dental replacement in the Eocene bat *Palaeochiropteryx tupaiodon* from Messel: the primitive condition and beginning of specialization of milk teeth among Chiroptera. Lethaia *31*, 349–358. https://doi.org/10.1111/j.1502-3931.1998.tb00525.x.

102. Altringham, J.D. (1996). Bats: Biology and Behaviour (Oxford University Press).

103. Zukal, J., Berkova, H., Bandouchova, H., Kovacova, V., and Pikula, J. (2017). Bats and caves: activity and ecology of bats wintering in caves. In Cave Investigation, S. Karabulut, and M. Cengiz, eds. (IntechOpen). https://doi.org/10.5772/intechopen.69267.

104. Geiser, F. (2020). Seasonal expression of avian and mammalian daily torpor and hibernation: not a simple summer–winter affair†. Front. Physiol. *11*, 436. https://doi.org/10.3389/fphys.2020.00436.

105. Bisson, I.A., Safi, K., and Holland, R.A. (2009). Evidence for repeated independent evolution of migration in the largest family of bats. PLoS One *4*, e7504. https://doi.org/10.1371/journal.pone.0007504.

106. Wilkinson, G.S., and South, J.M. (2002). Life history, ecology and longevity in bats. Aging Cell *1*, 124–131. https://doi.org/10.1046/j.1474-9728.2002.00020.x.

107. Wilkinson, G.S., and Adams, D.M. (2019). Recurrent evolution of extreme longevity in bats. Biol. Lett. *15*, 20180860. https://doi.org/10.1098/rsbl.2018.0860.

108. Tanalgo, K.C., Oliveira, H.F.M., and Hughes, A.C. (2022). Mapping global conservation priorities and habitat vulnerabilities for cave-dwelling bats in a changing world. Sci. Total Environ. *843*, 156909. https://doi.org/10.1016/j.scitotenv.2022.156909.

109. Maugoust, J., and Orliac, M.J. (2023). 3D models related to the publication: A 50-million-year-old, three-dimensionally preserved bat skull supports an early origin for modern echolocation. MorphoMuseuM, e217. https://doi.org/10.18563/journal.m3.217.

110. Ekdale, E.G., and Racicot, R.A. (2015). Anatomical evidence for low frequency sensitivity in an archaeocete whale: comparison of the inner ear of *Zygorhiza kochii* with that of crown Mysticeti. J. Anat. *226*, 22–39. https://doi.org/10.1111/joa.12253.

111. Spoor, F., and Thewissen, J.G.M. (2008). Comparative and functional anatomy of balance in aquatic mammals. In Sensory Evolution on the Threshold, Adaptations in Secondarily Aquatic Vertebrates, J.G.M. Thewissen, and S. Nummela, eds. (University of California Press), pp. 257–284. https://doi.org/10.1525/9780520934122-017.

112. Spoor, F., Garland, T., Krovitz, G., Ryan, T.M., Silcox, M.T., and Walker, A. (2007). The primate semicircular canal system and locomotion. Proc. Natl. Acad. Sci. USA *104*, 10808–10812. https://doi.org/10.1073/pnas.0704250104.

113. Schneider, C.A., Rasband, W.S., and Eliceiri, K.W. (2012). NIH Image to ImageJ: 25 years of image analysis. Nat. Methods *9*, 671–675. https://doi.org/10.1038/nmeth.2089.

114. Wiley, D.F., Amenta, N., Alcantara, D.A., Ghosh, D., Kil, Y.J., and Delson, E. (2007). Landmark editor version 3.6: Institute for Data Analysis and Visualization (University of California).

115. Cignoni, P., Callieri, M., Corsini, M., Dellepiane, M., Ganovelli, F., and Ranzuglia, G. (2008). MeshLab: an open-source mesh processing tool. Sixth Eurographics Italian Chapter Conference, 129–136.

116. Lebrun, R. (2018). MorphoDig, an open-source 3D freeware dedicated to biology. https://hal.science/hal-01876987/file/S16_10_Lebrun.pdf.

117. Lanfear, R., Frandsen, P.B., Wright, A.M., Senfeld, T., and Calcott, B. (2017). Partitionfinder 2: new methods for selecting partitioned models of evolution for molecular and morphological phylogenetic analyses. Mol. Biol. Evol. *34*, 772–773. https://doi.org/10.1093/molbev/msw260.

118. Goloboff, P.A., and Catalano, S.A. (2016). TNT version 1.5, including a full implementation of phylogenetic morphometrics. Cladistics *32*, 221–238. https://doi.org/10.1111/cla.12160.

119. Hammer, O., Harper, D.A.T., and Ryan, P.D. (2001). PAST: paleontological statistics software package for education and data analysis. Palaeontol. Electron. *4*, 4.

120. Swofford, D.L. (2003). PAUP*. Phylogenetic analysis using parsimony (* and other methods). Version 4 (Sinauer Associates).

121. R Core Team (2021). R: A Language and Environment for Statistical Computing (R Foundation for Statistical Computing).

122. Motani, R., and Schmitz, L. (2011). Phylogenetic versus functional signals in the evolution of form-function relationships in terrestrial vision. Evolution *65*, 2245–2257. https://doi.org/10.1111/j.1558-5646.2011.01271.x.

123. Maugoust, J., Beck, R.M.D., Hand, S.J., and Orliac, M.J. (2023). Supplementary analytical data for the article entitled "A 50-million-year-old, three-dimensionally preserved bat skull supports an early origin for modern echolocation" by Suzanne J. Hand, Jacob Maugoust, Robin M.D. Beck, and Maëva J. Orliac. Zenodo. https://doi.org/10.5281/zenodo.8176111.

124. Spoor, F., and Zonneveld, F. (1998). Comparative review of the human bony labyrinth. Yrbk. J. Physiol. Anthropol. *107*, 211–251. https://doi.org/10.1002/(SICI)1096-8644(1998)107:27+<211::AID-AJPA8>3.0.CO;2-V.

125. Simmons, N.B., Seiffert, E.R., and Gunnell, G.F. (2016). A new family of large omnivorous bats (Mammalia, Chiroptera) from the Late Eocene of the Fayum Depression, Egypt, with comments on use of the name "Eochiroptera". Am. Mus. Novit. *3857*, 1–43. https://doi.org/10.1206/3857.1.

126. Revilliod, P.A. (1917). Contribution à l'étude de chiroptères des terraine tertiaires. Première partie. Mém Soc. Géol Fr. Paléontol *43*, 1–58.

127. Russell, D.E., Louis, P., and Savage, D.E. (1973). Chiroptera and Dermoptera of the French Early Eocene. Univ. Calif. Publ. Geol. Sci. *95*, 1–57.

128. Harrison, D.L., and Hooker, J.J. (2010). Late Middle Eocene bats from the Creechbarrow Limestone Formation, Dorset, Southern England with description of a new species of *Archaeonycteris* (Chiroptera: Archaeonycteridae). Acta Chiropterol. *12*, 1–18. https://doi.org/10.3161/150811010X504554.

129. Smith, T., Rana, R.S., Missiaen, P., Rose, K.D., Sahni, A., Singh, H., and Singh, L. (2007). High bat (Chiroptera) diversity in the Early Eocene of India. Naturwissenschaften *94*, 1003–1009. https://doi.org/10.1007/s00114-007-0280-9.

130. Storch, G., Sigé, B., and Habersetzer, J. (2002). *Tachypteron franzeni* n. gen., n. sp., earliest emballonurid bat from the Middle Eocene of Messel (Mammalia, Chiroptera). Paläontol. Z. *76*, 189–199. https://doi.org/10.1007/BF02989856.

131. Smith, J.D., and Storch, G. (1981). New Middle Eocene bats from the Grube Messel near Darmstadt, W Germany (Mammalia: Chiroptera). Senckenb. Biol. *61*, 153–168.

132. Bajpai, S., Kapur, V.V., Thewissen, J.G.M., Tiwari, B.N., and Das, D.P. (2005). First fossil marsupial from India: Early Eocene *Indodelphis* n. gen. and *Jaegeria* n. Gen. from Vastan lignite mine, District Surat, Gujarat. J. Palaeontol. Soc. India *50*, 147–151.

133. Maitre, E., Sigé, B., and Escarguel, G. (2008). A new family of bats in the Paleogene of Europe: systematics and implications for the origin of emballonurids and rhinolophoids. N. Jahrb. Geol. Paläontol. Abh. *250*, 199–216. https://doi.org/10.1127/0077-7749/2008/0250-0199.

134. Sigé, B. (2011). *Cryptobune* nov. gen., chiroptère carnivore des phosphorites du Quercy, SW France. Bull. Soc. Hist. Nat. Toulouse *147*, 47–54.

135. Weithofer, A. (1887). Zur Kenntniss der fossilen Cheiropteren der französischen phosphorite. Sitzb K. Akad. Wissensch Wein *96*, 341–361.

136. Hand, S.J., Sigé, B., and Maitre, E. (2012). *Necromantis* Weithofer, 1887, large carnivorous Middle and Late Eocene bats from the French Quercy Phosphorites: new data and unresolved relationships. In Evolutionary history of Bats: Fossils, Molecules, and Morphology, G.F. Gunnell, and N.B. Simmons, eds. (Cambridge University Press), pp. 210–251. https://doi.org/10.1017/CBO9781139045599.007.

137. Forster Cooper, C. (1932). On some mammalian remains from the lower Eocene of the London Clay. Ann. Mag. Nat. Hist. Lond. *10*, 458–467. https://doi.org/10.1080/00222933208673518.

138. Beard, K.C., Sigé, B., and Krishtalka, L. (1992). A primitive vespertilionoid bat from the early Eocene of central Wyoming. C. R. Acad. Sci. II *314*, 735–741.

139. Smith, R., and Russell, D.E. (1992). Mammifères (Marsupialia, Chiroptera) de l'Yprésien de la Belgique. Bull. Inst. R. Sci. Natl. Belg. Sci. Terre *62*, 223–227.

140. Heller, F. (1935). Fledermäuse aus der eozänen Braunkohle des Geiseltales bei Halle a. S. Nova. Acta Leopold N. Folge *2*, 301–314.

141. Sigé, B., and Russell, D.E. (1980). Compléments sur les chiroptères de l'Eocène moyen d'Europe. Les genres *Palaeochiropteryx* et *Cecilionycteris*. Palaeovertebrata. Mém Jubil R Lavocat *1980*, 81–126.

142. Tong, Y.-S. (1997). Middle Eocene small mammals from Liguanqiao Basin of Henan province and Yuanqu Basin of Shanxi province, Central China. Palaeontologia Sinica, Series C *26*, 1–256.

143. Sigé, B. (1991). Rhinolophoidea et Vespertilionoidea (Chiroptera) du Chambi (Eocène inférieur de Tunisie). Aspects biostratigraphique, biogéographique et paléoécologique de l'origine des chiroptères modernes. N. Jahrb. Geol. Paläontol. Abh. *182*, 355–376. https://doi.org/10.1127/njgpa/182/1991/355.

144. Hand, S.J., Sigé, B., Archer, M., and Black, K.H. (2016). An evening bat (Chiroptera: Vespertilionidae) from the late Early Eocene of France, with comments on the antiquity of modern bats. Palaeovertebrata *40*, e2. https://doi.org/10.18563/pv.40.2.e2.

145. Russell, D.E., Galoyer, A., Louis, P., and Gingerich, P.D. (1988). Nouveaux vertébrés sparnaciens du Congolmérat de Meudon à Meudon, France. C.R. Acad. Sci. Paris Sér *II*, 429–433.

146. Tejedor, M.F., Czaplewski, N.J., Goin, F.J., and Aragón, E. (2005). The oldest record of South American bats. J. Vertebr. Paleontol. *25*, 990–993. https://doi.org/10.1671/0272-4634(2005)025[0990:TOROSA]2.0.CO;2.

147. Marandat, B. (1991). Mammifères de l'Ilerdien moyen (Eocène inférieur) des Corbières et du Minervois (Bas-Languedoc, France). Syst. Biostratigraphie Corrélations Palaeovertebrata *20*, 55–144.

148. Czaplewski, N.J., and Morgan, G.S. (2012). New basal noctilionoid bats (Mammalia: Chiroptera) from the Oligocene of subtropical North America. In Evolutionary History of Bats: Fossils, Molecules and Morphology, G.F. Gunnell, and N.B. Simmons, eds. (Cambridge University Press), pp. 162–209. https://doi.org/10.1017/CBO9781139045599.006.

149. Giannini, N.P., and Simmons, N.B. (2007). The chiropteran premaxilla: a reanalysis of morphological variation and its phylogenetic interpretation. Am. Mus. Novit. *3585*, 1–44. https://doi.org/10.1206/0003-0082(2007)3585[1:TCPARO]2.0.CO;2.

150. Hand, S.J. (1998). *Xenorhinos*, a new genus of Old World leaf-nosed bats (Microchiroptera: Hipposideridae) from the Australian Miocene. J. Vertebr. Paleontol. *18*, 430–439. https://doi.org/10.1080/02724634.1998.10011070.

151. Barone, R. (1986). Anatomie Comparée Des Mammifères Domestiques. Tome 1 Ostéologie (Vigot).

152. Giannini, N.P., Wible, J.R., and Simmons, N.B. (2006). On the cranial osteology of Chiroptera. I. *Pteropus* (Megachiroptera: Pteropodidae). Bull. Am. Mus. Nat. Hist. *295*, 1–134. https://doi.org/10.1206/0003-0090(2006)295[0001:OTCOOC]2.0.CO;2.

153. Butler, P.M. (1948). On the evolution of the skull and teeth in the Erinaceidae, with special reference to fossil material in the British Museum. Proc. Zool. Soc. Lond. *118*, 446–500. https://doi.org/10.1111/j.1096-3642.1948.tb00389.x.

154. Butler, P.M. (1956). The skull of *Ictops* and the classification of the Insectivora. Proc. Zool. Soc. Lond. *126*, 453–481. https://doi.org/10.1111/j.1096-3642.1956.tb00449.x.

155. Barghoorn, S.F. (1977). New material of *Vespertiliavus* Schlosser (Mammalia, Chiroptera) and suggested relationships of emballonurid bats based on cranial morphology. Am. Mus. Novit. *2618*, 1–29.

156. Hand, S.J. (1997). *Hipposideros bernardsigei*, a new hipposiderid (Mammalia: Microchiroptera) from the Australian Miocene and a reconsideration of the monophyly of related species groups. Münchner Geowiss Abh. *34*, 73–92.

157. Sanchez-Villagra, M.R., and Wible, J.R. (2002). Patterns of evolutionary transformation in the petrosal bone and some basicranial features in marsupial mammals, with special reference to didelphids. J. Zoological System. *40*, 26–45. https://doi.org/10.1046/j.1439-0469.2002.00173.x.

158. O'Leary, M.A. (2010). An anatomical and phylogenetic study of the osteology of the petrosal of extant and extinct artiodactylans (Mammalia) and relatives. Bull. Am. Mus. Nat. Hist. *335*, 1–206. https://doi.org/10.1206/335.1.

159. Billet, G., and Muizon de, C.D. (2013). External and internal anatomy of a petrosal from the late Paleocene of Itaborai, Brazil, referred to Notoungulata (Placentalia). J. Vertebr. Paleontol. *33*, 455–469. https://doi.org/10.1080/02724634.2013.722153.

160. Morgan, G.S., and Czaplewski, N.J. (2003). A new bat (Chiroptera: Natalidae) from the early Miocene of Florida, with comments on natalid phylogeny. J. Mammal. *84*, 729–752. https://doi.org/10.1644/1545-1542(2003)084<0729:ANBCNF>2.0.CO;2.

161. Wible, J.R., and Davis, D.L. (2000). Ontogeny of the chiropteran basicranium, with reference to the Indian false vampire bat, *Megaderma lyra*. In Ontogeny, Functional Ecology, and Evolution of Bats, R.A. Adams, and S.C. Pedersen, eds. (Cambridge University Press), pp. 214–246. https://doi.org/10.1017/CBO9780511541872.007.

162. West, C.D. (1985). The relationship of the spiral turns of the cochlea and the length of the basilar membrane to the range of audible frequencies in ground dwelling mammals. J. Acoust. Soc. Am. *77*, 1091–1101. https://doi.org/10.1121/1.392227.

163. Manoussaki, D., Chadwick, R.S., Ketten, D.R., Arruda, J., Dimitriadis, E.K., and O'Malley, J.T. (2008). The influence of cochlear shape on low-frequency hearing. Proc. Natl. Acad. Sci. USA *105*, 6162–6166. https://doi.org/10.1073/pnas.0710037105.

164. Legendre, S. (1984). Identification de deux sous-genres fossiles et compréhension phylogénique du genre *Mormopterus* (Molossidae, Chiroptera). C. R. Acad. Sci. Paris *2*, 715–720.

165. Hand, S.J. (1990). First tertiary molossid (Microchiroptera: Molossidae) from Australia: its phylogenetic and biogeographic implications. Mem. Qd Mus. *28*, 175–192.

166. Menu, H., and Sigé, B. (1971). Nyctalodontie et myotodontie, importants caractères de grades évolutifs chez les chiroptères entomophages. C. R. Acad. Sci. Paris *272*, 1735–1738.

167. Louzada, N.S.V., Nogueira, M.R., and Pessôa, L.M. (2019). Comparative morphology and scaling of the femur in yangochiropteran bats. J. Anat. *235*, 124–150. https://doi.org/10.1111/joa.12996.

168. Davis, J.C. (1986). Statistics and Data Analysis in Geology (John Wiley & Sons).

169. Simpson, G.G., Roe, A., and Lewontin, R.C. (1960). Measures of dispersion and variability. In Quantitative Zoology, Revised Edition, G.G. Simpson, A. Roe, and R.C. Lewontin, eds. (Brace and Company, Inc.), pp. 78–95.

170. Akaike, H. (1974). A new look at the statistical model identification. IEEE Trans. Autom. Control *19*, 716–723. https://doi.org/10.1109/TAC.1974.1100705.

171. Dempster, A.P., Laird, N.M., and Rubin, D.B. (1977). Maximum likelihood from incomplete data via the EM algorithm. J. R. Stat. Soc. B *39*, 1–22. https://doi.org/10.1111/j.2517-6161.1977.tb01600.x.

172. Orr, D.J.A., Teeling, E.C., Puechmaille, S.J., and Finarelli, J.A. (2016). Patterns of orofacial clefting in the facial morphology of bats: a possible naturally occurring model of cleft palate. J. Anat. *229*, 657–672. https://doi.org/10.1111/joa.12510.

173. Upham, N.S., Esselstyn, J.A., and Jetz, W. (2019). Inferring the mammal tree: species-level sets of phylogenies for questions in ecology, evolution, and conservation. PLoS Biol. *17*, e3000494. https://doi.org/10.1371/journal.pbio.3000494.

174. Smith, M.R. (2023). TreeSearch: morphological phylogenetic analysis in R. R J. *14*, 305–315. https://doi.org/10.32614/RJ-2023-019.

175. Farris, J.S., and Kluge, A.G. (1979). A botanical clique. Syst. Zool. *28*, 400–411. https://doi.org/10.2307/2412596.

176. Farris, J.S. (1983). The logical basis of phylogenetic analysis. In Advances in Cladistics II, N.I. Platnick, and V.A. Funk, eds. (Columbia University Press), pp. 7–36.

177. de Pinna, M.C.C. (1991). Concepts and tests of homology in the cladistic paradigm. Cladistics *7*, 367–394. https://doi.org/10.1111/j.1096-0031.1991.tb00045.x.

178. Begun, D.R. (2007). How to identify (as opposed to define) a homoplasy: examples from fossil and living great apes. J. Hum. Evol. *52*, 559–572. https://doi.org/10.1016/j.jhevol.2006.11.017.

179. Templeton, A.R. (1983). Phylogenetic inference from restriction endonuclease cleavage site maps with particular reference to the evolution of humans and the apes. Evolution *37*, 221–244. https://doi.org/10.1111/j.1558-5646.1983.tb05533.x.

180. Goldman, N., Anderson, J.P., and Rodrigo, A.G. (2000). Likelihood-based tests of topologies in phylogenetics. Syst. Biol. *49*, 652–670. https://doi.org/10.1080/106351500750049752.

181. de Queiroz, A., and Gatesy, J. (2007). The supermatrix approach to systematics. Trends Ecol. Evol. *22*, 34–41. https://doi.org/10.1016/j.tree.2006.10.002.

182. Manos, P.S., Soltis, P.S., Soltis, D.E., Manchester, S.R., Oh, S.H., Bell, C.D., Dilcher, D.L., and Stone, D.E. (2007). Phylogeny of extant and fossil Juglandaceae inferred from the integration of molecular and morphological data sets. Syst. Biol. *56*, 412–430. https://doi.org/10.1080/10635150701408523.

183. Dávalos, L.M., Velazco, P.M., Warsi, O.M., Smits, P.D., and Simmons, N.B. (2014). Integrating incomplete fossils by isolating conflicting signal in saturated and non-independent morphological characters. Syst. Biol. *63*, 582–600. https://doi.org/10.1093/sysbio/syu022.

184. Darlim, G., Lee, M.S.Y., Walter, J., and Rabi, M. (2022). The impact of molecular data on the phylogenetic position of the putative oldest crown crocodilian and the age of the clade. Biol. Lett. *18*, 20210603. https://doi.org/10.1098/rsbl.2021.0603.

185. Lawrence, B.N., Bennett, V.L., Churchill, J., Juckes, M., Kershaw, P., Pascoe, S., Pepler, S., Pritchard, M., and Stephens, A. (2013). Storing and manipulating environmental big data with JASMIN. In Proceedings of the 2013 IEEE International Conference on Big Data (IEEE), pp. 68–75. https://doi.org/10.1109/BigData.2013.6691556.

186. Lewis, P.O. (2001). A likelihood approach to estimating phylogeny from discrete morphological character data. Syst. Biol. *50*, 913–925. https://doi.org/10.1080/106351501753462876.

187. Harrison, L.B., and Larsson, H.C.E. (2015). Among-character rate variation distributions in phylogenetic analysis of discrete morphological characters. Syst. Biol. *64*, 307–324. https://doi.org/10.1093/sysbio/syu098.

188. Stamatakis, A. (2016). The RAxML v8.2.X Manual (Heidelberg Institute for Theoretical Studies).

189. Kealy, S., and Beck, R. (2017). Total evidence phylogeny and evolutionary timescale for Australian faunivorous marsupials (Dasyuromorphia). BMC Evol. Biol. *17*, 240. https://doi.org/10.1186/s12862-017-1090-0.

190. Beck, R.M.D., and Taglioretti, M.L. (2020). A nearly complete juvenile skull of the marsupial *Sparassocynus derivatus* from the Pliocene of Argentina, the affinities of "sparassocynids", and the diversification of opossums (Marsupialia; Didelphimorphia; Didelphidae). J. Mamm. Evol. *27*, 385–417. https://doi.org/10.1007/s10914-019-09471-y.

191. Beck, R.M.D., Voss, R.S., and Jansa, S.A. (2022). Craniodental morphology and phylogeny of marsupials. Bull. Am. Mus. Nat. Hist. *457*, 1–350. https://doi.org/10.1206/0003-0090.457.1.1.

192. Ronquist, F., Teslenko, M., van der Mark, P., Ayres, D.L., Darling, A., Höhna, S., Larget, B., Liu, L., Suchard, M.A., and Huelsenbeck, J.P. (2012). MrBayes 3.2: efficient Bayesian phylogenetic inference and model choice across a large model space. Syst. Biol. *61*, 539–542. https://doi.org/10.1093/sysbio/sys029.

193. Gunnell, G.F., Boyer, D.M., Friscia, A.R., Heritage, S., Manthi, F.K., Miller, E.R., Sallam, H.M., Simmons, N.B., Stevens, N.J., and Seiffert, E.R. (2018). Fossil lemurs from Egypt and Kenya suggest an African origin for Madagascar's aye-aye. Nat. Commun. *9*, 3193. https://doi.org/10.1038/s41467-018-05648-w.

194. Matzke, N.J., and Wright, A. (2016). Inferring node dates from tip dates in fossil Canidae: the importance of tree priors. Biol. Lett. *12*, 20160328. https://doi.org/10.1098/rsbl.2016.0328.

195. Mammal Diversity Database (2022). Mammal diversity database. Version 1.9.1. (Zenodo. https://doi.org/10.5281/zenodo.4139818.

196. Zhang, C., Stadler, T., Klopfstein, S., Heath, T.A., and Ronquist, F. (2016). Total-evidence dating under the fossilized birth-death process. Syst. Biol. *65*, 228–249. https://doi.org/10.1093/sysbio/syv080.

197. Püschel, H.P., O'Reilly, J.E., Pisani, D., and Donoghue, P.C.J. (2020). The impact of fossil stratigraphic ranges on tip-calibration, and the accuracy and precision of divergence time estimates. Palaeontology *63*, 67–83. https://doi.org/10.1111/pala.12443.

198. Beck, R.M.D., and Lee, M.S.Y. (2014). Ancient dates or accelerated rates? Morphological clocks and the antiquity of placental mammals. Proc. Biol. Sci. *281*, 20141278. https://doi.org/10.1098/rspb.2014.1278.

199. Flynn, A.G., Davis, A.J., Williamson, T.E., Heizler, M., Fenley, C.W., Leslie, C.E., Secord, R., Brusatte, S.L., and Peppe, D.J. (2020). Early Paleocene magnetostratigraphy and revised biostratigraphy of the Ojo Alamo Sandstone and Lower Nacimiento Formation, San Juan Basin, New Mexico, USA. GSA Bulletin *132*, 2154–2174. https://doi.org/10.1130/B35481.1.

200. Cohen, K.M., Finney, S.C., Gibbard, P.L., and Fan, J. (2013). The ICS International Chronostratigraphic Chart. Episodes *36*, 199–204. https://doi.org/10.18814/epiiugs/2013/v36i3/002.

201. Kusuhashi, N., Tsutsumi, Y., Saegusa, H., Horie, K., Ikeda, T., Yokoyama, K., and Shiraishi, K. (2013). A new Early Cretaceous eutherian mammal from the Sasayama Group, Hyogo, Japan. Proc. Biol. Sci. *280*, 20130142. https://doi.org/10.1098/rspb.2013.0142.

202. Ho, S.Y.W., and Phillips, M.J. (2009). Accounting for calibration uncertainty in phylogenetic estimation of evolutionary divergence times. Syst. Biol. *58*, 367–380. https://doi.org/10.1093/sysbio/syp035.

203. Sallam, H.M., and Seiffert, E.R. (2020). Revision of Oligocene '*Paraphiomys*' and an origin for crown Thryonomyoidea (Rodentia: Hystricognathi: Phiomorpha) near the Oligocene–Miocene boundary in Africa. Zool. J. Linn. Soc. *190*, 352–371. https://doi.org/10.1093/zoolinnean/zlz148.
204. Xie, W., Lewis, P.O., Fan, Y., Kuo, L., and Chen, M.H. (2011). Improving marginal likelihood estimation for Bayesian phylogenetic model selection. Syst. Biol. *60*, 150–160. https://doi.org/10.1093/sysbio/syq085.
205. Kass, R.E., and Raftery, A.E. (1995). Bayes factors. J. Am. Stat. Assoc. *90*, 773–795. https://doi.org/10.1080/01621459.1995.10476572.
206. Nylander, J.A.A., Ronquist, F., Huelsenbeck, J.P., and Nieves-Aldrey, J.L. (2004). Bayesian phylogenetic analysis of combined data. Syst. Biol. *53*, 47–67. https://doi.org/10.1080/10635150490264699.
207. Pagel, M., and Meade, A. (2004). A phylogenetic mixture model for detecting pattern-heterogeneity in gene sequence or character-state data. Syst. Biol. *53*, 571–581. https://doi.org/10.1080/10635150490468675.
208. Wang, L.G., Lam, T.T.-Y., Xu, S., Dai, Z., Zhou, L., Feng, T., Guo, P., Dunn, C.W., Jones, B.R., Bradley, T., et al. (2020). Treeio: an R package for phylogenetic tree input and output with richly annotated and associated data. Mol. Biol. Evol. *37*, 599–603. https://doi.org/10.1093/molbev/msz240.
209. Paradis, E., and Schliep, K. (2019). ape 5.0: an environment for modern phylogenetics and evolutionary analyses in R. Bioinformatics *35*, 526–528. https://doi.org/10.1093/bioinformatics/bty633.
210. Revell, L.J. (2012). phytools: an R package for phylogenetic comparative biology (and other things). Methods Ecol. Evol. *3*, 217–223. https://doi.org/10.1111/j.2041-210X.2011.00169.x.
211. Maugoust, J. (2022). ULT – useful little things in R. Zenodo. https://doi.org/10.5281/zenodo.6973431.
212. Wickham, H., and Seidel, D. (2020). scales: scale functions for visualization. https://cran.r-project.org/web/packages/scales/index.html.
213. Pennell, M.W., Eastman, J.M., Slater, G.J., Brown, J.W., Uyeda, J.C., FitzJohn, R.G., Alfaro, M.E., and Harmon, L.J. (2014). geiger v2.0: an expanded suite of methods for fitting macroevolutionary models to phylogenetic trees. Bioinformatics *30*, 2216–2218. https://doi.org/10.1093/BIOINFORMATICS/BTU181.
214. Ho, T., L.S., and Ané, C. (2014). A linear-time algorithm for Gaussian and non-Gaussian trait evolution models. Syst. Biol. *63*, 397–408. https://doi.org/10.1093/sysbio/syu005.
215. Paterno, G.B., Penone, C., and Werner, G.D.A. (2018). sensiPhy: an r-package for sensitivity analysis in phylogenetic comparative methods. Methods Ecol. Evol. *9*, 1461–1467. https://doi.org/10.1111/2041-210X.12990.
216. Adams, D.C. (2014). A method for assessing phylogenetic least squares models for shape and other high-dimensional multivariate data. Evolution *68*, 2675–2688. https://doi.org/10.1111/evo.12463.
217. Clavel, J., and Morlon, H. (2020). Reliable phylogenetic regressions for multivariate comparative data: illustration with the MANOVA and application to the effect of diet on mandible morphology in phyllostomid bats. Syst. Biol. *69*, 927–943. https://doi.org/10.1093/sysbio/syaa010.
218. Revell, L.J. (2009). Size-correction and principal components for interspecific comparative studies. Evolution *63*, 3258–3268. https://doi.org/10.1111/j.1558-5646.2009.00804.x.
219. Freckleton, R.P. (2002). On the misuse of residuals in ecology: regression of residuals vs. multiple regression. J. Anim. Ecol. *71*, 542–545. https://doi.org/10.1046/j.1365-2656.2002.00618.x.
220. Freckleton, R.P. (2009). The seven deadly sins of comparative analysis. J. Evol. Biol. *22*, 1367–1375. https://doi.org/10.1111/j.1420-9101.2009.01757.x.
221. Venables, W.N., and Ripley, B.D. (2002). Modern Applied Statistics with S, Fourth Edition (Springer).
222. Orme, D., Freckleton, R., Thomas, G., Petzoldt, T., Fritz, S., Isaac, N., and Pearse, W. (2018). caper: comparative analyses of phylogenetics and evolution in R. https://cran.r-project.org/web/packages/caper/index.html.
223. Pebesma, E. (2018). Simple features for R: standardized support for spatial vector data. R. J. *10*, 439–446. https://doi.org/10.32614/RJ-2018-009.
224. Adams, D.C., Collyer, M.L., Kaliontzopoulou, A., and Baken, E.K. (2021). Geomorph: software for geometric morphometric analyses. https://cran.r-project.org/web/packages/geomorph/citation.html.
225. Baken, E.K., Collyer, M.L., Kaliontzopoulou, A., and Adams, D.C. (2021). geomorph v4.0 and gmShiny: enhanced analytics and a new graphical interface for a comprehensive morphometric experience. Methods Ecol. Evol. *12*, 2355–2363. https://doi.org/10.1111/2041-210X.13723.
226. Arbour, J.H., and Brown, C. (2020). LOST: missing morphometric data simulation and estimation. https://cran.r-project.org/web/packages/LOST/LOST.pdf.
227. Microsoft Corporation, and Weston, S. (2020). foreach: provides foreach looping construct. https://CRAN.R-project.org/package=foreach.
228. Microsoft Corporation, and Weston, S. (2020). doParallel: foreach parallel adaptor for the "parallel" package. https://CRAN.R-project.org/package=doParallel.

STAR★METHODS

KEY RESOURCES TABLE

REAGENT or RESOURCE	SOURCE	IDENTIFIER
Deposited data		
Vielasia sigei holotype and paratypes	This paper; Legendre et al.[50]; Sigé[58]	UM-VIE-250–255, UM-VIE-614, 669–677, UM-VIE-02, 17, 19, 20
Vielasia sigei 3D models of cranium and bony labyrinth	This paper; MorphoMuseuM.com[109]	MorphoMuseuM: https://doi.org/10.18563/journal.m3.217
Character taxon matrix for phylogenetic analysis	This paper; O'Leary et al.[61]	MorphoBank Project 4407 http://morphobank.org/permalink/?P4407
Measurements of *Vielasia* and comparative taxa	This paper; Davies et al.[19,63]; Cox and Jeffery[92]; Ekdale and Racicot[110]; Spoor and Thewissen[111]; Spoor et al.[64,112]	Table 1 and Data S1A, S1F, S1G, S1K, S1M–S1O
Landmark co-ordinate data	This paper; Arbour et al.[65]	Data S1N and S1O
Software and algorithms		
Avizo 9.3	Thermofisher	https://www.thermofisher.com
ImageJ	Schneider et al.[113]	https://imagej.net
Landmark 3.6	Wiley et al.[114]	https://www.cs.ucdavis.edu
3Matic	Materialise	https://www.materialise.com
Meshlab	Cignoni et al.[115]	https://www.meshlab.net/
Meshmixer	Autodesk Inc.	https://meshmixer.com
MorphoDig	Lebrun[116]	https://morphomuseum.com/morphodig
MrBayes 3.2.7a	Ronquist et al.[77]	https://nbisweden.github.io/MrBayes
PartitionFinder 2.2	Lanfear et al.[117]	https://www.robertlanfear.com/partitionfinder/
TNT 1.5	Goloboff and Catalano[118]	https://www.lillo.org.ar/phylogeny/tnt/ https://doi.org/10.1111/cla.12160
PAST 4.05	Hammer et al.[119]	https://www.nhm.uio.no
PAUP* 4.0a169	Swofford[120]	https://paup.phylosolutions.com/
R 4.1.1	R Core Team[121]	https://www.r-project.org
R code	Motani and Schmitz[122]	https://doi.org/10.1111/j.1558-5646.2011.01271.x GitHub https://github.com/lschmitz/phylo.fda
R code (new)	This paper's additional analytical resources[123]	Github https://github.com/jacobmaugoust/Vielasia-sigei_hand-et-al; Zenodo https://doi.org/10.5281/zenodo.8176111

RESOURCE AVAILABILITY

Lead contact

Further information and requests for resources should be directed to and will be fulfilled by the lead contact Robin Beck (R.M.D.Beck@salford.ac.uk).

Materials availability

The holotype and paratype specimens of *Vielasia sigei* are lodged in the collections of Université de Montpellier (Montpellier, France), where the specimen is permanently available for research. The 3D models of the cranium and bony labyrinth of the holotype UM-VIE-250 are available at https://morphomuseum.com (https://doi.org/10.18563/journal.m3.217). Comparative data for other fossil bat taxa/specimens included in our study were retrieved from personal observations and the literature (as indicated in the taxon list provided below), and from O'Leary et al.[61]

Data and code availability

- Data analyzed in our study are publicly available as of the date of publication. Fossil accession numbers are listed herein, and a 3D model of the cranium and bony labyrinth can be accessed from the data repository MorphoMuseuM (see key resources table). For our phylogenetic analyses, the morphological taxon-character matrix is available at MorphoBank Project 4407 (listed in the key resources table), morphological and total evidence matrices formatted for analysis by TNT and MrBayes respectively, and the trees output by analyses of these matrices, are available on a public GitHub repository: https://github.com/jacobmaugoust/vielasia-sigei_hand-et-al and as a Zenodo DOI: https://doi.org/10.5281/zenodo.8176111; all results, trees, and statistics are included in supplemental information (Data S1, S2, and Figures S1–S5).

- All original code has been deposited on a public Github repository: https://github.com/jacobmaugoust/vielasia-sigei_hand-et-al and is available as a Zenodo DOI: https://doi.org/10.5281/zenodo.8176111 as of the date of publication. DOIs are listed in the key resources table.
- Any additional information required to reanalyze the data reported in this paper is available from the lead contact upon request.

EXPERIMENTAL MODEL AND SUBJECT DETAILS

The main subject of this study, the holotype specimen of *Vielasia sigei* (UM-VIE-250; Figures 1, 2, 3, 4, and S1), is a well preserved but damaged cranium containing the petrosal. This fossil specimen, and others assigned here to *V. sigei* (Figures 1 and S1), were all found at the type locality of Vielase, Quercy Phosphorites, southwestern France,[50] and were previously referred to Archaeonycteridae gen. et sp. indet.[50,58]

METHOD DETAILS

Data collection, CT scanning, model reconstruction, and measurements

Three dimensional data acquisition from fossils was performed using the μCT facilities (EasyTom 150 μCT) at the University of Montpellier (MRI, ISEM) with 90 kV and 80 μA at a resolution of 8.93 μm, and a U-CT (Milabs, Utrecht) at UNSW Sydney with 55 kV and 0.17 mA, ultrafocused setting at a resolution of 35-50 μm. Segmentation, visualization, and linear and volumetric measurements were performed using Avizo ® 9.3 (Thermo Fisher Scientific-FEI) and MorphoDig© at the University of Montpellier, and MIMICS 21.0 (Materialise) at UNSW Sydney. MeshLab 2020.12 and Meshmixer (Autodesk Inc.) were used to align meshes of UM-VIE-250 (cranium), UM-VIE-251 (rostrum) and UM-VIE-668 (duplicated and mirrored premaxilla) in order to reconstruct a composite virtual cranial model for inclusion in our 3D geometric morphometric analysis of bat cranial shape (see below). Meshes of UM-VIE-254 and UM-VIE-255 were similarly aligned to reconstruct a composite dentary. Measurements of craniodental material were made on the virtual models using 3Matic 13.0 (Materialise) and on the fossils using a Wild 5MA stereomicroscope with Wild MMS235 Digital length measuring set (accurate to 0.01 mm). Univariate and multivariate analyses of the dental sample were performed in the statistical program PAlaeontological STatistics (PAST 4.05; Data S1A, and see below).

One binning of the μCT dataset was applied prior to skull and bony labyrinth segmentation, resulting in a dataset with a 17.86 μm resolution, using ImageJ v1.48; segmentation was performed using Avizo ® 9.3 tools brush, lasso, and magic wand using varying threshold to remove sediment; model reconstruction was performed using Avizo ® 9.3, with an unconstrained smoothing value of 2.75. Measurements of the bony labyrinth (linear and angles) were made on the virtual model using 3Matic (Materialise), following the methods of Spoor and Zonneveld,[124] Spoor et al.,[64] Ekdale,[89] and Davies et al.[19,63] (Data S1F, and see below); basilar membrane length was measured using 86 approximately equidistantly stationary points (as per Davies et al.[19]; Figure 3A) placed in Landmark 3.6.

Comparative material

In the list below, an asterisk (*) denotes original material examined in addition to (otherwise) primary literature, supplementary photographs and/or scan data from MorphoSource and DigiMorph. Families listed alphabetically. List of institutional abbreviations for specimen numbers follows the taxon list.

AEGYPTONYCTERIDAE: *Aegyptonycteris knightae* Simmons et al.[125] Fayum, Egypt CGM83740*; ARCHAEONYCTERIDAE: *Archaeonycteris trigonodon* Revilliod[126] Grube Messel near Darmstadt, Germany HLMD 1398- Me 33a, b*, HLMD 16069; *A. brailloni* Russell et al.[127] Mutigny and Avenay, Marne, France MNHN Louis-410 Mu, MNHN Louis-432 Mu*, MNHN Bn-751 Av*, MNHN Bn-757 Av* (cast SMF 77/262); *A. pollex* Storch and Habersetzer[39] Grube Messel near Darmstadt, Germany SMNK Me 982*; *A. relicta* Harrison and Hooker[128] Creechbarrow, Dorset, England BMNH M35710/12. ?ARCHAEONYCTERIDAE: ?*Archaeonycteris praecursor* Tabuce et al.[25] Silveirinha Portugal UNLSNC-447*; ?*A. storchi* Smith et al.[129] Vastan lignite mine, Gujarat, India GU/RSR/VAS 140; *Protonycteris gunnelli* Smith et al.[129] Vastan lignite mine, Gujarat, India GU/RSR/VAS 436; *Xylonycteris stenodon* Hand and Sigé[98] Prémontré, France SLP 1 PR73*, SLP 27 PR184*. EMBALLONURIDAE:*Tachypteron franzeni* Storch et al.[130] Grube Messel near Darmstadt, Germany IRSNB BE 4-119a+b. HASSIANYCTERIDAE: *Hassianycteris revilliodi* (Russell and Sigé)[70] Grube Messel near Darmstadt, Germany HLMD 4294 Me 16* (cast SMF 77/269); *H. messelensis* Smith and Storch[131] Grube Messel near Darmstadt, Germany HLMD Me 7480*; *H. magna* Smith and Storch[131] Grube Messel near Darmstadt, Germany HLMD Me 7539*; *H. kumari* Smith et al.[129] Vastan lignite mine, Gujarat, India GU/RSR/VAS 56, GU/RSR/VAS 561. ?HASSIANYCTERIDAE: *Cambaya complexus* Bajpai et al.[132] Vastan lignite mine, Gujarat, India IITR/SB/VLM 435. ICARONYCTERIDAE: *Icaronycteris index* Jepsen[37] Green River Formation, Wyoming, USA YPM-PU 18150* and UW 21481*; *I. gunnelli* Rietbergen et al.[36] Green River Formation, Wyoming, USA AMNH:FM:145747A,B, ROM:Palaeobiology-Vertebrate Fossils:52666; *I. menui* Russell et al.[127] Mutigny and Avenay, Marne, France MNHN Louis-333*, MNHN Louis-Mu*, MNHN Louis-331*, MNHN Louis-380*, MNHN Louis-384*, MNHN Louis-353*, MNHN Louis-357*, MNHN Louis-117*, MNHN Av7201*, MNHN Av6797*, MNHN Av7200*, MNHN Louis-360 Mu*, MNHN Bn-547 Av*, MNHN Bn-340 Av*, MNHN Bn-319 Av* (SMF 77/259–261). ?ICARONYCTERIDAE**:** *Icaronycteris sigei* Smith et al.[129] Vastan lignite mine, Gujarat, India GU/RSR/VAS 137. MIXOPTERYGIDAE: *Carcinipteryx maximinensis* Maitre et al.[133] from St-Maximin, Gard Phosphorites, France, UM-SMXCm A.1.3*, UM-SMXCm A.1.5*. NECROMANTIDAE: *Cryptobune thevenini* Sigé[134] unknown locality, Quercy, France ACQ 140*; *Necromantis adichaster* Weithofer[135] Quercy, France QU16369*, QU16369*; *N. gezei* Hand et al.[136] Cuzal, Quercy, France CUZ-383*; *N. marandati* Hand et al.[136] La Bouffie, Quercy, France BFI-NmA.1.1*, BFINmA. 1.5*. ONYCHONYCTERIDAE: *Onychonycteris finneyi* Simmons et al.[9] Green River Formation, Wyoming, USA, ROM 55351A,B*, AMNH FM 142467*; *Ageina tobieni* Russell et al.[127] Mutigny, Marne, France MNHN Mu 5112*, MNHN Louis-481 Mu* (cast SMF 77/263); *Eppsinycteris anglica* (Forster Cooper)[137] Abbey Wood, London Basin, England BMNH M13776; *Honrovits tsuwape* Beard et al.[138] Wind River Formation, Wyoming, USA CM62640*, CM 62641*; ?*Honrovits joeli* (Smith and Russell)[139] Evere, Belgium IRSNB M 1567 (cast); *Marnenycteris michauxi* Hand et al.[31] Pourcy, France UM POY–11*; *Volactrix simmonsae* Czaplewski et al.[35] Elderberry Canyon, Nevada, USA, USNM PAL 544092, USNM PAL 417351. PALAEOCHIROPTERYGIDAE: *Palaeochiropteryx tupaiodon* Revilliod[126] Grube Messel near Darmstadt, Germany, HLMD Me25* (cast SMF 77/271 and 272), Me 266* (cast SMF 77/273 and 274); *Palaeochiropteryx spiegeli* Revilliod[126] Grube Messel near Darmstadt, Germany HLMD Me32 * (cast SMF 77/270); *Palaeochiropteryx sambuceus* Czaplewski et al.[35] Elderberry Canyon, Nevada, USA, USNM PAL 417350, USNM PAL 706598. *Cecilionycteris prisca* Heller[140] Geiseltal Obere Mittelkohle, Germany, GMH 3965*; *Matthesia germanica* Sigé and Russell[141] Geiseltal Obere Mittelkohle, Germany, GMH 3940*; *Lapichiropteryx xiei* Tong[142] Tuqiaogou, Shanxi province, China IVPP V10204; *Microchiropteryx folieae* Smith et al.[129] Vastan lignite mine, Gujarat, India GU/RSR/VAS 459; *Anatolianycteris insularis* Jones et al.[32] Pontide, Anatolia, Turkey, EOU-UCF-7 and 8. PHILISIDAE: *Dizzya exsultans* Sigé[143] Chambi, Tunisia CB 1–15*. VESPERTILIONIDAE: *Premonycteris vesper* Hand et al.[144] Prémontré, France SLP 29 BS 193*, SLP SLP 29 PE 875*, SLP 29 P E 110*; SLP 29 P E 614*; *Sonor handae* Czaplewski et al.[35] Elderberry Canyon, Nevada, USA, USNM PAL 544091. FAMILY INCERTAE SEDIS: cf. *Archaeonycteris* sp. (*sensu* Smith et al.[28]); cf. *Icaronycteris* sp. in Russell et al.[145] Meudon, France MNHN 16065 Me*; cf. Archaeonycteridae (Sigé[58]; Legendre et al.[50]) Vielase, Quercy, France VIE 19*, VIE 20*. *Australonycteris clarkae* Hand et al.[44] Murgon, Queensland, Australia QM F19147, QM F19149*; *Jaegeria cambayensis* Bajpai et al.[132] Vastan lignite mine, Gujarat, India IITR/SB/VLM/585; Chiropteran in Tejedor et al.[146] Laguna Fría, Chubut Province, Argentina, LIEB-PV 999; Chiroptera indet. 2 in Marandat[147] Fournes, Minervois, France FNR-02*; Eochiroptera in Ravel et al.[29] El Kohol, Algeria UT-KD-02, UT-KD-03; *Altaynycteris aurora* Jones et al.[33] Junggar Basin, Xinjiang, China IVPP V 27157, IVPP V 27158.

Institutional abbreviations

AMNH American Museum of Natural History, New York, USA; BMNH The Natural History Museum, London, UK; CGM Cairo Geological Museum, Egypt; CB Chambi collection, Tunisia; CM Carnegie Museum of Natural History, Pittsburgh, USA; EOU, Eskişehir Osmangazi University, Eskişehir, Turkey; FNR Université de Montpellier II, Fournes Locality Collections, France; GMH Geiseltal Museum, Halle, Germany; GPIMUH Geologisch-Paläontologisches Institut und Museum, Universität Hamburg, Germany; GU/RSR/VAS Garhwal University, Srinigar, India; HLMD Hessisches Landesmuseum, Darmstadt, Germany; IITR/SB/VLM Indian Institute of Technology, Roorkee, India; IRSNB M Institut Royal des Sciences Naturelles de Belgique, Brussels, Belgium; IVPP V Institute of Vertebrate Paleontology and Paleoanthropology, Beijing, China; LIEB-PV Laboratorio de Investigaciones en Evolución y Biodiversidad, Universidad Nacional de la Patagonia San Juan Bosco, Argentina; MNHN Muséum National d'Histoire Naturelle, Paris, France; QM Queensland Museum, Brisbane, Australia; ROM Royal Ontario Museum, Toronto, Canada; SLP, Société Laonnoise de Paléontologie collections, Muséum National d'Histoire Naturelle, Paris, France; SMF Me Senckenberg Museum, Messel Department, Frankfurt, Germany; SMNK Staatliches Museum fur Naturkunde, Karlsruhe, Germany; UM Université de Montpellier II, Montpellier, France; UNLSNC Universidade Nova de Lisboa, Portugal, Silveirinha new collection; USNM PAL, Department of Paleobiology, National Museum of Natural History; UT University of Tlemcen, Tlemcen, Algeria; UW University of Wyoming Museum, Laramie, Wyoming, USA; YPM-PU Princeton University (collections now housed in the Yale Peabody Museum, New Haven, CT, USA).

Differential diagnosis

Vielasia sigei differs from all other bats in the combination of features noted in the Diagnosis (main text). Morphological features distinguishing *V. sigei* from specific bat taxa are given below. See Figure S1 for cranial, mandibular and dental terminology.

The dental and postcranial morphology of *Vielasia sigei* most closely resembles that of early to middle Eocene bats referred to several extinct bat families (or currently unassigned to family). *Vielasia sigei* is distinguished from these groups as follows.

Differs from onychonycterids (species of *Onychonycteris*, *Honrovits*, *Ageina, Eppsinycteris, Marnenycteris* and *Volactrix*) in its upper molars being transversely developed (wider than long rather than nearly square); P4 relatively larger; M3 lacking postmetacrista; p3 relatively larger, and p2 smaller such that p2<p3<p4; m1-3 nyctalodont, cristid obliqua meeting the postvallid at centre; dentary with more vertical anterior margin of coronoid process. Differs additionally from *Volactrix simmonsae* in p3 having two roots. Differs additionally from *E. anglica* in p3 having only two roots and m1 not smaller than m2. Differs additionally from *O. finneyi* in I1 and I2 being of similar size, P2 tiny or absent, P3 relatively larger and with three roots, M1 with ectoflexus, M3 relatively shorter, lower incisors tricuspid, more expanded cochlea, shoulder joint with rudimentary secondary articulation, and capitulum of distal humerus near-aligned with longitudinal axis of shaft (rather than laterally displaced with condyle lateral to lateral ledge of shaft).

Differs from icaronycterids (*Icaronycteris* spp.) in P2 absent or tiny, P3 relatively smaller, P4 relatively larger, M1-3 lacking hypocone, and M3 relatively shorter. Differs additionally from *I. index* in its premaxilla with reduced or absent palatine process, I1-2 not recurved lingually, P4 lacking hypocone, dentary coronoid process with more vertical anterior margin and deeper horizontal ramus with slightly convex ventral margin, more expanded cochlea, shoulder joint with rudimentary secondary articulation and capitulum/articular surface of distal humerus less laterally displaced. Differs additionally from *I. sigei* in its smaller p4 metaconid. Differs additionally from *I. gunnelli* in lacking post-C1 diastema, and in P3 height less than P4 height.

Differs from archaeonycterids (species of *Archaeonycteris*, *Protonycteris* and *Xylonycteris*) in P2 absent or tiny, P3 relatively larger and with three roots, P4 with more lingually expanded heel, M1-3 with weaker cingulae including around heel, m1-3 with more cuspidate entoconid and hypoconulid, cristid obliqua meeting the postvallid at centre. Differs additionally from *Archaeonycteris* spp. in its more expanded cochlea. Differs additionally from *P. gunnelli* and *X. stenodon* in m1-3 nyctalodont, and from *X. stenodon* in its relatively wider lower molars.

Differs from palaeochiropterygids (species of *Palaeochiropteryx*, *Cecilonycteris*, *Matthesia*, *Lapichiropteryx*, *Microchiropteryx*, *Anatolianycteris*, and possibly *Stehlinia*, the latter sometimes referred to Vespertilionoidea[28]) in its P4-M3 more transversely developed, particularly M2 protocone lobe, I1-2 bilobed, lacking cingulum and cingular cuspule, P2 absent or tiny, P3 relatively smaller, P4 T-shaped rather than triangular, M1-2 without hypocone development and without double ectoflexi, m1-3 with relatively narrower talonids, entocristid and postcristid meet at angle of less than 90°. Differs additionally from *L. xiei* (and *Stehlinia* spp.[28]) in its M1-2 with ectoflexus and metastylar shelf, and from *C. prisca* in p4 with metaconid. Differs additionally from *Stehinia minor* in its distal humerus with spherical capitulum further laterally offset and spinous process short, not extending distally beyond the articular surface, and in its broader rostrum, anteriorly convergent [and relatively shorter] upper tooth rows, premaxilla (with palatine process and) without medial cleft, anterior palate margin V-shaped, infraorbital formen dorsal to P4 rather than P3 (see figure 12.5.12 of Habersetzer et al.[47]). Differs additionally from *Anatolianycteris insularis* (see figure 2 of Jones et al.[32]) in its less elongated p4.

Differs from hassianycterids (species of *Hassianycteris*) in its M1-2 with ectoflexus, I1-2 not diamond shaped, P3 with three roots, M1-2 with heels less posterolingually developed, M3 with three roots, p4 with metaconid and longer talonid, m1-3 with relatively narrower talonid and lower entoconid, m3 talonid less reduced, angular process of dentary slimmer, cranium with uninflated braincase. Differs additionally from *H. messelensis* and *H. magna* in P4, p3 and p4 without exceptionally tall primary cusp, from *H. revilliodi* in c1 not recurved, and from *H. magna* in trigonid and talonid cusps not subequal in height.

Differs from *Cambaya complexus* (tentatively referred to Hassianycteridae by Smith et al.[129]) in its shallower dentary without markedly anteroventrally expanded symphysis, p4 with wider (and longer?) talonid, m1-3 with relatively narrower talonid, m1 with talonid narrower than trigonid, angular process of dentary slimmer, inflection point for ascending ramus of dentary ventral (rather than posterior) to m3, with posteroventral margin rounded.

Differs from mixopterygids (species of *Mixopteryx* and *Carcinipteryx*) in its C1 not recurved, P4 T-shaped, M1-2 more transversely developed and without posteriorly directed heel (not quadrate occlusal outline), without protruding mesostyle, postprotocrista meeting base of metacone, three lower incisors, three lower premolars, m1-2 without crestiform hypoconulid, m2 talonid relatively narrower.

Differs from aegyptonycterids (*Aegyptonycteris knightae*) in its M2 being more transversely developed, with deeper ectoflexus, lacking ectostyle between parastyle and centrocrista, without large, bulbous hypocone, lacking large metaconule, postprotocrista not longitudinal to tooth row, lingual and buccal cingulae present; M3 more reduced and without hypocone shelf.

Differs from necromantids (species of *Necromantis* and *Cryptobune*) in its P3 large and with three roots, P4 wider and shorter, M1-2 without enlarged heels, centrocrista reaching buccal border, M3 with premetacrista (and metacone), p3 large, p4 short and with metaconid, and m1-3 nyctalodont. Differs additionally from *N. adichaster* in premaxilla and upper incisors present, P2 absent or tiny, lower incisors present, gracile cranium, angle between basicranium and facial region not pronounced, supraorbital ridges and postorbital processes weak, facial region not with clear pentagonal shield, palate relatively longer with posterior margin posterior to toothrow, unexpanded zygoma, paroccipital not overlying mastoid, horizontal ramus of dentary not exceptionally deep, more expanded cochlea, and distal humerus with relatively smaller, less laterally displaced, capitulum and longer distal spinous process.

Differs from the tanzanycterid *Tanzanycteris mannardi* in its less expanded cochlea (dentition unknown in that species).

Differs from philisids (species of *Philisis*, *Dizzya* and *Witwatia*) in its P4-M3 more transversely developed, M1-2 ectoloph without subparallel cristae and double mesostyle, p4 with metaconid, and m1-3 nyctalodont.

Differs from bat species unassigned to family as follows.

Differs from *Jaegeria cambayensis* (see figure 2 of Smith et al.[129]) in its deeper dentary, p4 with smaller metaconid, m1 talonid narrower than trigonid. Differs from *Chambinycteris pusilli*[30] in its C1 and c1 relatively taller, P3 large with three roots, M1 without posteriorly directed heel, p3 large with two roots, p4 with two roots unfused, dentary with deeper horizontal ramus. Differs from *Drakonycteris glibzegdouensis*[30] in its P3 not massive, M1-2 ectoloph without subparallel cristae, M1 with single mesostyle and strong parastyle, M2 buccal margin directed anteroposteriorly (rather than obliquely), m1-3 with more cuspidate hypoconulid. Differs from *Australonycteris clarkae*[44] in its P4 with parastyle, lingually extended heel/lobe and large protocone/cingular cusp, m1-3 nyctalodont. Differs from *Altaynycteris aurora* (see figure 2 of Jones et al.[33]) in its M1-2 with deep ectoflexus and presence of heel.

Differs in its m1-3 nyctalodont from early Eocene indeterminate bat taxa such as:?*Archaeonycteris* sp., Meudon, Paris Basin[145]; Eochiroptera indet. 2 (see pl. 5 of Marandat[147]), Fournes, southern France; chiropteran indet. from Laguna Fria, Argentina[146]; and Eochiroptera indet. from El Kohol, Algeria (see figures 3–4 of Ravel et al.[29]). Differs additionally from the El Kohol eochiropteran its M1-3 with smaller paracone and narrower cingulum.

Vielasia sigei differs from modern bat species in its (archaic) dental morphology. This suite of features includes: molariform dP4 and dp4, P4 paracone tall, twice height of M1 paracone, P4 protocone medial to paracone, M1-3 transversely developed (wider than long), anteroposteriorly narrow, tall cusps and deep valleys, large protocone and lingually extended heel without hypocone, M1-2 with buccal and anterolingual cingula, M1 stylar shelf narrow (less than 50% width of tooth), metacone more lingual than paracone, protocone tall (more than 80% height of metacone), postprotocrista extending buccally to metacone base, M2 paracone and metacone subequal in height, M2 with tall postprotocrista, M3 large, two-thirds area of M1, p3 tall, large (80-40% area of m1), with paraconid and tall protoconid, subequal to p4 protoconid height, p4 with paracristid, talonid more than one third trigonid length, with hypoconulid, hypoflexid, small entoconid, m1-3 trigonids becoming more mesiodistally compressed from m1 to m3, m1 with low paracristid, only 50-75% height of paracone, metaconid height subequal to protoconid height, talonid subequal in width to trigonid, with postentocristid, m2 with with metaconid height subequal to protoconid height, complete but low protocristid, low weak crest between hypoconid and hypoconulid, hypoconulid above cingulid level, m3 hypoconulid at or near midline of tooth.

Vielasia sigei differs additionally from individual modern bat families as follows.

Differs additionally from pteropodids in its tribosphenic teeth not highly modified (tribosphenic morphology clearly identifiable), premaxilla with at least small flange on palatine process (Figure S1G), cranium with expanded cochlea, shoulder joint with rudimentary second articulation and distal humerus articulation less laterally offset.

Differs additionally from rhinolophids, hipposiderids and rhinonycterids in its premaxilla with nasal process and two incisors, nasal not inflated, cranium with short postorbital process, short p4 with metaconid, dentary with tall ascending ramus, and distal humerus with articular surface less laterally offset. Differs additionally from rhinonycterids and hipposiderids in having three lower premolars, although Eocene hipposiderid species (e.g., *Palaeophyllophora* and *Pseudorhinolopus*) may retain p3. Differs additionally from rhinolophids in its longer hard palate without deep U shaped anterior emargination, large, two-rooted p3, tall coronoid process of dentary, less expanded cochlea, distal humerus without deep ridges and long spinous process, proximal femur with large trochanters and shaft straight.

Differs additionally from rhinopomatids in its rostrum without anterolateral inflations, cranium with short postorbital process, its two upper incisors, C1 relatively larger, two upper premolars, M1-2 without large heel, M3 with metacone, three lower incisors, three lower premolars, anterior lower premolar larger, m1-2 talonid narrower, proximal humerus with hemispherical head, second (though rudimentary) articulation.

Differs additionally from craseonycterids in premaxillae not forming complete ring around narial opening, rostrum without anterolateral inflations, braincase not inflated, with postorbital process, less expanded cochlea, two upper incisors, more than one upper premolar, M1-2 without large heel, M3 with metacone, three lower incisors, three lower premolars, anterior lower premolar larger, m1-2 talonid narrower, dentary with tall ascending ramus, distal humerus articulation less laterally offset and spinous process short.

Differs additionally from megadermatids in premaxilla with well-developed nasal process and bearing incisors, braincase less expanded, more expanded cochlea, C1 without large posterior accessory cusp, M1-2 without large heels, M3 with metacone and premetacrista, three lower incisors, three lower premolars, p4 with metaconid, m1-3 without relatively long, open trigonids and small talonids, proximal humerus with hemispherical head, distal humerus articulation less laterally offset, proximal femur with well-developed trochanters and straight shaft.

Differs additionally from emballonurids in its cranium with less developed postorbital process, without basisphenoid pits, P3 not highly reduced, M1-2 without posteriorly expanded heels, c1 without long posterior heel, three lower premolars, m1-3 talonids relatively narrow, proximal humerus with hemispherical head, and proximal femur with well-developed trochanters and straight shaft. Differs additionally from *Taphozous* spp. in its two upper incisors, three lower premolars, anterior dentary not abruptly shallow. Differs additionally from *Tachypteron franzeni* in its M3 without heel, three lower incisors, relatively taller c1, larger p2, p4 with metaconid and entocristid-like crest on talonid, ventral margin of dentary without marked concavity below incisor region, glenoid fossa of the scapula with secondary articular surface, head of proximal humerus hemispherical, greater tuberosity extending proximally beyond head, distal humerus with spinous process not reaching level of trochlea. Differs additionally from *Pseudovespertiliavus* and *Vespertiliavus* spp. in its m1-3 trigonid not anteroposteriorly compressed, and additionally from *Vespertiliavus* spp. in its three lower premolars, with p4 longer than p2.

Differs additionally from nycterids in premaxilla with nasal process, cranium without basisphenoid depression/pits, more than one upper premolar, M1-2 without posteriorly expanded heels, M3 not strongly reduced, cranium lacking deep frontal depression and very broad supraorbital ridge extending over orbit, c1 tall, three lower premolars, p4 with metaconid, m1-3 with entoconids not markedly reduced, m3 length and width less reduced, dentary with deep horizontal ramus, tall coronoid process and well developed angular process, distal humerus articulation less laterally offset, and proximal femur with well-developed trochanters and straight shaft.

Differs additionally from myzopodids in its premaxilla not fused to rostrum and palatine process not well developed, rostrum relatively wider and with short postorbital process, cranium without basisphenoid pit/s, braincase uninflated, P2 tiny or absent, P3-4 larger, M1-2 with double ectoflexi, large p3 with two roots (and not p2>p3<p4), p4 with metaconid, m1-3 nyctalodont, talonid relatively narrower, distal humerus without bilobed medial process (epitrochlea).

Differs additionally from noctilionoids (noctilionids, mystacinids, mormoopids, phyllostomids, thyropterids, furipterids) in its premaxilla not fused to rostrum and palatine process not well developed.

Differs additionally from noctilionids in its hard palate not extending posteriorly beyond level of M3, I2 in toothrow, more than one upper premolar, M1-2 without enlarged posteriorly directed heels, mesostyle not protruding buccally, three lower incisors, three lower premolars, p4 roots in axis of toothrow, m1-3 nyctalodont, talonid narrower, cristid obliqua does not reach lingual border of tooth, coronoid process of dentary taller than condyloid process, ventral margin of horizontal ramus less convex, proximal humerus with hemispherical head, distal humerus with less expanded medial process.

Differs additionally from mystacinids in its short, wide rostrum, postorbital process, uninflated braincase, two upper (small) incisors, M1-2 without double ectoflexi, three lower incisors, three lower premolars, m1-3 nyctalodont, dentary with tall ascending ramus, distal humerus with spherical rather than narrow central capitulum, broad medial process and short spinous process, proximal femur with less proximally extended trochanters.

Differs additionally from mormoopids in its cranium with short postorbital process, uninflated braincase/taller rostrum, M1-2 without posteriorly enlarged heels, without double ectoflexi, p4 with metaconid, p4>p3>p2, coronoid process of dentary tall, taller than condyloid process, m1-3 talonid narrower, proximal femur with well-developed/unreduced trochanters. Differs additionally from *Pteronotus* spp. in m1-3 nyctalodont.

Differs additionally from phyllostomids in its p4 with tall metaconid. Differs additionally from frugivorous stenodermatines and carolliines, and sanguivorous desmodontines, in its unmodified dilambdodont dentition, and from nectivorous glossophagines, brachyphyllines and phyllonycterines in its short, broad rostrum and unreduced teeth.

Differs additionally from thyropterids in its cranium with wider rostrum and postorbital process, P2 absent, larger c1, m1-3 talonid relatively narrower, and from furipterids in its large C1 and p3 with two roots. Differs from both in its uninflated braincase, dentary with tall coronoid process much higher than condyloid process, angular process digit-shaped, and deeper horizontal ramus.

Differs additionally from extinct speonycterids in its M1-2 not square in occlusal outline, without broad heel, its large p3, m3 with hypoconulid, dentary with deep horizontal ramus, and femur with unreduced trochanters.[148]

Differs additionally from vespertilionoids (vespertilionids, natalids, miniopterids, cistugids, molossids) in its premaxilla not fused to rostrum and palatine process not well developed.

Differs additionally from vespertilionids in p4>p3>p2, proximal humerus with greater tuberosity less proximally extended and less well-developed secondary articulation with scapula, distal humerus with spherical capitulum, proximal femur with widely splayed trochanters. Differs additionally from the Early Eocene vespertilionids *Premonycteris vesper* and *Sonor handae* in its nyctalodont m1-3, and additionally from *S. handae* in its p3 having two roots.

Differs additionally from natalids in its short, wide rostrum, uninflated braincase, orbit not reduced and infraorbital canal not elongated, P2 tiny or absent, p4>p3>p2 (not p4=p3=p2), m1-3 talonid narrower, dentary with condyloid process lower than coronoid process and deep horizontal ramus, proximal humerus with less well-developed secondary articulation with scapula, proximal femur not laterally bent and trochanters not greatly reduced.

Differs additionally from miniopterids in its uninflated braincase, deeper, shorter and wider rostrum, I1 and I2 of similar size, C1 large, M1-2 without posteriorly directed heels, p4 large, p4>p3>p2, m1-3 talonid narrower, deeper horizontal ramus, tall coronoid process with condyloid process lower than coronoid process, proximal humerus with less deep fossa for supraglenoid tuberosity of the scapula and head hemispherical, distal humerus with spherical capitulum and only short spinous process, proximal femur with widely splayed trochanters.

Differs additionally from cistugids in its large p3 with two roots (not p4>p3<p2) and m1-3 nyctalodont.

Differs additionally from molossids in its cranium with postorbital process, two (small) upper incisors, three lower premolars with roots not oblique in toothrow, tall coronoid process of dentary, only rudimentary second articulation in shoulder joint, distal humerus with spherical capitulum and short spinous process, and proximal femur lacking hook-like process on greater trochanter and lesser trochanter less proximally extended.

DESCRIPTION

Cranium

General outline and proportions (Figures 1 and S1; Table 1) – The cranium is small (GSL 18.29 mm without premaxilla; Table 1) and gracile. It is partly damaged anteriorly (anterior snout broken), ventrally (right pterygoid wing missing) and posteriorly (left petrosal, left exoccipital and ventral two thirds of left side of supraoccipital missing). In dorsal view (Figures 1B and S1A), the cranium is slightly constricted in the interorbital region, with braincase and rostrum of approximately equal length. The braincase enlarges immediately posterior to the orbits for the first half of the braincase, then is rather quadrate in outline. The maximal width is attained in the posterior part of the zygomatic arches and, without them, at the posterior extremity of the cranium (across mastoids). Interorbital width is approximately one third maximal cranium width (zygomatic), and one half maximal width excluding the zygomatic arches (mastoid). In lateral view (Figures 1C and S1B), the cranium is rather flat dorsoventrally; there is no marked dip in height in the interorbital region, nor any conspicuous change in basicranial angle, i.e., between palate and basicranium. Except for a slight median bulge, the dorsal outline is straight in lateral view and the maximal height of the cranium occurs posteriorly; rostral height is only slightly lower than braincase height (Table 1). The occipital surface is flat and forms a marked angle with the dorsal surface. Ventrally (Figures 1A and S1C), the petrosal is relatively large (>25% mastoid width) and the promontorium does not well reflect the shape of the cochlear canal.

Rostrum (Figures 1B, 1C, 1E, S1A, S1B, and S1G) – Dorsally, a pentagonal frontal shield is defined by low supraorbital ridges ending in postorbital processes and slightly concave frontals with two supraorbital foramina and anteriorly directed grooves that issue from these foramina. The point of junction of the ridges is posterior to maximum interorbital constriction (minimum interorbital width), the crests formed between them meeting in an angle of ~40 degrees. The anterior frontal fossa at the point of bifurcation of the supraorbital ridges appears to be only slightly depressed. Between and anterior to paired supraorbital foramina, is a small single foramen. Rostral inflations are present laterally but poorly inflated. The infraorbital canal runs from a large foramen in the anteroventral floor of the orbit, exiting anteriorly in an equally large foramen dorsal to P4. At the rostrum's anterodorsal margin, the nasals do not meet at their most anterior point, giving the anterior margin a scalloped appearance. In anterior view, the nasal aperture is almost as tall as wide (Figure S1G).

Premaxilla (Figures 1F and S1G) – The premaxilla is known from an isolated specimen, UM-VIE-668. The premaxilla body is just deeper than the long roots of its two incisors I1 and I2. The nasal process, which appears to have been of constant width throughout its depth, is directed posterodorsally but broken caudally with the posterodorsal part missing. Nevertheless, judging from rostrum UM-VIE-251, the right and left premaxillae did not meet dorsally, with the nasals dorsally bridging the gap between them. The premaxilla articulates with the facial portion of the maxilla along a relatively long maxilloincisive margin and, based on UM-VIE-251, probably a much shorter nasoincisive margin. The bone margins of UM-VIE-668 and UM-VIE-251 (and UM-VIE-250) indicate that the maxilloincisive articulation was not fused or sutured (no interlocking of the intervening bones[149]), but fibrous/ligamentous. Left and right premaxillae appear to have approached or been in contact with each other at the interincisive suture ventrally, and probably loosely connected to each other by ligaments. At the point of contact, a short midline flange (which may be broken caudally) is directed toward the anterior margin of the palate (Figure S1G). This could suggest at least partial ossification of a medial flange of the palatine process. However, there is no evidence of a process extending from the anterior margin of the palate and, while some bony division of the median incisive fissure might have occurred anteriorly, it evidently did not occur posteriorly. The premaxilla appears to have been proclivous, its anterior margin extending anteriorly beyond the level of the upper canine root.

Palate (Figures 1A and S1C) – The hard palate is relatively short and broad. The tooth rows are roughly parallel anteriorly (C1-P3) but from P4 they diverge posteriorly, such that the width of the posterior palate is much greater than the anterior palate. The anterior edge of the palate is v-shaped, with the deepest part of the V (its more posterior point) being level with the midpoint of C1 length; there is no median spine. The palate's posterior border has two small lateral indentations that extend anteriorly to the level of the M3 protocone. The posterior extension of the midline is level with the posterior face of M3. The maximum length of the palate extends to this level. The palate is slightly concave posteriorly (in anteroposterior profile). Palatal foramina occur medial to the anterior face of M1 and M2–3. The posterior margin of the palate appears scalloped, with a median projection marking the posterior extent of the vomer.

Orbit (Figures 1C and S1B) – The orbit is rather large, and bears several openings in its anterior floor. Major ones are identified hereafter. There is a concavity in the anteorbital bar,[150] of moderate size, here identified as the lacrimal fossa for the lacrimal sac. It quickly extends straight through the maxillary bone and opens in the lateral wall of the nasal cavity; this canal is the nasolacrimal duct. This configuration is found in other mammals.[151] Ventromedially to the lacrimal fossa is a wide maxillary foramen: it narrows anteriorly, then rises a bit dorsally (under the anteorbital bar) and exits anteriorly to the anteorbital bar, through the infraorbital foramen. The latter foramen is therefore at the other side of the lacrimal fossa on the anteorbital bar. On the dorsal surface of this bar are also two small pits, which could be the lacrimal foramina. The anteroventral surface of the orbit, posteriorly to the maxillary foramen and above the molars, is pierced by several alveolar foramina. There are also three openings medially to the lacrimal fossa and to the maxillary foramen. One is large, wider than tall, of irregular outline, and is located just at the transition between the horizontal and transverse processes of the palatine (sensu[152]), and just posteriorly to the maxillary. A second opening, small and rounded, is retrieved just laterally to the anterior end of the first. Both open posterodorsally. The third, of same shape and size, is posterior to the second: it lies just ventrolaterally to the internal choanae and opens posteriorly. The first is the orbitonasal foramen. It is a rather uncommon feature in mammals: it is described in insectivorous mammals[153,154] where it is a foramen of similar position. According to Barone[151] and to Giannini et al.,[152] the second opening is the sphenopalatine foramen and the third is the minor palatine foramen (posterior palatine foramen in Barghoorn[155]). We thus disagree with some of the foramina Barghoorn (figure 6)[155] recognized: his unnamed foramen is the sphenopalatine foramen, and his sphenopalatine foramen is rather the lacrimal fossa. The third foramen is the posterior opening of a short palatine canal of anteroposterior orientation. This canal opens anteriorly through the major palatine foramen between M2 and M3.

Interorbital and internal nares regions – The narrowest point (Figures 1A, 1B, S1A, and S1C) of the interorbital region is located at the level of M3, just anterior to the internal nares. The point where supraorbital crests unite is located posteriorly to this narrowest point, at the middle point of the broken zygomatic arch (Figure S1A), and forms the slight bulge of the dorsal outline in lateral view (Figure S1B). In lateral view (Figure S1B), the?ethmoidal foramen is marked, just posteriorly and ventrally to the supraorbital ridge. The foramen for the anterior opening of the orbitotemporal canal is also present, small, located dorsally to the ethmoidal foramen and at the narrowest point of the interorbital region. In ventral view (Figure S1C), the posterior part of the palate is salient ventrally and forms a transverse ridge or postpalatine torus between the M3s. Posteriorly, the pterygoids and palatines together form raised and straight pterygoid wings, gradually decreasing in height posteriorly, and with a small hamular process. The following general observations can be made about the internal nasal skeleton. In the nasal cavity, the ossified nasal septum is well preserved, as are the roots of the turbinals on the internal surfaces of the ethmoid, nasal and maxillary bones. Ossified remnants of the fragile turbinals themselves and the laminae are also present. Posterodorsally, three to four ethmoturbinals are present in a relatively large ethmoturbinal recess. The lamina horizontalis is present and extends laterally, separating the ethmoturbinal recess from the nasopharyngeal passage ventrally. A maxilloturbinal is also apparent, and possibly a frontoturbinal and/or lamina semicircularis. A detailed comparative study of *Vielasia*'s internal nasal skeleton and cribiform plate is being prepared.

Zygomatic arch (Figures 1A–1C and S1A–S1C) – The entire left zygomatic arch is missing, as is the jugal of the right zygomatic arch. In dorsal view, the zygomatic arch diverges posteriorly and seems only curved at its squamosal part, being otherwise rather straight. In lateral view, the zygomatic arch originates dorsal to the tooth row and rises posteriorly along a straight line. Its posterior extremity is continuous with a ridge running along the squamosal, the mastoid portion of the petrosal and the paroccipital process.

Cranial vault (Figures 1B, 1C, S1A, and S1B) – The braincase is rather large but only slightly bulbous laterally. It enlarges quickly posteriorly in its anterior half, then only very slightly until its posterior end. There are two large, shallow holes located dorsally, close to the sagittal midline, at two thirds of the length. They open in the endocranial cavity on their anterior and lateral sides; these holes may be the openings for the transverse sinus (or diploic transverse sinus in Hand[156]). The supraorbital crests are slightly raised, the sagittal crest is low to absent anteriorly then taller posteriorly; the lambdoid crest is distinct in its whole length, until reaching the mastoid portion of the petrosal. A detailed comparative study of *Vielasia*'s endocranial cast is in preparation for separate publication.

Glenoid (Figures 1A and S1C) – The glenoid fossa is flat, and twice as wide as long. A tall postglenoid process forms the posterior margin of the articular surface, and it protrudes ventrally, perpendicular to the glenoid fossa. Posterolateral to this process is a large postglenoid foramen, the opening of the capsulo-parietal emissary vein.

Temporal region – Posterior to the glenoid region, the squamosal continues as a curved plate until reaching the mastoid portion of the petrosal (Figures S1A and S1B). It shows a ridge, not tall but marked, which is continuous with the lateral edge of the zygomatic arch anteriorly and with a shallow ridge on the mastoid portion of the petrosal posteriorly. Its posterior part is the posttympanic process, and it contacts the anterior margin of the paroccipital process of the mastoid portion of the petrosal. Its dorsal suture with the parietal is not visible. The parietal contributes to the lambdoid crest but is notched at the lateral extremity of the latter, a part of the mastoid portion of the petrosal being therefore visible. The epitympanic recess is present on the medial surface of the posterior curved plate of the squamosal. It is located posterodorsally to the glenoid foramen.

Basicranial foramina, basicranium and occipital region (Figures 1A, 1D, and S1C–S1E) – The anteriormost basicranial foramen is the optic foramen. It is large, slightly wider than long and opens in the orbitosphenoid, which constitutes the bony bar separating it from the sphenorbital fissure.[152] The latter mostly extends within the alisphenoid. This fissure is ovoid in shape and of constant width. The sphenorbital bridge, i.e., the median portion separating the left and right sphenorbital fissures, is very wide and the latter are further apart than the two optic foramina. Moreover, the two fissures diverge anteriorly (the sphenorbital bridge widens anteriorly). Posteriorly is the oval foramen. It is oval in shape (the major axis of the two foramina converge anteriorly), and of moderate size, smaller than the optic foramen. The alisphenoid surrounds it except medially, where a ridge of the presphenoid forms its medial wall. This sharp ridge is continuous with the pterygoid wing anteromedially and with a broad and very shallow ridge on the lateral aspect of the glenoid fossa posterolaterally. There is no separate round foramen, the latter being most probably confluent with the sphenorbital fissure. There are several foramina around the petrosal. One is located anterolaterally to it and is large; it is the pyriform fenestra. The notch antero-medial to the pyriform fenestra at the anterior end of the transpromontorial sulcus is the carotid foramen. The apex of the promontorium contacts the basisphenoid laterally and the basioccipital medially. There is a wide but slim aperture between a contact point with the basisphenoid and another with the basioccipital. These apertures are undetermined yet. Medially to the petrosal, the long and thin basicochlear fissure separates it from the basioccipital. Finally, there is an almond-shaped aperture, located posteriorly to the promontorium (encompassed between the petrosal and the exoccipital); it is the jugular foramen. These apertures are not confluent, and clearly separated by connections between the petrosal and other basicranial bones. The hypoglossal foramen opens in the exoccipital bone, anteroventrally, and is located just posteromedially to the jugular foramen. Of the foramen magnum, only remains its ventral and right margins. It seems ovoid in shape, with a flat ventral base, and is wider than high (Figures S1C and S1E). The exoccipital participates to the paracondylar process together with the posterior part of mastoid of the petrosal. The occipital condyle is narrow, weakly projected ventrally with a small dorsal expansion. Its external margin is thick and shows two concave surfaces, one posteriorly to the hypoglossal foramen, and another postero-medially to the paracondylar process. There is a groove between the posterior aspect of the petrosal and the ventral margin of the foramen magnum, throughout the basioccipital and the exoccipital. This groove is deeper between the occipital condyle and the paroccipital process, at the condyloid fossa. Dorsally, the supraoccipital forms marked and developed lambdoid crests when contacting the parietals. These crests, in occipital view (Figure S1E), are straight and diagonal in orientation; the lateral bulge of the cranial cavity is visible in this view. In lateral view, the supraoccipital is only slightly concave in its dorsal half, giving a general straight and vertical shape to the posterior face of the cranium. There is a large aperture in its most lateral part, where lies the mastoid portion of petrosal. This aperture follows the anterior and medial edges of the mastoid but do not contact it, there is a wide gap in the location of the mastoid foramen, this structure could be refered to as the "mastoid aperture."

Petrosal (Figures 1D and S1B–S1E; Data S1F) – The auditory bulla, stylohyal, and auditory ossicles are missing. Only the right petrosal is preserved in situ (Figure S1C). Its pars cochlearis contacts the basicranium through four bone contacts (see above). On the ventrolateral surface, the fenestra cochleae and fenestra vestibuli (ventromedially and dorsolaterally respectively) are large openings (Figure S1D). The fenestra vestibuli is oval, longer than wide. The fenestra cochleae is bean-shaped, being much wider than long. Both are separated by a large crista interfenestralis. Just anteriorly to the fenestra vestibuli is an aperture. In Chiroptera, except pteropodid bats,[152] the facial nerve does not run in a canal then a sulcus as in some other mammals (e.g., marsupials,[157] artiodactylans,[158] notoungulates[159]). This aperture therefore corresponds to both the hiatus Fallopii (the exit foramen for the greater petrosal nerve branch of facial nerve VII) and the secondary facial foramen (where, typically, the rest of the facial nerve VII exit and continues along in the facial sulcus). This foramen is hereafter named a facial foramen. The facial sulcus then widens distally: it is firstly a short and narrow groove then a wider area. The posterior end of this area, just dorsolaterally to the base of the fenestra vestibuli, is a short and thick rim. This is a vertical thickening of the facial sulcus floor, and it is pierced by a small foramen which opens in a sinus of the squamosal. A large concave surface follows this rim posteriorly and ventromedially, posterior to the windows; it is very wide, with a bean shape. In this surface are a large and excavated stylomastoid notch dorsolaterally and a shallow stapedial muscle fossa ventromedially. The previous short and thick rim is continuous anteriorly with the floor of the fenestra vestibuli and posteriorly with a bony expansion. The latter corresponds to the tympanohyal attachment site. It is directed antero-ventrally and its apex is large and concave. A very subtle transpromontorial sulcus runs roughly parallel to the facial sulcus on the whole length of the promontorium, at the antero-posterior level of the fenestra vestibuli. There also is a very shallow sulcus for the stapedial artery, just medially to the fenestra vestibuli, joining the transpromontorial sulcus at a right angle. Posteriorly, the transpromontorial sulcus passes just posteriorly to a tall bony spike. Anteriorly to this spike is a small crest that runs along the ventromedial edge of the petrosal and joins the most medial bony contact with the basioccipital. A similar spike or tubercle occurs in natalids (see figure 5 of Morgan and Czaplewski [160]), emballonurids (JM pers. obs.) and molossids (see figure 12 of Henson et al.[88]), and also *Onychonycteris finneyi* (see supplemental figure 2 of Simmons et al.[9]) In natalids, it bears a small hook-like process that in life partly encircles the internal carotid artery and contacts part of the posterior end of the stylohyal.[160] In emballonurids and molossids, it is one of the attachment sites of the auditory bulla and it greatly resembles that described here; we propose a similar function. The shape, location and putative function of this spike are very similar to those of the metatherian rostral tympanic process (as illustrated by Sanchez-Villagra and Wible[157]). Being regarded as a typical marsupial feature, we do not name it in the same way, but this should be emphasized.

There is no epitympanic wing. The antero-lateral surface of the promontorium shows a slight depression corresponding to the area (a ‘‘fossa’’ when more marked) for the tensor tympani muscle insertion. Ventromedially to its posterior ridge is the anterior end of the transpromontorial sulcus. The bulge of the cochlear canal is decipherable on the promontorium surface, but is not very well outlined; there are at least two turns in the cochlear canal, with two and one-quarter turns according to Davies et al.[19] or two and a third turns according to Ekdale.[89] There is a small caudal tympanic process, tubercle-shaped, immediately posteriorly to the fenestra cochleae. Posteriorly to the fenestra cochleae and the caudal tympanic process is a concavity, which corresponds to the petrosal contribution to the anterolateral margin of the jugular foramen. There is a great bony expansion dorsolaterally to the floor of the facial sulcus, which runs anteriorly with a spike directed anteroventrally; it is the tegmen tympani. It is pierced by a foramen of comparable size to that of the fenestrae and which opens posteroventrally; it is probably the foramen for the superior ramus of stapedial artery.[161] The posterior base of the tegmen tympani contributes to the tympanohyal attachment site. The epitympanic recess is not located on the petrosal but on the squamosal (see above), just dorsolaterally to the tegmen tympani. It is quite deep. There is a small but definite fossa incudis, at the posterior extremity of the dorsolateral edge of the tegmen tympani. This fossa is oriented toward the epitympanic recess of the squamosal, ventrolaterally. The mastoid portion of the petrosal bone is massive, of comparable size to that of the pars cochlearis. It is widely exposed ventrally, occipitally, and laterally. The lateral edge of the mastoid forms a large and blunt ridge, the paroccipital process, continuous with the ridge of the squamosal anteriorly (the posttympanic process) and the paracondylar process posteriorly (Figures S1B, S1C, and S1E). The dorsal part is widely visible occipitally and less so laterally, within the ‘‘mastoid aperture’’ (Figure S1E).

Bony labyrinth (Figures 3A and S1F; Data S1F) – The cochlea has a volume of 3.05 mm^3 and comprises ~74% of total inner ear volume. The cochlear canal makes 2.25 turns according to the criterion of Davies et al.,[19] or 2.3 turns following Ekdale.[89] It has a maximum width of 2.50 mm (first turn diameter). The aspect ratio of the cochlear spiral in profile[89] is 0.62; the fenestra vestibuli (oval window) is elliptical (stapedial ratio 1.75). A secondary bony lamina is present along the radial wall of the cochlea canal and appears to extend well beyond the basal turn, almost reaching the apex. The length of the cochlea canal/basilar membrane is ~12.38 mm (method of Davies et al.[19]). The plane of the basal turn of the cochlea forms an angle with the plane of the lateral semicircular canal of ~25 degrees. The canaliculus cochleae for the cochlear aqueduct is small and slightly curved. The dorsal edge of the cochlear fossula bears a horseshoe shaped keel extending anteriorly on the dorsal surface of the cochlear canal and connecting medially to the root of the cochlear aqueduct. The spherical recess is not distinguishable from the elliptical recess in the vestibule. *Vielasia* possesses an anterior excavation for the anterior and lateral ampullae, expressed as a pedestal for the anterior and lateral ampullae on the endocast, as well as a posterior excavation for the posterior ampulla and common crus. The common crus is tall and slender but thicker than the anterior, posterior and lateral canals. The bony channel for the vestibular aqueduct leaves the inner ear directly medial to the vestibular aperture of the common crus. The posterior limb of the lateral semicircular canal opens into the posterior ampulla. The angle between the planes of the anterior and posterior semicircular canals (101 degrees) is greater than between the lateral and posterior canals (89 degrees) which is similar to that between the anterior and lateral canals (90 degrees). The radius of the arc (R^{124}) of the anterior semicircular canal (0.92) is greater than the posterior canal (0.77) which is greater than the lateral semicircular canal arc (0.74).

Hearing frequency range reconstruction (Figure S4; Data S1K and S1L) – Davies et al.[19] performed several multiple regression analyses to assess the relationship between echolocation call parameters (minimum, peak, and maximum frequencies) and putative hearing-related measurements (basilar membrane length, number of cochlear turns, body mass). Their best-fitting model involved only cochlear measurements (basilar membrane length, number of cochlear turns), with empirical formulae provided[19] (see also additional file 1, table s6 of Davies et al.[19]). Using these formulae, we reconstructed echolocation call parameters for *Vielasia sigei*, given its basilar membrane length and number of cochlear turns (Data S1F and S1G), as minimum echolocation frequency of 30.19 kHz, peak echolocation frequency of 41.95 kHz, and maximum echolocation frequency of 55.57 kHz. Davies et al.[19] also inferred low and high limits of hearing frequencies at 30 dB and at 60 dB, using the methods of West[162] and Manoussaki et al.[163] They performed OLS regressions of (1) $\log_{10}$ low limit of hearing frequencies against $\log_{10}$ of the product of basilar membrane length and number of cochlear turns, and of (2) $\log_{10}$ high limit of hearing frequencies against $\log_{10}$ of relative basilar membrane length (i.e., ratio between basilar membrane length and cube root of body mass). Davies et al.[19] used a dataset containing 38 mammal species but discarded two subterranean rodents and two marsupials for performing OLS regressions. The latter dataset contains 14 chiropteran species and 20 non-bat placental mammal species. Davies et al.[19] performed OLS regressions both with and without the 14 bat species, and therefore obtained two OLS regression lines for each of the four cases (low/high limit, 30/60 dB). We re-analysed the data (Data S1K; Figure S4) and estimated low and high limits of hearing frequencies at 30 dB and 60 dB for *Vielasia sigei*, comparing these also to values calculated by Davies et al.[19] for the theoretical "chiropteran ancestor" (Data S1L).

Eye size – Eyeball size in *Vielasia sigei* was estimated as ~2.3 mm diameter or less, using the method of Brooke et al.[93] (and see Thiagavel et al.[22] for validation in bats). Using this method, a virtual spherical eye ball was fitted into the socket in a model of the holotype UM-VIE-250 without touching any part of the skull while the gap between bone and eyeball on the median side was maintained at ~1 mm.

Upper dentition

Dental terminology follows Legendre (see figure 1),[164] Hand,[165] and see Figures S1H and S1I.

Upper incisors – I1 and I2 are known from isolated teeth and are present in premaxilla UM-VIE-668 (Figures 1F and S1G). Both I1 and I2 are small, of similar size, hypsodont, bilobed with the anterior lobe longer and taller than the posterior lobe, and lacking cingula. The incisors in UM-VIE-668 are worn, but I1 has lobes of more equal size (both length and height) than I2 in which the posterior lobe is significantly smaller such that the tooth is nearly caniniform. The root in both I1 and I2 is long, at least 2.5 times crown height. Upper incisors are not particularly reduced, with I1 length in toothrow approximately half M3 length.

Upper canine – In cross-section C1 is anteroposteriorly elongate (Figures 1A, S1C, and S1H). It has a tall, anteriorly placed single cusp (paracone) with two main crests separating its two faces; the posterior crest is sharper that the anterior crest. The lingual face is flat and slightly depressed; the buccal face is convex in section but its distal surface is somewhat flatter. A discontinuous cingulum is well developed around most of the crown but in some specimens attenuates anterobuccally and is absent anteriorly. A small but distinct cingular cuspule is formed where the lingual and buccal cingula meet the cusp's posterior crest.

Upper premolars – UM-VIE-250 and UM-VIE-251 preserve alveoli for two premolars (Figures 1A, S1C, and S1H), interpreted here as P3 and P4. The first upper premolar (P2) is absent in UM-VIE-250 and UM-VIE-251 but an alveolus for a very small, single-rooted tooth in this position is present in UM-VIE-252. P3 is known from several specimens (Table 1). It is a relatively small, three-rooted tooth, round to triangular in occlusal shape. It has a single central cusp that is rounded in section anteriorly and has a sharp posterior crest. A cingulum is well developed around the crown but dissipates buccally where the central cusp is most convex/at the cusp's greatest convexity. P4 is a three-rooted tooth that is conspicuously larger than P3. It is slightly wider than long and T-shaped in occlusal view. It has a tall and sharp buccal cusp (paracone), a low and weakly cuspate parastyle that projects slightly anteriorly and a low rounded and expanded lingual lobe or heel. It has a distinct cingulum along the buccal, anterior, lingual and posterior sides; the anterior cingulum dissipates/is absent in its medial part. The lingual cingulum increases in height anteriorly where it bears a distinct lingual cuspule (protocone). A curved posterobuccal crest (postparacrista) runs from the paracone to the posterobuccal corner of the crown.

Upper molars – There are three upper molars (Figures 1A, S1C, and S1H). M1 is a three-rooted tooth that is much wider than long (mean ratio 1.4; Table 1). The metacone is taller than the protocone which is taller than the paracone. The buccal border has an overall oblique direction with respect to the paracone, and has a single, long, shallow pre-ectoflexus anterior to the mesostyle. The well-developed, crested parastyle projects anterolingually. The postpara- and premetacrista meet close to the buccal cingulum, with the mesostyle no more than a slight elevation of the buccal border crest. The postparacrista and premetacrista meet at an angle of ~60°. The postmetacrista is longer than the premetacrista which is longer than the subequal pre- and postparacrista. The protofossa is closed posteriorly by the postprotocrista which meets the base of the metacone, or in some specimens also extends beyond the metacone and connects with the posterior cingulum. The preprotocrista extends along the anterior flank of the paracone to meet the base of the parastyle in an acute angle. A paraloph, extending from the base of the paracone to the preprotocrista, is variably present. There is no metaloph. The protocone is relatively tall, narrow (anteroposteriorly), and lingually extended. The basal posterior face of the protocone extends lingually and slightly posteriorly, developing as a rounded heel which has a distinct but weak cingulum, best developed anteriorly and posteriorly. There is no hypocone, but a swelling in the posterolingual cingulum is sometimes present (e.g., UM-VIE-250, Figures 1A and S1C). In UM-VIE-250 a depression in the heel's posterior cingulum appears to represent a wear facet for the protoconid of m2. M2 has a similar structure to M1 but differs as follows. M2 is wider than M1 (and is proportionately wider; mean width to length ratio 1.61) and its protocone heel shorter anteroposteriorly. The buccal border, from anterior to posterior, is directed anteroposteriorly rather than obliquely, and this border also has a deeper and longer ectoflexus, more medial in position than in M1. The paracone and metacone are more equal in size, their buccal valleys more similar in area, and the preparacrista, postparacrista and premetacrista more equal in length although still shorter than the postmetacrista. The protocone heel is less posteriorly and more lingually extended, and the basal cingulum more or less continuous around the protocone. M3 is conspicuously wider than long, but narrower than M2 and typically subequal to M1. It retains a metacone, which is lower in height than the paracone and protocone. The preparacrista is longer than the postparacrista which is just longer than the premetacrista; there is no postmetacrista. The tooth has a well-developed, cuspidate and anteriorly directed parastyle. The paracingulum is narrow, as in M1-2, and the protofossa deep. The posterobuccally directed postprotocrista meets the base of the metacone, closing the protofossa. There is no cingulum around the base of the protocone, and no buccal, anterolingual or posterior cingulae.

Dentary and lower dentition

Dentary – The horizontal (mandibular) ramus (UM-VIE-254 and UM-VIE-255) has a slightly convex ventral margin, best seen in UM-VIE-254 (Figures 1G–1H and S1I), but is of uniform medium depth (2.1 mm), approximately equivalent to 1.5 times m1 height. Its symphysis extends posteriorly to mid-p3 (Figures 1I and S1I). The anterior mental foramen occurs below the incisors; the posterior mental foramen occurs below c1-p2. The dentary has a tall ascending ramus, with the condyloid process occurring at a level well dorsal to the tooth row but conspicuously lower than the tall coronoid process. The anterior edge of the coronoid rises nearly vertically, its tip is missing but is at least twice tooth crown height. The well-defined angular process is digit-shaped, more or less in line with the horizontal ramus and occurs at the level of the tooth alveoli. An elongate mandibular foramen opens well ventral to the tooth row. The dental formula is i3, c1, p2, p3, p4, m1-3, where p2 is single rooted and p3–m3 have two roots each.

Lower incisors – No lower incisors are preserved in situ but alveoli in UM-VIE-254 and CT data indicate that three incisors were present (Figures 1G–1I and S1I). Isolated lower incisors (e.g., Figure S1I) are small tri-lobed teeth, longer (in toothrow) than wide, with wide, well-developed basin, brachyodont, without cingulid.

Lower canine – The c1 is anteroposteriorly elongate, and there is a single, tall primary cusp (protoconid) and posteriorly-extended heel (talonid) with a small transverse basin (Figures 1I and S1I). The protoconid's buccal face is convex, while the posterior face is flat or slightly concave. A cingulid is very well developed lingually but is indistinct or absent buccally. Anterolingually, the cingulid joins the vertical anterior crest of the principal cusp in a sweeping curve that extends up the anterolingual face of the canine attenuating at about half cusp height. Posterolingually, the cingulid is lower but still pronounced. A small cingular cuspid is present posteriorly. The root is of similar proportions to the crown.

Lower premolars – The first lower premolar p2 is a single rooted tooth (Figures 1I and S1I). It has a low main cuspid, is longer than wide, elliptical in occlusal view and triangular in lateral view. Cristids run anteriorly and posteriorly from the tip of the main cuspid (protoconid) to small cingular cuspids at the crown's most anterior and posterior points, respectively. The lingual cingulid is stronger than the buccal cingulid but both are distinct. The middle lower premolar p3 is a larger two-rooted tooth (Figures 1G–1I and S1I). In occlusal shape and general proportions, the crown is rectangular, and longer than wide. It consists of a tall main cuspid (protoconid). This cuspid has a cristid running from its tip anterobuccally to a well differentiated paraconid, and a less distinct cristid running posteriorly to a cingular basin. No metaconid is present. There is a discontinuous basal cingulid around the crown which is better developed lingually than buccally where it attenuates approximately midway along the length of the crown, at the greatest convexity of the protoconid. A small but distinct cingular cuspid occurs at the most posterior point of the crown. The posterior lower premolar p4 is a two-rooted tooth similar in length to p3 but conspicuously wider. It consists of a tall main cuspid (protoconid) with a cristid running from its tip anterobuccally to a well differentiated paraconid and a posterior cristid to a less distinct metaconid, the former being smaller and closer than the latter to the main cuspid (protoconid). Variably, a posterior (entocristid-like) cristid continues from the metaconid to the posterolingual cingulid. A basal cingulid is more or less continuous around the crown. A small cingular cuspid projects posteriorly.

Lower molars – In m1, the trigonid is shorter but slightly wider than the talonid (Table 1). The trigonid basin is significantly higher than the talonid basin (Figures 1G, 1I, and S1I). The protoconid is the tallest cuspid followed closely by the metaconid which is taller than the subequal paraconid, hypoconid and entoconid. The hypoconulid is distinct but low; it is lingually situated and the postcristid runs from the hypoconid directly to the hypoconulid, in the nyctalodont pattern.[166] In occlusal view (Figure 1H), the metacristid is straight and almost at right angles to the long axis of the tooth, whereas the paracristid is longer and slightly more curved, reflecting a slightly anteriorly directed paraconid. In posterior view, the angle formed by the metacristid components is less than 90°, whereas that formed along the paracristid is conspicuously more than 90°. The angle formed between the paracristid and metacristid at the protoconid is approximately 50°. The cristid obliqua joins the posterior wall of the trigonid (postvallid) at the centre of the crown, below the junction of the two components of the metacristid, such that the hypoflexid is relatively deep. The anterior, buccal, and posterior cingulid is continuous, but is thinnest around the hypoconid. There is no lingual cingulid. The m2 is described in so far as it differs from m1. The trigonid is more anteriorly compressed such that the angle formed between the paracristid and metacristid at the protoconid is approximately 40°. The lengths of the paracristid and metacristid are more equal than in m1. The talonid cuspids are relatively shorter, such that there is a more conspicuous difference in height between trigonid and talonid cuspids in m2. Compared to m1-2, m3 is a narrower tooth (Table 1), with talonid width conspicuously less than trigonid width. The talonid cuspids are shorter, such that there is more difference in height between trigonid and talonid cuspids than in m1-2. The angle formed between the paracristid and metacristid at the protoconid is approximately 35°. The basal cingulid is briefly absent around the greatest convexity of the hypoconid.

Postcranium

Terminology and orientation for skeletal element morphology follows Vaughan[85] and Smith.[86]

Scapula – UM-VIE-671 represents a fragment of a left scapula (Figure 1K). Few structures are preserved but those include the glenoid fossa, the supraglenoid tuberosity and the bases of the coronoid process (ventral surface) and acromion process (dorsal surface). The glenoid fossa of the scapula is pear-shaped, being narrower cranially than caudally. It is defined by a low lip except dorsomedially where a smooth, poorly developed facet (dorsal articular facet) marks an articulation with the greater tuberosity of the humerus.

Humerus – UM-VIE-672 is the proximal end of a right humerus (Figures 1L and 1M). It is 4.6 mm wide dorsoventrally and 3.5 mm deep mediolaterally without pectoral ridge and ~5 mm deep mediolaterally with pectoral ridge; this fragment is 10.7 mm long. The greater tuberosity is knob-like and extends proximally just beyond the head. The lesser tuberosity is more wing-like, being markedly ventrally extended, and does not extend proximally beyond the head. The head is hemispherical and centred between the tuberosities; it extends caudad only just beyond the shaft. The head is separated from both tuberosities by equally deep grooves, the groove between the head and greater tuberosity being narrower. A shallow fossa is developed anterior to the head and between the two tuberosities but closer to the greater tuberosity. The pectoral ridge is long and tall, its edge turned so that its posterior surface is concave and its medial surface forms the lateral part of the broad, deep bicipital groove. The pectoral ridge meets the shaft distally

~8 mm from the most proximal point of the greater tuberosity. A ventral crest (medial ridge) that runs distally from the base of the lesser tuberosity for ~3 mm is anteriorly concave. A less pronounced crest extends from the distal part of the greater tuberosity before dissipating.

The distal end of the shaft is oval in cross-section (~1.8 x 1.3 mm). UM-VIE-673 represents the distal portion of a left humerus (Figure 1N). It is 4.4 mm wide mediolaterally and 2.4 mm deep anteroposteriorly; this fragment is 6.7 mm long. The articular surface is slightly offset with respect to the shaft so that, in anterior view, both the trochlea and lateral epicondyle rim are just lateral to its medial and lateral edges respectively. The central capitulum is spherical and occupies ~40% the articular surface width. The medial process (epitrochlea) is relatively broad, representing ~30% the width of the articular facets (including distal spinous process representing one-half that width ~17%). The distal spinous process is well separated from the trochlea and short (does not reach the distal articular surface). The trochlea and central capitulum are more prominent than the lateral epicondyle. The trochlea extends slightly further distally than the capitulum; they are separated by a trochlear groove. A ridge extends from this margin proximally along the shaft to enclose, medially, a deep, broad, central radial fossa.

Radius – UM-VIE-674 represents the proximal portion of a left radius (Figure 1O). It is ~2.8 mm wide dorsoventrally and ~2.4 mm deep anteroposteriorly; this fragment is 8.2 mm long. The epiphysis is ~1.7 times as thick as the shaft, and inclined craniad (tilting from the lateral to medial sides) with respect to the long axis of the shaft. In anterior view, the epiphysis is a rounded triangular shape, with the most acute angle being blunt and proximally directed. The surface is concave with the articular facet for the capitulum being large and round, occupying ~60% the width of the articular surface. There is no conspicuous ridge separating articular facets for the capitulum and trochlea. Medial and lateral winged articular processes are similar in size and distally tilted. The anterior flange of the radius articulates with the anterior face of the trochlea, and the posterior flange articulates with the epicondyle anterior face. Posteromedially, there is no clear facet indicating the contact area for the posterior articular facet of the cubitus of the ulna. Immediately distal to the anteromedial part of the distal rim of the articular surface is a deep slit (flexor fossa) into which the tendons for the Mm. triceps and brachii and brachialis would insert. The distal end of the shaft is circular in cross-section (diameter ~1.65 mm).

Femur – UM-VIE-675 represents the proximal portion of a left femur (Figure 1P). It is ~3.2 mm wide mediolaterally, ~1.5 mm deep anteroposteriorly; this fragment is ~4.8 mm long. It is relatively large, its width across the trochanters being 70% of that across the proximal humerus tuberosities. The head of the femur, clearly distinct from the rest of the epiphysis, is spherical, slightly anteromedially directed and has a distinct but shallow fovea capitis. The head is relatively large (diameter ~1.4 mm), slightly wider than the distal shaft, and with its medial edge aligned with the shaft's medial edge. Two well-developed trochanters are located opposite each other but both on the posterior surface of femur. The head lies between the trochanters, along the longitudinal axis of the shaft and extends anteromedially. The trochanters are similar in size and widely spread. They are connected to one another by a weak horizontal ridge across the posterior surface of the femur just distal to the head. The lesser trochanter does not extend proximally beyond the base of the head; the greater trochanter extends further proximally (half head height). Grooves separate the head from the shaft and the greater trochanter. The shaft appears to have been straight, as least proximally. It is slightly flattened such that low crests extend from greater and lesser trochanters. The distal end of the shaft is oval in cross-section (~1.10 x 0.89 mm).

Comparisons of postcranial elements with other stem bats – *Vielasia*'s skeletal elements exhibit specializations for flight found in all bats, extant and extinct (e.g., reorientation of scapular spine, absence of olecranon fossa, supinator ridge and entepicondylar foramen in humerus, elongated radius with respect to humerus, reorientated femur with poorly-developed neck, prominent and proximal head, greater and lesser trochanters equally developed, lack of digital fossa).[9,45,46]

Vielasia's shoulder joint (with hemispherical head on proximal humerus and scapula with correspondingly simple, pear-shaped glenoid cavity) is of a form regarded as the least specialized type among extant bats, as found in (e.g.) pteropodids and rhinopomatids.[87] In *Vielasia*, however, the major tuberosity of the proximal humerus extends proximally beyond the head and a shallow pit receives the greater tuberosity of the scapula's glenoid fossa at stages in wingbeat cycle. These represent specializations that reduce the pronatory movements of the abducted forearm during the downstroke of the wing-beat cycle,[87] possibly facilitating longer time on the wing. Among stem bats a second articulation in the shoulder is better developed in *Hassianycteris* and *Palaeochiropteryx* spp. but not in *Onychonycteris* and *Icaronycteris*[9,46] and possibly not in *Archaeonycteris* (see figure 23 of Russell and Sigé[70]).

Similarly, the elbow joint morphology in *Vielasia* is similar to that found in stem bats. *Vielasia* retains a spherical central capitulum and broad medial epicondyle with low spinous process (indicative of a large medial muscle mass), a morphology also seen in *Icaronycteris*,[46] *Onychonycteris* and *Archaeonycteris* spp. (see figure 24 of Russell and Sigé[70]) and to a less degree in *Palaeochiropteryx* and *Hassianycteris* spp. (in which the spinous process extends to the level of the distal trochlea; see figure 11 of Russell and Sigé[70]). This arrangement enables considerable rotational (anteroposterior and lateral) movement in the joint, facilitating the maneuvrable flight used today by (e.g.) phyllostomids, hipposiderids and pteropodids. In more archaic bats, the articular surface is laterally positioned, with the capitulum either completely or mostly lateral to the lateral edge of the humeral shaft, and the medial edge of the trochlea well lateral to the medial edge of the humeral shaft[46]; this condition is also seen among extant (e.g.) pteropodids, rhinolophoids, phyllostomids, some mormoopids, and in noctilionids. In *Vielasia*, it is a little more specialized: the capitulum lies mostly medial to the lateral edge of the humeral shaft, such that the articular surface is displaced only slightly laterally with respect to the midline of the shaft.

With well developed, broad trochanters, low lesser trochanter and slender, straight shaft, *Vielasia*'s proximal femur is also similar to that of other stem bats including *Icaronycteris* and *Archaeonycteris* spp. (SJH pers. obs.) but differs from the condition in *Palaeochiropteryx* (see figure 15 of Russell and Sigé[70]) in which the head is more proximally directed and the trochanters less splayed. It is similar to that of most extant bat species with generalized roosting habits (i.e., hang from branches or ceilings, cling to vertical surfaces and/or rest in crevices) such as pteropodids, vespertilionids and emballonurids.[85,102] It lacks specializations seen in bats that hang pendant-like, such as mormoopids and rhinolophids (trochanters greatly reduced, head directed proximally), or bats that walk, such as vampires, mystacinids and some molossids (robust shaft, well developed lateral and medial ridges, proximally extended lesser trochanter[167]).

Other specimens referred to *Vielasia sigei* – More than 400 craniodental and postcranial fossil specimens recovered from Vielase locality in the Quercy Phosphorites, southwestern France[50,56–58] appear to be referable to *Vielasia sigei*. Qualitative examination, univariate statistics, mixture analysis and principal components analysis of craniodental specimens in the fossil sample are consistent with the material representing a single species - the common Vielase bat species noted by Legendre et al.[50] and described here as *Vielasia sigei* n. gen. et sp. A second, much smaller bat species is represented by rare teeth, also noted by Legendre et al.[50]; these teeth will be described separately and are not included in the sample analysed here. Univariate and multivariate analyses of 131 complete/measurable craniodental specimens were performed in the statistical program PAlaeontological STatistics (PAST[119,168]), with univariate summary statistics given in Data S1A. Coefficient of variation (CV) values lie within the range expected from a single population, i.e., CV values between 4 to 10,[169] and PCA analysis (using iterative inputation for missing data) also found no evidence of clustering that would suggest the presence of more than one population/sexual dimorphism among isolated teeth referred to this species (Data S1A). For most variables, mixture analysis[170,171] showed no evidence of clustering or dimorphism in the sample of isolated teeth. However, for lower first molars (N=41), mixture analysis did detect two groupings in trigonid widths (m1WT) with means at 1.30 mm and 1.47 mm (prob. 0.536 and 0.464, respectively), and two groupings in talonid widths (m1Wt) with means at 1.20 mm and 1.33 mm (prob. 0.541 and 0.459, respectively) (Data S1A). The well-preserved Vielase fossil tooth sample provides an opportunity to further examine dental variation, including sexual dimorphism, in an early Eocene bat and is the subject of a separate analysis by additional authors.

Unfused premaxilla and familial distinction

In *Vielasia*, the premaxilla contains two relatively large incisors (Figures 1F and S1G), the maximum number found in any bat and the number found in all stem bats. However, unlike all other early Eocene bat taxa in which the morphology is thought to be clear, *Vielasia*'s premaxilla was only loosely attached to the rostrum (see Description above), as it is in many extant bats, including in both yangochiropterans and yinpterochiropterans.[149] In *Vielasia*, the maxilloincisive articulation in the adult bat appears to have been ligamentous, rather than fused or sutured; left and right premaxilla bodies approach one another anteroventrally, or meet in a loose midline interincisive contact; a short medial flange extends caudally from the premaxilla body but a palatine process from the anterior margin of palate is absent (we interpret/score this as palatine process of the premaxilla being reduced or absent); nasal processes of right and left premaxillae do not meet dorsally (nasals bridging the gap); and the anterior edge of the premaxilla extends beyond the level of the upper canine root (proclivous condition[149]). In bats, the variable form of the premaxilla is taxonomically diagnostic among extant and extinct families,[149] and *V. sigei* exhibits a combination of premaxillary features that suggests familial distinction for *Vielasia* may be warranted, but a re-examination of this complex in other stem bats is needed before this can be confirmed as unique. The adaptive or functional significance of a reduced, relatively mobile premaxilla in bats is currently not understood, but possibilities include increased gape, inflight prey capture and manipulation, modulation of echolocation call, noseleaf function, reduced interference with returning echolocation call, and/or olfactory function (as noted by Orr et al.[172] and references therein).

Scoring of premolar positions

Extant and fossil bats have a maximum of three premolars, which have been traditionally identified as P2-4/p2-4 in descriptions of bat comparative anatomy (e.g., Smith et al.,[28] Hand et al.,[31] Czaplewski et al.,[35] Simmons and Geisler,[46] Sigé,[101] Russell et al.,[127] and Hand et al.[144]). To facilitate comparisons between these studies and the description of *Vielasia sigei* presented here, we also refer to bat premolars as P2-4/p2-4 in the descriptive and comparative aspects of our study. However, our craniodental character matrix is based on that of O'Leary et al.,[61] who identified the premolars of bats as comprising P1/p1 P4/p4 and P5/p5 of the ancestral eutherian complement of five premolars; to ensure that we have correctly compared equivalent tooth positions between bats and the non-bat eutherians in our matrix, we have followed O'Leary et al.'s[61] scheme for bat premolars when scoring our dental characters (Morphobank Project 4407, http://morphobank.org/permalink/?P4407).

All of the five known maxillary specimens of *V. sigei* contain two upper premolars (P4 and P5 of O'Leary et al.[61] In four of these five specimens (including the holotype UM-VIE-250; Figures 1A and S1C), there is no sign of, nor space for, P2 (P1 of O'Leary et al.).[61] A fifth maxilla preserves a possible alveolus buccal to the centre of P3 (P4 of O'Leary et al.[61]) which could represent either a tiny, buccally extruded, variably present premolar or a dental atavism (Figure S1H). However, in our phylogenetic analysis, we scored the anteriormost premolar as being absent in *Vielasia sigei*, as this is clearly the modal condition.

PHYLOGENETIC ANALYSES

In order to test the evolutionary relationship of *Vielasia sigei* to other chiropterans (extant and fossil), we carried out a series of phylogenetic analyses using both morphological and total evidence (= combined morphological and molecular) matrices, as follows.

Morphological matrix

Our morphological character list comprised 2665 craniodental characters, which is a reduced version of the 4541 phenomic character matrix of O'Leary et al.[61] (with postcranial, soft tissue, behavioural and developmental characters deleted). We used this matrix as a starting point because it is the largest (in terms of characters) morphological matrix currently available for resolving higher-level relationships within mammals, and because it has already been scored for the early Eocene bats *Onychonycteris finneyi* and *Icaronycteris index*, plus six extant bats that collectively represent all major crown chiropteran lineages, namely: the yinpterochiropteran

Pteropodidae (*Pteropus giganteus*) and Rhinolophoidea (the rhinopomatid *Rhinopoma hardwickii*), and the yangochiropteran Emballonuroidea (the emballonurid *Saccopteryx bilineata* and the nycterid *Nycteris thebaica*), Vespertilionoidea (the vespertilionid *Myotis lucifugus*), and Noctilionoidea (the mormoopid *Pternotus parnelli*) O'Leary et al.[61] As outgroups, we retained from O'Leary et al.'s[61] original matrix the stem eutherians *Maelestes gobiensis*, *Ukhaatherium nessovi*, and *Zalambdalestes lechei*, plus five plesiomorphic members of the same placental superorder to which Chiroptera belongs, namely Laurasiatheria: the early Paleocene *Protungulatum donnae* (a probable stem-euungulate), the early Eocene carnivoramorphan *Vulpavus profectus*, and the extant eulipotyphlan "insectivores" *Solenodon paradoxus* (Solenodontidae), *Erinaceus europaeus* (Erinaceidae), and *Sorex araneus* (Soricidae). We deleted all other non-chiropteran terminals.

To this reduced, chiropteran-focused matrix, we added *Vielasia sigei* and a further 15 early Eocene bats *Ageina tobieni*, *Archaeonycteris trigonodon*, *Ar. brailloni*, ?*Ar. storchi, Cambaya complexus*, *Eppsinycteris anglica*, *Hassianycteris messelensis*, *Honrovits joeli*, *H. tsuwape*, *Icaronycteris index*,?*I. sigei*, *Microchiropteryx folieae*, *Onychonycteris finneyi*, *Palaeochiropteryx tupaiodon*, *Protonycteris gunnelli*; for family assignment see list of Comparative material, above). We did not include fossil species whose taxonomy is under review (e.g.,?*I. menui* which appears to represent a mixed species sample; SJH in prep.). Our final matrix therefore comprised 22 chiropteran ingroup terminals (six extant bats, and 16 fossil bats representing all five currently recognised early Eocene families[32]), and eight non-chiropteran outgroup terminals (three extant, five fossil). Percentage completeness of our terminals for the craniodental matrix is given in Data S1B. In the final 2665 craniodental character matrix, 925 characters (34.7%) were parsimony informative, and a further 433 characters (16.2%) were variable but non-parsimony informative. Following O'Leary et al.,[61] all characters were specified as unordered.

Maximum parsimony analyses of morphology matrix

We analysed the full craniodental matrix using maximum parsimony (MP), as implemented in TNT 1.5,[118] using a two-stage search strategy: an initial "New Technology" search with Sectorial Search, Ratchet, Drift, and Tree Fusing (with default settings for each of these) that was run until the same minimum tree length was found 100 times, followed by a "traditional" search using tree bisection reconnection within the trees saved from the first stage, saving a maximum of 100,000 trees. Multiple most parsimonious trees were summarised using strict consensus, and support values were calculated for clades in the consensus topology using 2000 bootstrap replicates, with bootstrap values reported as absolute frequencies.

This analysis recovered two most parsimonious trees (length = 3165 steps), the strict consensus of which is shown in Figure S2A. Relationships among extant bats found in this analysis are partially incongruent with current molecular evidence: specifically, the pteropodid *Pteropus* was placed as the first branch within Chiroptera (rather than in a clade with the rhinolophoid *Rhinopoma*), separate from a clade comprising the remaining, laryngeally-echolocating extant bats ("microbats") – a basal position for pteropodids is characteristic of most unconstrained morphology-only analyses of chiropteran phylogeny.[36,46] In this analysis, the fossil Eocene bats form a paraphyletic assemblage that is more closely related to the clade of laryngeally-echolocating extant bats than to *Pteropus*. Notably, *Vielasia* and *Cambaya* (known from a single 54 Ma dentary from the Cambay Formation at Vastan mine, India, that has been tentatively referred to Hassianycteridae[28,129]) form a weakly supported (bootstrap <50%) clade, and this in turn is weakly supported (bootstrap < 50%) as sister to the extant echolocating clade. Monophyly of the extant echolocating clade, to the exclusion of *Pteropus* and all Eocene fossil bats, is strongly supported (bootstrap = 97%). Besides the basal position of *Pteropus*, the overall topology in this analysis is broadly similar to our dated total evidence analysis (Figure 2).

The fact that maximum parsimony analysis of the full craniodental matrix results in a topology that conflicts with current molecular evidence in placing *Pteropus* as the sister to all other bats (extant and fossil), rather than in a clade with our representative rhinolophoid, *Rhinopoma* (e.g., Shi and Rabosky[83] and Amador et al.[84]), raises questions about the ability of this matrix to accurately resolve bat phylogeny. To further investigate this, we filtered the matrix to retain only those characters that are fully compatible (= show no homoplasy) with the current molecular consensus view of bat phylogeny, as follows. We deleted all fossil taxa from the matrix, and then analysed the extant-only matrix using MP in TNT, using the same two-stage search strategy as before, and applying a "molecular scaffold" that enforced the monophyly of the following clades, based on recent molecular studies (e.g., Meredith et al.,[2] Álvarez-Carretero et al.,[6] and Upham et al.[173]): Eulipotyphla (our extant outgroup taxa *Sorex*, *Solenodon* and *Erinaceus*), crown Chiroptera (our six extant bat terminals), Yinpterochiroptera (*Pteropus* and *Rhinopoma*), Yangochiroptera (*Saccopteryx*, *Nycteris*, *Myotis*, and *Pteronotus*), and Emballonuroidea (*Saccopteryx* and *Nycteris*). This procedure resulted in a single most parsimonious tree. We then used the R package TreeSearch[174] to calculate the minimum possible length of each craniodental character on any tree (using the MinimumLength function), and its length on the single most parsimonious tree that resulted from the molecular scaffold analysis (using the CharacterLength function); if the latter was greater than the former (indicating some homoplasy relative to the molecular consensus), then that character was removed from the craniodental matrix. This procedure resulted in the removal of 519 characters, leaving 2146 characters, of which 467 were parsimony informative, and 422 were variable but non-parsimony informative. The fossil terminals were then re-added to this homoplasy-filtered matrix, which was analysed using MP in TNT with the same two-stage search strategy used for the full matrix.

MP analysis of the homoplasy-filtered craniodental matrix resulted in three most parsimonious trees (length = 1598 steps). The strict consensus of these (Figure S2B) recovers relationships among extant bats that are fully congruent with the current molecular consensus, including monophyly of Yangochiroptera (bootstrap = 89%) and Yinpterochiroptera (bootstrap = 50%), although only the former is strongly supported. Similarly to MP analysis of the full craniodental matrix (Figure S2A), this analysis places all the Eocene fossil bats, including *Vielasia*, outside the crown clade, but bootstrap support for the crown clade is low (bootstrap <50%). The fossil bats are recovered in a single clade that is moderately strongly supported (bootstrap 73%), rather than as a paraphyletic assemblage as found in the MP analysis of the full craniodental matrix (Figure S2A); within this fossil clade, *Vielasia* and *Cambaya* form a weakly supported (boostrap < 50%) clade that is sister to another weakly supported (bootstrap < 50%) clade comprising the remaining fossil taxa.

Although this analysis similarly supports the hypothesis that *Vielasia* is not a crown clade bat, it is incongruent with previous studies[9,36] (and with our maximum parsimony of the full craniodental dataset [Figure S2A] and our Bayesian dated analysis of our total evidence data set [Figure 2]) in placing all Eocene fossil bats in a clade, with onychonycterids (species of *Onychonycteris*, *Eppsinycteris*, *Ageina* and *Honrovits*) in a nested position; these other analyses instead recover Eocene fossil bats as paraphyletic with respect to the crown clade, and place onychonycterids (including the well-preserved *Onychonycteris*, which shows a range of features that have been generally interpreted as plesiomorphic relative to other known fossil bats) in a basal position.[9] In addition, this kind of homoplasy-filtering approach represents a form of ''maximum compatibility'' analysis, which is a method of phylogenetic analysis that has had a long history of criticism (e.g., Farris and Kluge,[175] Farris,[176] and de Pinna[177175–177]), and characters that are homoplastic within one part of a phylogeny (e.g., within the crown clade) may still be useful for resolving relationships elsewhere in the tree,[178] and so arguably should not simply be discarded. For these reasons, we have used the full, unfiltered craniodental matrix for our total evidence analyses (see below). Nevertheless, we consider the results of this homoplasy-filtered craniodental analysis to provide additional evidence that *Vielasia* is not a crown clade bat.

Templeton tests of alternative topologies

To test whether our full and homoplasy-filtered craniodental matrices are compatible with *Vielasia* being a crown chiropteran, we carried out constrained MP analyses of both matrices with *Vielasia* enforced to fall within the crown-clade. As already noted, MP analysis of the full craniodental dataset placed extant laryngeally-echolocating bats in a single clade to the exclusion of *Pteropus*, which was sister to all other chiropterans (Figure S2A); within the extant echolocating clade, *Myotis* and *Pteronotus* formed one subclade, and *Nycteris*, *Rhinopoma* and *Saccopteryx* the other. For the constrained analyses of the full craniodental dataset, we therefore enforced *Vielasia* to either form a clade with *Myotis* and *Pteronotus* to the exclusion of all other taxa, or a clade with *Nycteris*, *Rhinopoma* and *Saccopteryx* to the exclusion of all other taxa. MP analysis of the homoplasy-filtered craniodental dataset (Figure S2B) recovered monophyly of Yangochiroptera and Yinpterochiroptera, and so for the constrained analyses of this dataset, we enforced *Vielasia* to either form a clade with the extant yangochiropteran taxa (*Saccopteryx*, *Nycteris*, *Myotis*, and *Pteronotus*), or the yinpterochiropteran taxa (*Pteropus* and *Rhinopoma*), to the exclusion of all other taxa. The constrained maximum parsimony analyses used the same search settings in TNT as the unconstrained analyses.

Templeton tests[179] comparing the most parsimonious topologies from the unconstrained and constrained analyses were then implemented in PAUP* 4.0a169,[120] the resultant p-values converted from two-tailed to one-tailed (following Goldman et al.[180]) by dividing by two, and mean p-values were calculated from the MPTs for each constrained analysis. In both cases, a constrained position for *Vielasia* within the crown clade (or, in the case of the full craniodental analysis, within the extant echolocating clade) was rejected, with p-values for the Templeton tests <0.05 (Data S1E). Thus, a position for *Vielasia* within crown Chiroptera is strongly rejected by our full and homoplasy-filtered craniodental matrices.

Total evidence (TE) matrix

Numerous studies support the use of a total evidence (combined morphological and molecular data) approach over morphology-only and molecular scaffold approaches for phylogenetic analyses that combine fossil and extant taxa (e.g., de Queiroz and Gatesy,[181] Manos et al.,[182] Dávalos et al.,[183] and Darlim et al.[184]). We therefore created a total evidence matrix by combining our full craniodental matrix (see above) with molecular data for our six extant bat terminals and three extant non-bat outgroup terminals (*Solenodon*, *Erinaceus*, and *Sorex*) taken from the alignment of O'Leary et al.,[61] which comprises 36860 base pairs of DNA sequence data from 27 nuclear loci, originally from Meredith et al.[2] All our fossil terminals were scored as unknown (?) for the molecular data.

Undated Bayesian analysis of TE matrix

Undated Bayesian analysis of the total evidence analysis was carried out in MrBayes v. 3.2.7a running on JASMIN, the UK's collaborative data analysis environment (https://jasmin.ac.uk[185]). We assigned a single Lewis[186] Mk model to the craniodental characters; given the large proportion of variable but non-parsimony informative characters (see above), we corrected for ascertainment bias by using the Mk*v* variant of the model, which assumes that only variable characters were scored (and so all constant characters were ignored in each analysis). An eight category lognormal distribution was used to model rate heterogeneity between characters.[187] For the DNA sequence data, an optimal partitioning scheme and set of models was identified using PartitionFinder 2.2,[117] with the sequence data initially partitioned by gene and (if protein-coding) codon position. The ''greedy'' algorithm and the Bayesian Information Criterion were used for model selection, with the choice of models restricted to those implemented by MrBayes, and with models that include both a gamma distribution and a proportion of invariant sites not tested[188] (Data S1C).

The undated total evidence analysis comprised two independent runs of four chains with default heating parameters, run for 10 million generations, sampling trees and other parameters every 5000 generations. To reduce the time needed to reach stationarity and convergence between chains, the following uncontroversial clades were enforced as monophyletic: Chiroptera (= all of our extant and fossil bat terminals), Eulipotyphla (= *Solenodon* + *Erinaceus* + *Sorex*), and Laurasiatheria (= all our terminals except *Maelestes*, *Ukhaatherium*, and *Zalambdalestes*). Tracer was used to identify an appropriate burn-in fraction for each analysis, and the post-burnin trees were summarised in MrBayes using 50% majority rule consensus, with Bayesian posterior probabilities as support values.

The undated total evidence analysis (Figure S2C) provides strong support (BPP = 0.95) for monophyly of crown clade bats to the exclusion of all Eocene fossil bats included in the matrix, including *Vielasia*. The topology resembles that of the homoplasy-filtered craniodental matrix (Figure S2B) in placing all Eocene fossil bats in a relatively strongly supported (BPP = 0.86) clade, within which *Vielasia* forms a strongly supported (BPP = 0.97) clade with *Cambaya*, and *Vielasia* + *Cambaya* is sister to the remaining fossil bats, with Onychonycteridae in a nested position. We consider this topology less plausible than that found in the dated total evidence analysis (Figure 2) for reasons already discussed (see above), but it again supports the hypothesis that *Vielasia* is not a crown clade bat.

Dated analysis of TE matrix

Based on simulated data, Mongiardino Koch et al.[54] found that including temporal information in Bayesian analyses using a fossilised birth-death (FBD) model led to increased phylogenetic accuracy relative to equivalent undated approaches. For these reasons, our preferred phylogenetic analysis is a dated Bayesian analysis of the total evidence matrix, and we focus on this here.

For this analysis, we used the same substitution models for the morphological and molecular partitions as in the undated analysis (see above). We implemented the Fossilised Birth Death model with a combination of tip and node calibrations, following the general approach of Kealy and Beck,[189] Beck and Taglioretti,[190] and Beck et al.[191] An Independent Gamma Rates (IGR) clock model[192] was specified, with two separate clock models: one for the morphological characters, and one for the combined DNA sequence data. The prior on the clock rate was estimated using the custom R script of Gunnell et al.[193] A vague prior – uniform (0.001,200) – was specified for the variance of the IGR clock model, following Matzke and Wright.[194] Diversity sampling was assumed, with a sample probability of 0.00418, based on the inclusion of six extant bat species out of a currently recognised total of 1437.[195] Because our taxon set does not include any fossil terminals younger than 47.4 Ma, we specified a shift in sampling at this time.[196] Priors on speciation, extinction and fossilisation were left as the MrBayes defaults.

Extant terminals were assigned an age of 0 Ma, whilst fossil terminals were assigned a uniform age prior reflecting the stratigraphic uncertainty in their ages, following the recommendations of Püschel et al.[197] (Data S1D). We enforced monophyly of Chiroptera, Eulipotyphla and Laurasiatheria (as in the undated analyses) and specified internal node calibrations for these three clades based on current fossil evidence, as follows. Chiroptera was assigned a minimum bound of 52.201 Ma (very slightly older than the minimum age of the oldest bat terminal in our matrix, *Eppsinycteris anglica*; Data S1D) and a maximum bound of 66 Ma. Eulipotyphla was assigned a minimum bound of 62.5 Ma (the minimum age of Torrejonian To2, see Beck and Lee [198] and electronic suppl. mat. of Flynn et al.[199]) and a maximum bound of 83.6 Ma (the maximum age of the Campanian).[200] Laurasiatheria was assigned a minimum bound of 65.689 Ma (very slightly older than the minimum age of the oldest laurasiatherian terminal in our matrix, *Protungulatum donnae*) and a maximum bound of 113 Ma (the Aptian-Albian boundary[201]), which corresponds to the age of the oldest known eutherian with only four premolars (*Sasayamamylos kawaii*[201]), on the assumption that the origin of Placentalia (the last common ancestor of which is reconstructed as having four premolars[61]), and hence Laurasiatheria, is highly unlikely to predate this. All three internal node calibrations were specified as offset exponential distributions,[202] such that there was a 5% prior probability for the calibrated node being older than the maximum bound. Preliminary analyses with the age of the root node unconstrained resulted in implausibly ancient posterior root ages, and so we used a truncated normal prior on the root age with a mean age (77.95 Ma) that was slightly older than the mean age (77.85 Ma) of the oldest terminals in our matrix (the outgroups *Maelestes gobiensis*, *Ukhaatherium nessovi*, and *Zalambdalestes lechei*), and a standard deviation of 1.0 Ma, following Sallam and Seiffert.[203]

The dated total evidence analysis comprised two independent runs of four chains, with default heating parameters, run for 40 million generations, and sampling trees and other parameters every 5000 generations. Stationarity and convergence between runs were determined using Tracer and used to identify an appropriate burn-in period; all post-burn-in trees were then combined using 50% majority rule consensus, with Bayesian posterior probabilities as support values.

In the dated total evidence analysis (Figure 2), monophyly of crown-clade bats to the exclusion of all our fossil Eocene bats is strongly supported, with a Bayesian posterior probability (BPP) of 1.00. Relationships within the crown-clade are fully congruent with previous molecular studies, with very strong support for monophyly of Yangochiroptera (BPP = 1.00) and Yinpterochiroptera (BPP = 1.00). *Vielasia sigei* was recovered as the sister-taxon of crown-clade bats in this analysis, although with only moderate support (BPP = 0.63); the presence of a non-zero branch length leading to *V. sigei* indicated that it is not plausibly ancestral to the crown clade. The sister-taxon to *Vielasia* + the crown-bat clade was *Cambaya*, and monophyly of *Cambaya* + *Vielasia* + crown clade bats received strong support (BPP = 0.95).

This analysis also recovered a fairly strongly supported (BPP = 0.85) clade comprised of onychonycterids (species of *Onychonycteris*, *Eppsinycteris*, *Ageina* and *Honrovits*) and another containing the other four extinct Early Eocene bat families in our sample (icaronycterids + archaeonycterids + hassianycterids + palaeochiropterygids), although support for this latter clade is very weak (BPP = 0.51). Onychonycteridae was the first family to diverge, which is congruent with previous suggestions.[9,28,31,67] Within Onychonycteridae, relationships were fully resolved and consistent with previous studies.[28,31] Archaeonycterids (*Archaeonycteris* and *Protonycteris* spp.) form a poorly supported (BPP = 0.51) clade, with the exception of *A. trigonodon* which is moderately strongly supported as sister to icaronycterids + hassianycterids + palaeochiropterygids (BPP = 0.82). Within this latter group, the relationship of *Icaronycteris* spp. to each other and to a clade comprising the hassianycterids + palaeochiropterygids were unresolved. The possible paraphyly of *Archaeonycteris* and *Icaronycteris* has been suggested previously.[28,31]

Maximum parsimony optimisation of the craniodental matrix on the dated total evidence phylogeny (our preferred topology; Figure 2) in PAUP 4.0a[120] results in 49 characters being identified as unambiguous (i.e., under both accelerated and delayed transformation) synapomorphies for crown Chiroptera to the exclusion of *Vielasia*; a full list of synapomorphies for all nodes in the dated total evidence phylogeny is given in Data S2.

Bayes factor tests of alternative topologies

To test whether our total evidence matrix is compatible with *Vielasia* being a crown chiropteran, we carried out constrained versions of the undated and dated Bayesian analyses with *Vielasia* enforced to fall within the crown-clade; we then compared the fit of these constrained analyses to the unconstrained analyses using Bayes factors.[204–206] Both undated (Figure S2C) and dated (Figure 2) analysis of the total evidence dataset recovered monophyly of Yangochiroptera and Yinpterochiroptera, and so for the constrained versions of these analyses, we enforced *Vielasia* to either form a clade with the extant yangochiropteran taxa in the matrix (*Saccopteryx*, *Nycteris*, *Myotis*, and *Pteronotus*), or the yinpterochiropteran taxa (*Pteropus* and *Rhinopoma*), to the exclusion of all other taxa. We calculated harmonic means for the unconstrained and constrained topologies using stepping stone analysis[204] calculated using 10 million generations, with otherwise default settings. Bayes factors were then calculated as 2x the difference in log likelihood between the constrained and unconstrained topologies.[205–207] For all constrained topologies, Bayes factors (B10) for the stepping stone analyses were >150 (Data S1E), representing very strong evidence[205–207] against a position for *Vielasia* within crown Chiroptera, and in favour of its unconstrained position as a stem chiropteran.

Summary of phylogenetic analyses

In summary, the results of the phylogenetic analyses presented here collectively provide very strong evidence that *Vielasia* is not a crown clade bat (see Figures 2 and S2A–S2C; Data S1E). In turn, they support the hypothesis that the advanced echolocation abilities evidently present in *Vielasia* based on its cranial anatomy originated outside the clade that encompasses all modern laryngeally-echolocating bats. However, our preferred topology (Figure 2), from the dated total evidence analysis, places *Vielasia* sister to the crown-clade, and so suggests that the echolocation abilities of *Vielasia* may be homologous with crown bats, and thus that the laryngeal echolocation characteristic of modern non-pteropodid bats evolved once, prior to the diversification of the crown clade.

LINEAR AND GEOMETRIC MORPHOMETRIC ANALYSES

Phylogenetic framework

In order to investigate the impact of phylogenetic non-independence on our morphometric analyses, we used phylogenetic comparative methods and three different dated phylogenies of bats: (1) the total evidence tip-dating phylogeny produced as part of this study (e.g., Figure 2), (2) the molecular node-dating phylogeny of Shi and Rabosky,[83] and (3) the molecular node-dating phylogeny of Amador et al.[84] The total evidence tip-dating phylogeny obtained here only allows for taking into account variation in branch lengths, which are proportional to time: *Vielasia sigei*, as a tip, and the node where *Vielasia* diverges from the crown bat clade, are reconstructed with a range of ages based on the post-burnin trees output by MrBayes. The phylogenies of Shi and Rabosky[83] and of Amador et al.[84] allow for taking into account variation in both topology and branch lengths (= divergence times). Combining these three different phylogenetic datasets, we could therefore take into account variation in both topology and estimated divergence times (the only constant point being the stem position of *Vielasia sigei*), and this served to test the robustness of our statistical results.

Vielasia is present in our total evidence tip-dating phylogeny, as the sister taxon of crown Chiroptera, but needed to be added in this position to the Shi and Rabosky[83] and Amador et al.[84] molecular phylogenies *a posteriori*. This is only possible if the age of the *Vielasia* + crown Chiroptera node (as estimated in our total evidence tip-dating phylogeny) predates the age of crown Chiroptera in the two molecular phylogenies. We sampled 1001 post-burnin trees output from our total evidence tip-dating analysis and filtered them to retain only those in which the age of *Vielasia* + crown Chiroptera predates the age of crown Chiroptera estimated by Shi and Rabosky[83] and Amador et al.[84]; to do this, we used the packages treeio,[208] ape,[209] phytools,[210] and ULT,[211] which resulted in 104 trees for the Shi and Rabosky[83] phylogenetic dataset, and two trees for the Amador et al. dataset.[84]

However, this approach resulted in only a small amount of variation in branch lengths being retained (particularly in the case of Amador et al.,[84] where only two trees can be used), and, perhaps more importantly, it resulted in a potentially unrealistically short branch between *Vielasia* + crown Chiroptera and crown Chiroptera, which would reduce the probability that the similarities between *Vielasia* and crown chiropterans are convergent: the branch separating *Vielasia* + crown Chiroptera from crown Chiroptera is so short that very little evolutionary change will be estimated to have occurred along it, and so similarities between *Vielasia* and crown chiropterans will be likely to be interpreted as due to common ancestry. Therefore, we also rescaled the Shi and Rabosky[83] and Amador et al.[84] molecular phylogenies so that the age of crown Chiroptera matched the age of this node in the 1001 post-burnin trees obtained from our total evidence tip-dating analysis. This allows for a greater range of variation in branch lengths to be taken into account. To do this, we used the R packages scales[212] and geiger[213] to linearly rescale the ages of the Shi and Rabosky[83] and Amador et al.[84] molecular phylogenies so that the age of crown Chiroptera matched the age of this node in each of the 1001 post-burnin trees from our total evidence tip-dating analysis, with the ages of more nested nodes adjusted by the same (linear) scaling factor.

We note here that the phylogeny of Amador et al.[84] includes a node that is younger than one of its two descendants; this is an artefact produced by the software used by the authors of that article (N.P. Giannini, pers. comm.). To avoid problems with downstream analyses, we changed the age of this node so that the length of the branch leading to its ‘‘older’’ descendant became half the minimal length of all other internal branches (i.e., half of 0.0648 Ma); this represents a compromise between keeping a negative value and replacing it with an arbitrary positive value (i.e., the branch length is now positive instead of negative, but still half the length or less than that of any other internal branch). In addition, we note that most of the extant tips in the phylogeny of Amador et al.[84] do not have an exact age of 0 Ma (out of 812 taxa, only four have an age of 0 Ma, 30 have an age of 0.24 Ma, and 778 have an age of 0.35 Ma). However, we did not correct these very minor anomalies, as they would have a minimal impact on our downstream analyses.

As a result of these procedures, we were left with 1105 trees corresponding to the Shi and Rabosky[83] phylogeny – 104 with original ages that are already compatible with the post-burnin trees from our total evidence tip-dating analysis, and 1001 with ages rescaled to match the post-burnin trees -, and 1003 trees corresponding to the Amador et al.[84] phylogeny – two with original ages that are already compatible with the post-burnin trees, and 1001 with ages rescaled to match the post-burnin trees. In both cases, two of the rescaled trees had a null branch length between the *Vielasia* + crown Chiroptera node and the crown Chiroptera node; these two trees were removed, leaving 1103 trees corresponding to the Shi and Rabosky[83] phylogeny, and 1001 corresponding to the Amador et al. phylogeny.[84]

Bony labyrinth morphometric analysis

Using several morphometric features of the bony labyrinth, Davies et al.[19,63] were able to discriminate between bats and non-bat placental mammals, as well as between echolocating and non-echolocating bats. Of these features, we focused on two we were able to measure on the bony labyrinth of *Vielasia sigei* and that may give an indication of the echolocating ability of this species. The first is the length of the cochlear basilar membrane, the allometric relationship of which with body mass led Davies et al.[19] to note that, in comparison to other placentals, echolocating bats have a longer cochlear basilar membrane than expected given their body mass. Secondly, Davies et al.[63] calculated the size of the semicircular canals (estimated as the average of a canal's height and width) and the size of the cochlea (a one dimensional value calculated following Spoor et al.[64] as the average of the diameters of the first and second cochlear turn and of the "slant height" of the cochlea) and found a difference between echolocating bats and other mammals (including non-echolocating bats) when plotting semicircular canal size against cochlea size (echolocating bats having larger cochlea/smaller canals).

For both basilar membrane length vs body mass and semicircular canal size vs cochlear size, we tested whether we could discriminate between bats and non-bat placentals, and between different echolocation types in bats (non-laryngeal echolocating, oral-emitting, and nasal-emitting). We included cetaceans in both datasets because they represent a mammalian clade that includes species that have evolved to hear very high frequencies (odontocetes), similarly to bats, but also species that have evolved to hear very low frequencies (mysticetes). These two additional classes may allow us to identify a functional signal in the traits tested and therefore increase the validity of our inferences. After controlling for potential effects of these ecological categories on the relationships we tested, our final goal was to include *Vielasia* and test whether it could be confidently assigned to a particular class (i.e., non-LE bats, LE-bats, HF-hearing cetaceans, LF-hearing cetaceans, or other placental mammals).

For the cochlear basilar membrane length vs body mass relationship, we simply added measurements for *Vielasia* to the dataset of Davies et al. (see table S2),[19] with therefore 82 species included (44 extant bats, 37 extant mammals, and *Vielasia sigei*; Data S1G). The dataset of Davies et al. (see table S1)[63] included measurements of cochlear and semicircular canal sizes for chiropterans only; thus, we had to obtain the non-chiropteran data they used directly from various references,[64,92,112] to which we added additional measurements for cetaceans.[110,111] The resulting dataset therefore includes 124 species, with 52 extant bats, 71 extant mammals, and *Vielasia sigei* (Data S1M). The phylogeny used by Davies et al.[63] for their comparative analyses does not include cetaceans, and so we instead used the dated mammalian phylogeny of Álvarez-Carretero et al.[6] as the starting tree for our own analyses. However, we replaced the bat clade in the Álvarez-Carretero et al.[6] phylogeny with the bat phylogenies derived from Shi and Rabosky,[83] Amador et al.,[84] and the current study (see "phylogenetic framework" above). This requires that the age of *Vielasia* + crown Chiroptera is younger than that of the node uniting Chiroptera with its sister taxon, which in the Álvarez-Carretero et al.[6] phylogeny is Artiodactyla + Perissodactyla + Carnivora + Pholidota. This was the case for 74 of the 104 trees derived from Shi and Rabosky[83] without rescaling, but was not the case for either of the two trees derived from Amador et al.[84] without rescaling (see "phylogenetic framework" above for details); for the rescaled phylogenies, this was the case for 971 of the 1001 trees derived from Shi and Rabosky,[83] and for 974 of the 1001 trees derived from Amador et al.[84] For each dataset (basilar membrane length vs body mass; semicircular canal size vs cochlear size), we then pruned the relevant phylogenies to retain only those species for which we had measurements.

Basilar membrane length vs body mass – Regarding the allometric relationship of basilar membrane length to body mass, we first simply plotted all points, distinguishing them according to the following groups: high-frequency hearing cetaceans, low-frequency hearing cetaceans, non-laryngeally echolocating bats (pteropodids), laryngeally echolocatng bats (nasal- and oral-emitters), and other placentals.

We then performed phylogenetic generalized least squares (PGLS) regressions of (natural logarithm of) basilar membrane length against body mass, repeating the analysis for all phylogenies we created. To do so, we used functions and methodology from the packages phylolm[214] and sensiPhy[215] to implement PGLS regression of log basilar membrane length against log body mass, taking into account phylogenies with variation in their relationships (within Chiroptera) and in their branch lengths. The function phylolm from the eponym package[214] allows for performing PGLS regressions with several different possible evolutionary models (Brownian motion, Brownian motion with trend, Ornstein-Uhlenbeck with a fixed and estimated root value or with a stationary ancestral distribution, Pagel's lambda, kappa, and delta, and the early burst model). The function tree_phylm from the sensiPhy package enables the PGLS regression to be repeated across multiple phylogenies, and outputs tables to compare averaged parameters between the tested models. We wrote a function named tree_phylm_full_results[123] which is a slightly modified version of the tree_phylm function (of the sensiPhy package). This custom function can be easily further modified to output more information than given by the standard tree_phylm function, such as regression residuals, fitted values etc. This custom function returns two important elements that are also returned by the standard tree_phylm function, namely: the estimated parameters for each PGLS regression (the $sensi.estimates element) and the averages of the parameters for each model (the $all.stats element). In tree_phylm_full_results however, the $sensi.estimates element as well as other outputs from the regressions can be returned for all tested models, not just for the best-fitting model, the choice being up to the user (by turning the option output.all.models to TRUE or FALSE).

Finally, we tested whether there were significant differences in the PGLS regression parameters between selected comparisons (bat versus non-bat placentals, laryngeally echolocating bats versus other placentals, high-frequency hearing mammals versus others, high- and low-frequency hearing mammals versus others). To perform these comparisons, an additional wrapper on the tree_phylm function, compare.tree_phylm[123] was written. This function takes the same input variables as the tree_phylm_full_results function, plus information regarding potential subsetting of the dataset. If a subset is specified, the dataset is divided in two groups (i.e., both the phylogenies and the morphometric data), PGLS is performed for both (using tree_phylm_full_results function), then the compare.tree_phylm function provides the results from a t-test contrasting average slopes and intercepts for the PGLS with best-fitting evolutionary models for each group, and finally it outputs average regression line parameters to be able to simply add them to an existing biplot.

Overall, there are few differences between our comparisons (Data S1H), that aim to compare selected subsets of our dataset (LE bats, all bats, LE bats plus HF-hearing cetaceans, LE bats plus both HF-hearing and LF-hearing cetaceans) both to the remaining species (i.e., non LE bat placentals, non-bat placentals etc.) and to the whole dataset. There is no significant difference in regression slopes ($p > 0.4$ for every comparison), and only some significant differences in regression intercepts. These differences generally contrast echolocating mammals and other species: LE bats seem to differ from other placentals, although this relationship is not significant ($p = 0.06$), bats are significantly different from non-bat placentals ($p = 0.02$), and placentals with extreme hearing abilities (i.e., HF-hearing and LF-hearing mammals) in general differ markedly from other placentals ($p = 0.009$).

No selected subset differs significantly from the overall placental trend (i.e., the regression for the whole placental dataset), and so we only added the placental regression line (i.e., Pagel's delta with an average value of 2.47) to the primary drawn biplot in the main text (Figure 3B); other configurations can be found in Figure S3A. Regarding the position of *Vielasia*, it is located in the middle of the morphospace comprising laryngeally echolocating bats, which is far from that of non-echolocating bats. This suggests echolocating abilities in *Vielasia*, although echolocating bats do not differ enough from other mammals to demonstrate this statistically. Morphospaces of both echolocation call types (i.e., emission through the nose or the mouth) overlap considerably, and *Vielasia* falls within this area of overlap; thus, this particular analysis is unable to determine the type of echolocation emission of *Vielasia*.

For our analysis of the relationship between semicircular canal size vs cochlear size, we first performed a simple, graphical comparison of semicircular canal size (radius of their curvature, R) and cochlea size (as defined by Spoor et al.,[64] but see also Davies et al.[63]) for bat species as done by Davies et al.[63] We however diverged from the original representation of Davies et al. (see figure 4)[63] by instead performing boxplots (to better represent whole bat trend) adding values ranges (for LE yangochiropterans, LE yinpterochiropterans, and non-LE yinpterochiropterans) to compare with the values of *Vielasia sigei* (Figure 3C). Values were not corrected for relative size or phylogeny.

Second, our goal was to replicate Davies et al.'s[63] regressions of each semicircular canal size against cochlea size (e.g., see figure 5 in Davies et al.[63]). Instead of analyzing each regression separately, we aimed to encompass all three regressions and provide a multivariate depiction of the relationship between semicircular canal size and cochlea size. We could not directly perform multivariate analyses, as the sensiPhy package[215] cannot deal with multivariate data, and as there is currently no satisfactory method for multivariate PGLS - there are some methods for highly correlated variables that are landmark coordinates, but as yet not for putatively independent ones (e.g., Adams[216] and Clavel and Morlon[217]). Therefore, we performed a PGLS regression for each semicircular canal separately (i.e., natural logarithms of semicircular canal radius against cochlea size), and PGLS residuals were then used as the basis for further interpretation. It should be noted that these residuals are not phylogeny-corrected residuals; they are simply more appropriate to use than residuals derived from OLS regressions.[218] Moreover, subsequent tests on regression residuals are not recommended since they can give erroneous results.[219,220] Hence, we took an appropriately cautious approach, applying descriptive treatments: we performed discriminant analyses taking into account phylogeny ('phylogenetic flexible discriminant analysis' or pFDA[122]) or not (traditional linear discriminant analysis, LDA, using the package MASS[221]) to examine first whether the link between canal and cochlea size proposed by Davies et al.[63] depends on phylogeny (see Data S1I), and second in which group *Vielasia sigei* falls in each case (see Data S1J). To determine whether *Vielasia* could be assigned to a particular hearing ability group (same groups as the basilar membrane length vs body mass relationship), we specified the groups as the discriminant factor, *Vielasia* as the "test" group, and all other extant species as the "training" set of the discriminant analysis (as their membership of a particular group is already known). We repeated these analyses for all the phylogenies we created, and we reported average coordinates, reflecting the coordinate variation for each species, for each analysis (Figures 3D and S3B).

Numerous R packages allow for performing PGLS regression; here, we chose to use the pgls function of the package caper.[222] The pFDA function (to perform the eponym analysis), as written by Motani and Schmitz,[122] takes phylogeny into consideration by modifying the inputted phylogeny by transforming its branch lengths (and therefore its variance-covariance matrix) to account for phylogenetic autocorrelation using Pagel's lambda. Motani and Schmitz[122] recommend estimating the lambda parameter from the data, and to provide this estimate of lambda to the pFDA function. However, as well as values of Pagel's lambda, the pgls function of the package caper estimates (using maximum likelihood) values for two other models: Pagel's kappa and delta (see for instance the vignette of the package caper[222]). By default, Pagel's kappa and delta are not taken into account in the pFDA function. However, since all three models are direct transformations of the tree, we slightly modified the pFDA function written by Motani and Schmitz[122] to also take these two parameters into account, applying the exact same transformation to the tree that the function pgls does.

Doing three regressions (i.e., each semicircular canal size vs cochlear size), the three values for each Pagel's parameter are likely to differ, whereas the pFDA function can only handle a single value for each (i.e., a single way to transform the tree). A unique value for each parameter has therefore to be found that can be applied to all three regressions; we wrote and used the function conv.pgls to deal with this.[123] This function runs PGLS regressions of each variable, narrowing progressively the interval in which the values are estimated, which results in parameter estimates that converge asymptotically. First, the conv.pgls function performs PGLS regressions with the default bounds for each parameter; each of these first regressions yield 95% confidence intervals for each parameter. Then, the function retains the shared interval of all 95% intervals for each parameter, and repeats PGLS regressions, narrowing progressively this interval using a user-defined thinning parameter (with a default value set to 10%) that is not necessarily symmetrical: the narrowing of this interval of a (provided) % value is proportional to the position of the parameter value (i.e., the closest to a bound is the parameter value, the less the interval is narrowed on that bound, and the more it is narrowed on the other bound, the sum of this narrowing being equal to the provided % value). At the end, the function outputs the "optimal" common value of the three parameters lambda, kappa, and delta, together with two tables comparing 1) AIC values for regressions with locally (i.e., for each regression) or globally (i.e., for all regressions) optimal parameters, and comparing 2) the parameters value and 95% confidence interval of each PGLS regression with the "globally optimal" parameter values. The function can also output the residuals for each PGLS with the "globally optimal" parameter values. We then wrote two functions to repeatedly perform pFDA and LDA (pfda_LSchmitz and rep_lda respectively[123]) using the "globally optimal" Pagel's parameter values (and the residuals arising from PGLS regressions using them) for all phylogenetic trees considered. These functions output, for each iteration (= phylogeny), a confusion matrix (a matrix of true and predicted attributions for the training dataset) and various results regarding the training and test datasets (i.e., predicted class, probability for each class, discriminant axes scores).

To help visualize the variation between all calculated pFDAs and LDAs (i.e., depending on phylogenies) for each species' score on discriminant axes, we also plotted the morphospaces of each species' points, using both all points of each species ('full' morphospaces) and the 95% points closest to the 'full' morphospace centroid ('95%' morphospaces; i.e., points below the 95% quantile of Euclidean distance to the full morphospace centroid, the latter being calculated using the sf package[223]). This procedure has been wrapped in a custom function named plots.variation,[123] taking into account data points (and morphospaces if already computed and saved), average positions, analyses names, axes information (number, percentage of contribution), ecological groups (and colors) if applicable, and options to return the computed morphospaces and to output the produced figures. These plots of 'full' and '95%' morphospaces (Figure S3B) allow for more detailed comparison of the position of *Vielasia* relative to the morphospaces of the other taxa in these plots, and to visualize the full variation in discriminant axes scores.

In both pFDA and LDA, the first discriminant axis accounts for ~75% of the between-group variance. There is also a clear link between phylogeny and hearing ability type across placentals. Though there are errors in the classification (Data S1I), there is a hierarchy along the first discriminant axis in the LDA (i.e., when phylogeny is not taken into account), with high-frequency hearing non-bat mammals (odontocetes), then echolocating bats plus low-frequency hearing non-bat mammals (mysticetes), and then non-echolocating bats and all other placentals (Figures 3D and S3B). Most of the classification errors are swaps between overlapping groups. In the LDA, *Vielasia* is classified as an echolocating bat (Data S1J; Figures 3D and S3B), but nasal-emitting and oral-emitting bats are not distinguishable along the first linear discriminant axis. Taking into account phylogeny by means of pFDA, there seems to be no ecological signal at all: all taxa are predicted as "non-echolocating and non-bat placentals" (Data S1J), and all categories overlap (Figure S3B). Therefore, *Vielasia* is also retrieved as a "non-echolocating and non-bat mammal" (Data S1J) and falls roughly in the middle of the plot of the two first discriminant axes (Figure S3B). Variation in the phylogeny does not alter these observations: there is more variation in species position in the pFDA than in the LDA (Figure S3B), but it remains slight.

In summary, the echolocation call types/hearing abilities may depend on phylogeny, phylogenetic variation not much altering global trend; we hence preferred to provide average species' position and groupings of the LDA in the main text (Figure 3D), detailed graphs for both analyses being available in the Figure S3B. According to these results, *Vielasia* would presumably have been able to echolocate because it is a bat, but non-LE bats still fall within the morphospace of "other" placentals; in bats, phylogeny does not exactly "predict" echolocation call type, and *Vielasia*'s position in the LDA may be independent from phylogeny as well.

3D geometric morphometric analysis

We included the composite 3D cranial and mandibular models of *Vielasia sigei* in the 3D geometric morphometric dataset of Arbour et al.,[65] ESM3 capturing shape of bat crania (with 36 landmarks and 5 curves represented by equidistant semi-landmarks) and mandibles (with 20 landmarks and 4 curves). Using the same protocol, we collected these data from *Vielasia sigei* with Landmark 3.6[114] (Data S1N and S1O). This allowed us to compare *Vielasia* with 202 extant bat species for the cranium and 191 species for the mandible, using the dietary and echolocation emission categories assembled by Arbour et al.[65] (Data S1P). Processing of the cranium and mandible landmark data (i.e., inputting the data, flipping the data when the left or right landmark was missing, estimating missing data, performing the generalized Procrustes alignment, averaging Procrustes coordinates for each species, and averaging paired landmarks) was performed in R 4.1.1,[121] following the approach of Arbour et al.,[65] and was implemented as a custom R function (Arbour_et_al_treatment; available at Maugoust et al.[123]); this function uses functions from the packages geomorph[224,225] and LOST.[226]

We then performed phylogenetic Principal Component Analyses (pPCA) on these aligned datasets using the package phytools. In order to examine variation in pPCA results implied by phylogenetic variation (in terms of branch lengths), pPCAs were performed for all 1103 trees corresponding to the Shi and Rabosky[83] phylogeny (see "phylogenetic framework" above), and so there were a total of 1103 pPCAs for the cranial and the mandibular datasets. To reproduce Arbour et al.'s[65] approach as closely as possible (and so ensure meaningful comparison between our results and theirs), we did not use the set of phylogenies corresponding to the later phylogeny of Amador et al.,[84] as it was not used by Arbour et al.[65]

Parallelisation of the pPCAs computation was done using the packages foreach[227] and doParallel.[228] A problem of repeated pPCAs with slightly varying inputs we encountered is that the outputted principal components can be inverted in their sign depending on the inputs; a custom function (align_rep_ppca) was therefore written to resolve this issue (see comments within this function for technical details[123]).

After this procedure, average pPCA coordinates were calculated for each species on each phylogenetic Principal Component (pPC) axis over all 1103 iterations. As done by Arbour et al.,[65] the proportion of variance explained by each pPC axis was calculated using the procD.lm function of the geomorph package; here this was done for each iteration and then averaged. We then plotted the average coordinates of the two first axes of the pPCAs for cranial and mandibular landmarks (Figure 4).

We also plotted the variation in species' position for all pPCA axes (axes 1-3 for the cranium and 1-4 for the mandible) with 'full' and '95%' morphospaces (see previous section) together with average coordinates (Figure S5). Regarding the cranium (Figure S5A), there is relatively little spatial variation within the 'full' and '95%' morphospaces for each species, with the most variation on the second and third pPC axes. The most significant point is that, on a plot of pPC1 and pPC2 (upper row of Figure S5A), *Vielasia* plots well outside the morphospace of non-echolocating bats, and within the morphospace of oral-emitting echolocating bats, with a clear offset between *Vielasia* and non-echolocating bats on both axes. Regarding the mandible (Figure S5B), the morphopace for each species is once again quite small. In plots of pPC1 and pPC2 (upper row of Figure S5B), most notable is the fact that the morphospace of carnivorous bats overlaps those of nectarivorous and omnivorous bats. In plots of pPC3 and pPC4, each species has a slightly larger morphospace, especially for sanguivorous bats. However, *Vielasia*'s position within dietary morphospace remains similar: it is near the middle of each pPC axis, corresponding to the overlapping morphospaces of carnivorous, frugivorous, and insectivorous bats on pPC1 and pPC2, and at the edge of the insectivorous morphospace in pPC3 and pPC4.

Underlying methodological implications

The goal of our set of morphometric analyses described above was, beyond their original purpose, to test how the results were affected when phylogenetic uncertainty (in terms of phylogenetic relationships and of branch lengths) was taken into account. We first found that, after repeating PCAs (arising from geometric morphometrics) and DAs (of regression residuals) over all the phylogenies we considered, exhaustive graphical results (i.e., showing the whole morphospace of each species) do not differ from simpler ones (i.e., showing only the average values of each species coordinates); this justifies our use of the simpler graphs in the main text (Figures 3B, 3D, and 4). Secondly, again using information from phylogenetic variation, we found little difference between echolocating and non-echolocating placental mammals regarding the allometry of cochlear basilar membrane length (Figure S3A; Data S1H). Alternative allometries of cochlear basilar membrane length (Figure S3A; Data S1H) show that the distinction between laryngeally echolocating bats and other placental mammals found by Davies et al.[19] may be less robust than first thought, but there would still be an offset of the allometric relationship between placentals with extreme hearing abilities and the other species. In all cases, *Vielasia* lies almost on the regression line of the group of interest. Finally, phylogeny is likely to play an important role in ecological discrimination in the relationship between semicircular canal size and cochlear size (Figure S3B; Data S1I and S1J), and should be considered when inferring the ecology of extinct species.

QUANTIFICATION AND STATISTICAL ANALYSIS

The statistical treatment of morphometric data was performed using R 4.1.1[121] and PAST 4.05[119] (see key resources table). It can be re-performed using the source data (also available in Data S1G, S1K, S1M–S1P), with the R script and the entire results of its execution (a RData file) being available at.[123] The R script contains original R functions written for our analyses (as detailed above) and existing R functions (with minor modification) to perform phylogenetic flexible discriminant analysis (pFDA[122]; retrieved from the Github page of Lars Schmitz). The phylogenetic analyses were carried out in TNT 1.5[118] (maximum parsimony analyses of the morphological matrices) and MrBayes 3.2.7a[77] (undated and dated Bayesian analysis of the total evidence matrix), with Templeton tests of alternative topologies and mapping of synapomorphies in PAUP* 4.0a169[120]; the morphological and total evidence matrices as TNT-formatted and MrBayes-formatted files respectively, and the trees output by analyses of these matrices, are available at Maugoust et al.[123] DOIs are listed in the key resources table.

Current Biology, Volume *33*

Supplemental Information

A 50-million-year-old, three-dimensionally preserved bat skull supports an early origin for modern echolocation

Suzanne J. Hand, Jacob Maugoust, Robin M.D. Beck, and Maeva J. Orliac

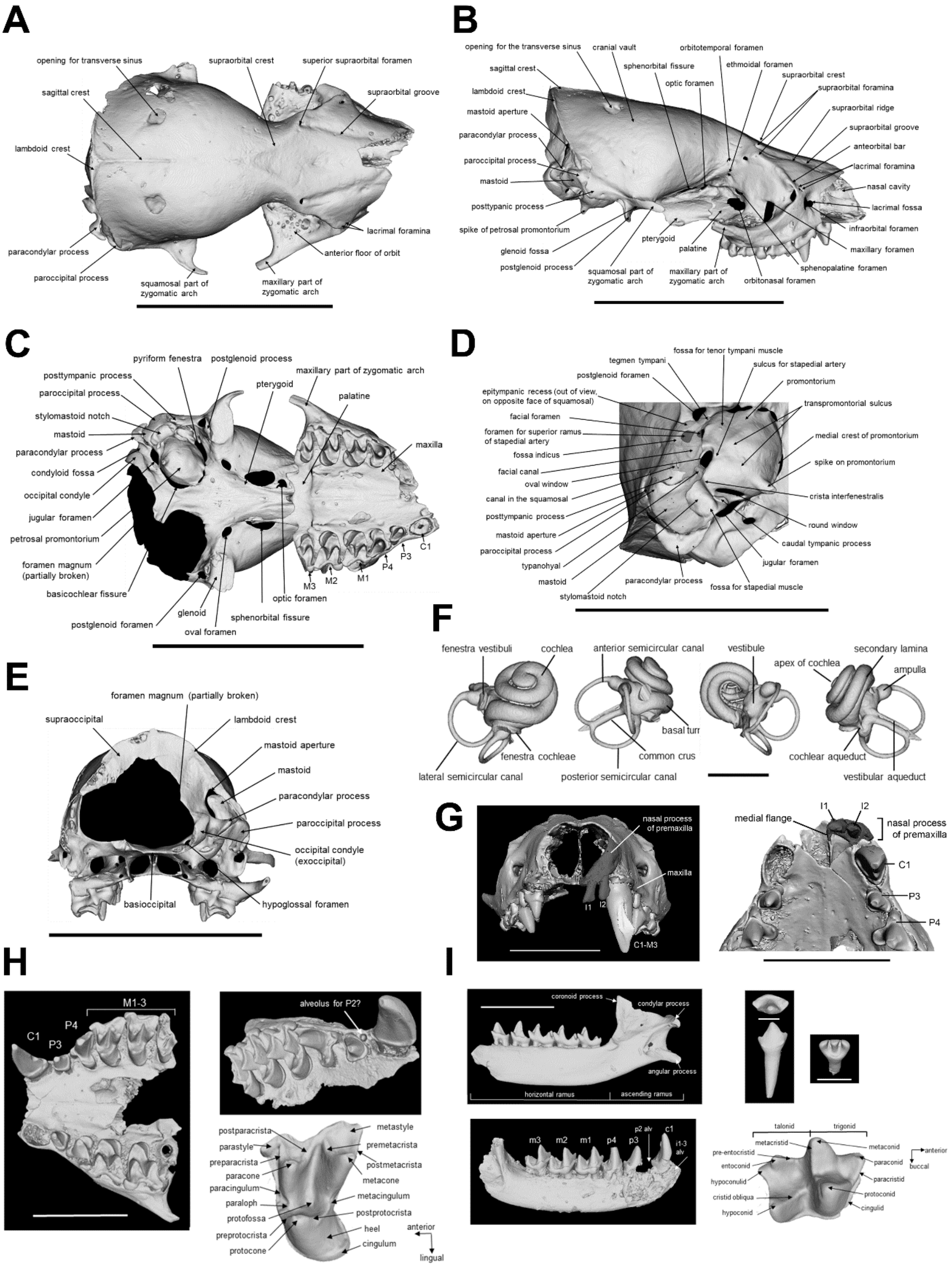

Figure S1. **Cranial, mandibular and dental terminology used in description and discussion of *Vielasia sigei*. Related to Figure 1 and STAR Methods**. (**A-E**) UM-VIE-250, holotype, dorsal, lateral, ventral, posterior and petrosal views, scale bars 10 mm. (**F**) Bony labyrinth endocast (UM-VIE 250, holotype), left to right, ventral, lateral, dorsal, and medial views, scale bar 2 mm. (**G**) 3D model compiled from UM-VIE-251 paratype rostrum and UM-VIE-668 premaxilla with upper incisors: left, anterior view; right, ventral view; scale bars 5 mm, dental abbreviations as in H-I. (**H-I**) Dentition, abbreviations: C/c, upper or lower canine; P/p upper or lower premolar; M/m, upper or lower molar. (**H**) Upper dentition: UM-VIE-251, paratype, rostrum, occlusal view, scale bar 5 mm; UM-VIE-252, paratype, maxilla, oblique view; molar terminology, right M1 in UM-VIE-252. (**I**) Lower dentition: UM-VIE-255, paratype, dentary, lingual view, scale bar 5 mm; UM-VIE-254, paratype, dentary, buccal view, scale bar 5 mm; UM-VIE-614, paratype, p2, occlusal and buccal views, scale bar 0.5 mm; UM-VIE-605, lower incisor, oblique occlusal view, scale bar 0.5 mm; molar terminology, right m1 in UM-VIE-254.

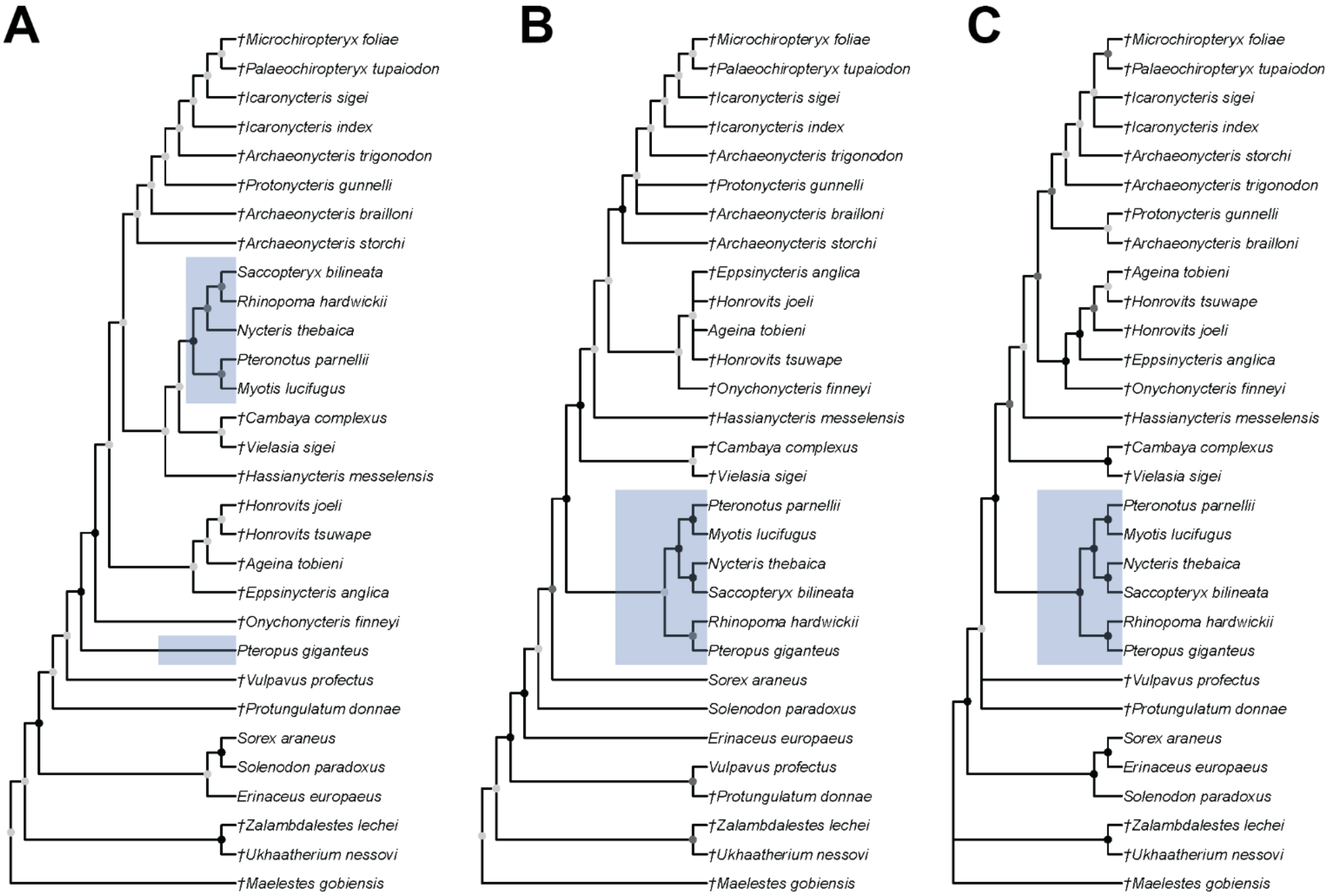

Figure S2. Supplementary phylogenetic analyses (see STAR Methods for full details). Related to Figure 2, STAR Methods, Data S1B-E, and Data S2. (**A**) Maximum parsimony analysis of full craniodental character dataset; strict consensus of 2 MPTs (tree length 3165 steps). (**B**) Maximum parsimony analysis of homoplasy−filtered craniodental character dataset; strict consensus of 3 MPTs (tree length 1598 steps). (**C**) Undated Bayesian analysis of total evidence dataset; 50% majority rule consensus of post-burnin trees. Extant bats are indicated with light blue boxes. Colored dots at nodes indicate support as follows: black = "strong support" (>70% bootstrap support or ≥0.95 Bayesian posterior probability); dark grey = "moderate support" (50%–69% bootstrap support or 0.75–0.94 Bayesian posterior probability); light grey = "weak support" (<50% bootstrap support or 0.50–0.74 Bayesian posterior probability).

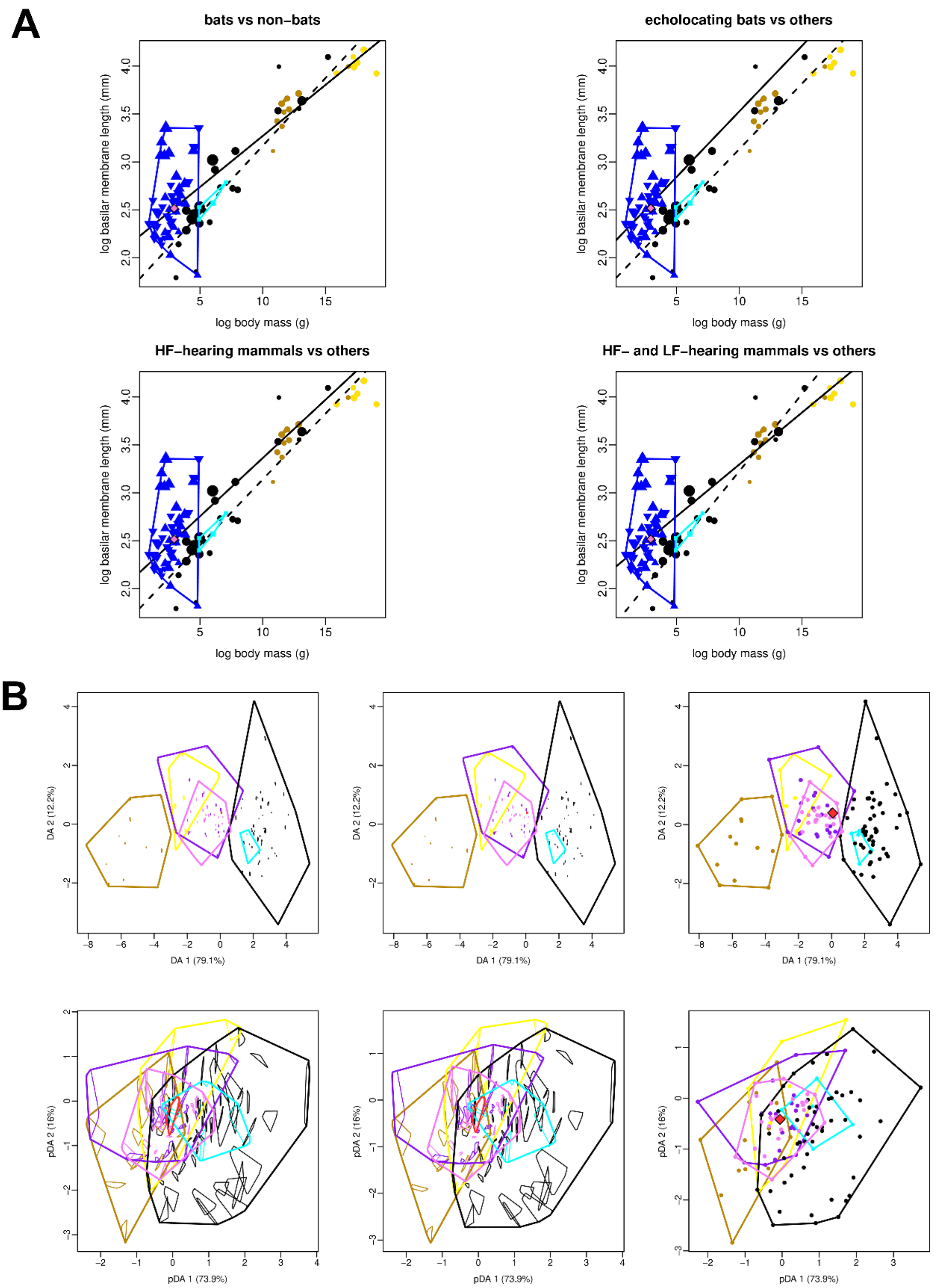

Figure S3. **Basilar membrane and semicircular canal size among placental mammals**. **Related to Figure 3, STAR Methods, and Data S1G-J, M.** Colors represent hearing abilities and/or particular groups: pink diamond, *Vielasia sigei*; aqua, non-laryngeally emitting bats (pteropodids); dark blue, laryngeally emitting bats (triangles, nasal emitters; inverted triangles, oral emitters); tan, High Frequency (HF)-hearing cetaceans; yellow, Low Frequency (LF)-hearing cetaceans; black, other placentals. (**A**) Allometric relationship of log basilar membrane length and log body mass across placental mammals, considering species with specific hearing abilities. Solid lines are the average PGLS regression line for the tested group of interest (i.e., bats, laryngeally echolocating bats, HF-hearing and HF- and LF-hearing mammals), dashed lines are the average PGLS regression lines for the remaining group (i.e., non-bats, non-laryngeally echolocating bats, non HF- and HF- and LF-hearing mammals). (**B**) Individual variation in the discriminant analyses performed on the PGLS regression residuals of each semicircular canal log size against cochlear log size. Discriminant axes percentages are average between-groups variance explained. Top panels: position of species on the two first linear discriminant analysis (LDA) axes. Bottom panels: position of species on the two first phylogenetic flexible discriminant analysis (pFDA) axes. Left panels: 'full' morphospaces showing the entire variation of each point. Centre panels: '95%' morphospaces showing variation of the 95% closest points to the whole morphospace centroid. Right panels: average position (Figure 3D).

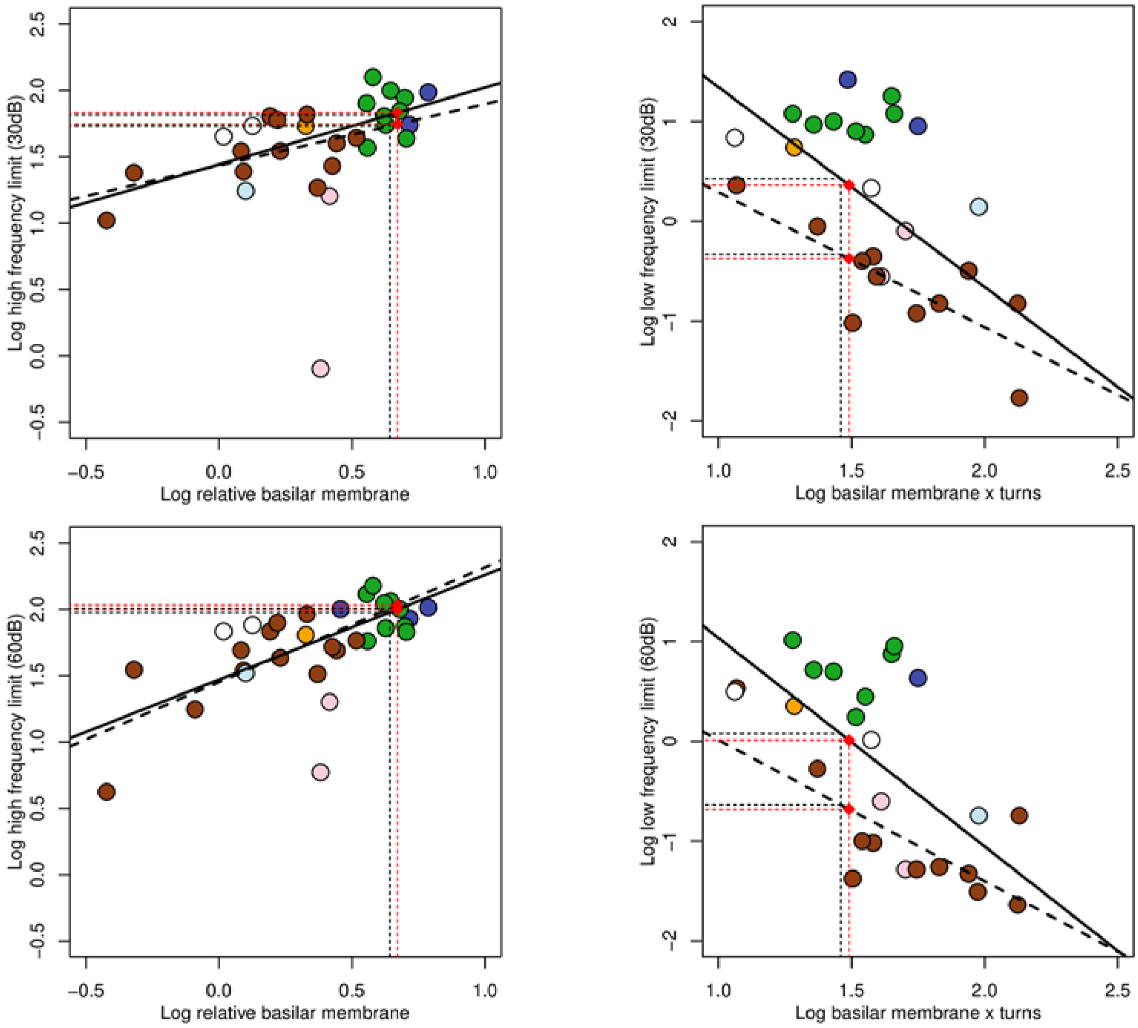

Figure S4. **Estimated hearing limits of *Vielasia sigei*. Related to STAR Methods, and Data S1K-L.** Estimated hearing limits of *V. sigei* (thin red dotted lines) and the hypothetical modern bat common ancestor (thin black dotted lines); based on ancestral reconstructions of inner ear morphology, see Davies et al.[S1] Low (left panels) and high (right panels) frequency hearing limits are reconstructed at 30 dB (top panels) and 60 dB (bottom panels) respectively using the relationships between log relative basilar membrane length (for low frequencies) or log product of basilar membrane length and cochlear turns (for high frequencies) against frequency hearing limits in extant taxa.[S1-3] Colored points: non-LE yinpterochiropterans (orange), LE yinpterochiropterans (blue), LE yangochiropterans (green), subterranean rodents (pink), semi-aquatic seals (light blue), other placental mammals (brown), and marsupials (white). OLS regression lines are shown for placental mammal species without subterranean rodents, including bats (solid thick black line) or excluding bats (dashed thick black line).

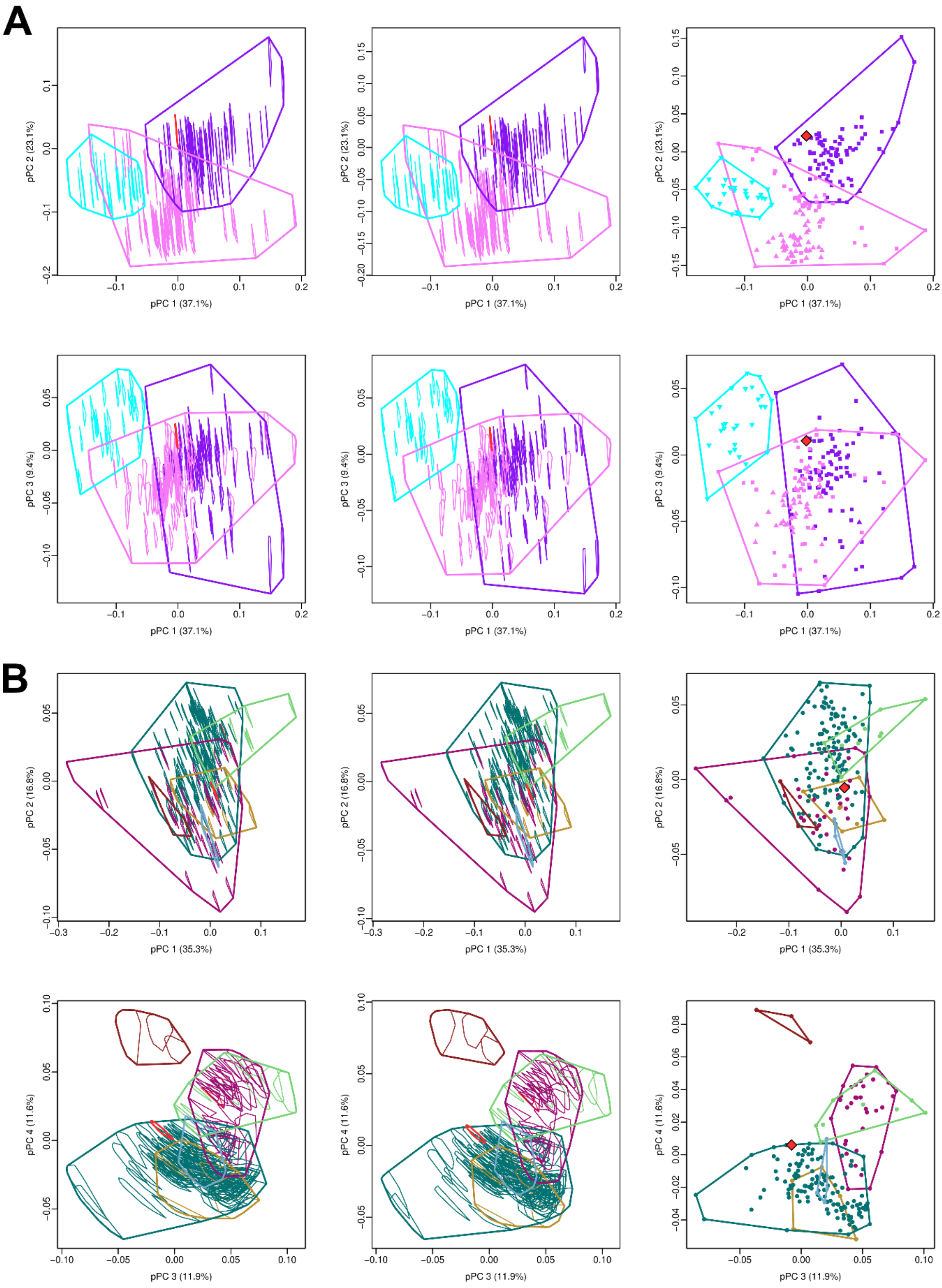

Figure S5. **Individual variation in pPCAs performed on cranium and mandible datasets. Related to Figure 4, STAR Methods, and Data S1N-P.** pPC percentages are average variance explained for each pPC axis. (**A**) Cranium, colors represent echolocation call type: aqua, non-laryngeal echolocators; pink, nasal emitters; purple, oral emitters. (**B**) Mandible, colours represent diet type: light green, nectarivore; plum, frugivore; teal, insectivore; gold, carnivore; skyblue, omnivore; rust, sanguivore. Top panels: pPC1 and pPC2. Bottom panels: pPC1 and pPC3. Left panels: 'full' morphospaces showing the entire variation of each point. Centre panels: '95%' morphosapces showing variation of the 95% closest points to the whole morphospace centroid. Right panels: average position (as shown in Figure 4A and 4B). *Vielasia sigei*'s point and convex hull are in red. Data from Arbour et al.[S4] and this paper.

SUPPLEMENTAL INFORMATION REFERENCES

S1. Davies, K.T., Maryanto, I., and Rossiter, S.J. (2013a). Evolutionary origins of ultrasonic hearing and laryngeal echolocation in bats inferred from morphological analyses of the inner ear. Front. Zool. *10*, 2. 10.1186/1742-9994-10-2.

S2. West, C.D. (1985). The relationship of the spiral turns of the cochlea and the length of the basilar membrane to the range of audible frequencies in ground dwelling mammals. J. Acoust. Soc. Am. *77*, 1091–1101. 10.1121/1.392227.

S3. Manoussaki, D., Chadwick, R.S., Ketten, D.R., Arruda, J., Dimitriadis, E.K., and O'Malley, J.T. (2008). The influence of cochlear shape on low-frequency hearing. Proc. Natl. Acad. Sci. *U.S.A. 105*, 6162–6166. 10.1073/pnas.0710037105.

S4. Arbour, J.H., Curtis, A.A., and Santana, S.E. (2019). Signatures of echolocation and dietary ecology in the adaptive evolution of skull shape in bats. Nat. Commun. *10*, 2036. 10.1038/s41467-019-09951-y.

S5. O'Leary, M.A., Bloch, J.I., Flynn, J.J., Gaudin, T.J., Giallombardo, A., Giannini, N.P., Goldberg, S.L., Kraatz, B.P., Luo, Z.-X., Meng, J., *et al*. (2013). The placental mammal ancestor and the post-K-Pg radiation of placentals. Science *339*, 662–667. 10.1126/science.1229237.

S6. Beck, R.M.D., and Lee, M.S.Y. (2014). Ancient dates or accelerated rates? Morphological clocks and the antiquity of placental mammals. Proc. R. Soc. Lond. *B* Biol. Sci. *281*, 20141278. 10.1098/rspb.2014.1278

S7. Lyson, T.R., Miller, I.M., Bercovici, A.D., Weissenburger, K., Fuentes, A.J., Clyde, W.C., Hagadorn, J.W., Butrim, M.J., Johnson, K.R., Fleming, R.F., Barclay, R.S., Maccracken, S.A., Lloyd, B., Wilson, G.P., Krause, D.W., and Chester, S.G.B. (2019). Exceptional continental record of biotic recovery after the Cretaceous–Paleogene mass extinction. Science *366*, 977–983. 10.1126/Science.Aay2268

S8. Murphey, P., Townsend, K.E., Friscia, A., Westgate, J., Evanoff, E., and Gunnell, G. (2017). Paleontology and stratigraphy of Middle Eocene rock units in the southern Green River and Uinta Basins, Wyoming and Utah. Geol. intermountain West *4*, 1–53. 10.31711/giw.v4.pp1-53

S9. Smith, K.T., Bhullar, B.-A.S., Köhler, G., and Habersetzer, J. (2018). The only known jawed vertebrate with four eyes and the bauplan of the pineal complex. Curr. Biol. *28*, 1101–1107.e1102. 10.1016/j.cub.2018.02.021

S10. Smith, M.E., Chamberlain, K.R., Singer, B.S., and Carroll, A.R. (2010). Eocene clocks agree: Coeval 40Ar/39Ar, U-Pb, and astronomical ages from the Green River Formation. Geology *38*, 527–530. 10.1130/G30630.1

S11. Musser, G., and Clarke, J.A. (2020). An exceptionally preserved specimen from the Green River Formation elucidates complex phenotypic evolution in Gruiformes and Charadriiformes. Front. Ecol. Evol. *8*, 559929. 10.3389/fevo.2020.559929

S12. Escarguel, G. (1999). Les rongeurs de l'Eocène inférieur et moyen d'Europe occidentale: systématique, phylogénie, biochronologie et paléobiogéographie des niveaux-repères MP 7 à MP 14. Palaeovertebrata 28, 89–351.

S13. Gradstein, F.M., Ogg, J.G., Schmitz, M.D., and Ogg, G.M. (eds.) (2012). The Geologic Time Scale 2012 (Elsevier).

S14. Lenz, O.K., Wilde, V., Mertz, D.F., and Riegel, W. (2015). New palynology-based astronomical and revised 40Ar/39Ar ages for the Eocene maar lake of Messel (Germany). Int. J. Earth Sci. *104*, 873–889. 10.1007/s00531-014-1126-2

S15. Solé, F., Plateau, O., Le Verger, K., and Phélizon, A. (2019). New paroxyclaenid mammals from the Early Eocene of the Paris Basin (France) shed light on the origin and evolution of these endemic European cimolestans. J. Syst. Palaeontol. *17*, 1711–1743. 10.1080/14772019.2018.1551248

S16. Smith, M.E., and Carroll, A.R., eds. (2015). Stratigraphy and Paleolimnology of the Green River Formation, Western USA (Springer Dordrecht). 10.1007/978-94-017-9906-5

S17. Smith, T., and Smith, R. (2003). Terrestrial mammals as biostratigraphic indicators in Upper Paleocene-Lower Eocene marine deposits of the southern North Sea Basin. Geol. Soc. Am. Spec. Pap. *369*, 513–520. 10.1130/0-8137-2369-8.513

S18. Hooker, J.J. (2010). The mammal fauna of the early Eocene Blackheath Formation of Abbey Wood, London. *Palaeontogr. Soc. Monogr. 165*, 1–162.

S19. Smith, T., Kumar, K., Rana, R.S., Folie, A., Solé, F., Noiret, C., Steeman, T., Sahni, A., and Rose, K.D. (2016). New early Eocene vertebrate assemblage from western India reveals a mixed fauna of European and Gondwana affinities. Geosci. Front. *7*, 969–1001. 10.1016/j.gsf.2016.05.001

S20. Kass, R.E., and Raftery, A.E. (1995). Bayes factors. *J. Am. Stat. Assoc*. *90*, 773–795. 10.1080/01621459.1995.10476572.

S21. Nylander, J.A.A., Ronquist, F., Huelsenbeck, J.P., and Nieves-Aldrey, J.L. (2004). Bayesian phylogenetic analysis of combined data. Syst. Biol. *53*, 47–67. 10.1080/10635150490264699.

S22. Ekdale, E.G. (2013). Comparative anatomy of the bony labyrinth (inner ear) of placental mammals. PLoS ONE *8*, e66624. 10.1371/journal.pone.0066624.

S23. Ekdale EG, Rowe T (2011) Morphology and variation within the bony labyrinth of zhelestids (Mammalia, Eutheria) and other therian mammals. J. Vertebr. Paleontol. *31*, 658–675. 10.1080/02724634.2011.557284

S24. Habersetzer, J., Rabenstein, R., and Gunnell, G.F. (2018). Bats – highly specialized nocturnal hunters with echolocation. In Messel – an Ancient Greenhouse Ecosystem, K.T. Smith, S.F.K. Schaal, and J. Habersetzer, eds. (Senckenberg Gesellschaft für Naturforschung), pp. 249–261.

S25. Spoor, F., and Zonneveld, F. (1998). Comparative review of the human bony labyrinth. Yrbk. Phys. Anthropol. *107*, 211–251. 10.1002/(SICI)1096-8644(1998)107:27+<211::AID-AJPA8>3.0.CO;2-V.

S26. Spoor, F., Bajpai, S., Hussaim, S.T., Kumar, K., and Thewissen, J.G.M. (2002). Vestibular evidence for the evolution of aquatic behaviour in early cetaceans. Nature *417*, 163–166. 10.1038/417163a.

S27. Cox, P.G., and Jeffery, N. (2010). Semicircular canals and agility: the influence of size and shape measures. J. Anat. *216*, 37–47. 10.1111/j.1469-7580.2009.01172.x.

S28. Davies, K.T.J., Bates, P.J.J., Maryanto, I., Cotton, J.A., and Rossiter, S.J. (2013). The evolution of bat vestibular systems in the face of potential antagonistic selection pressures for flight and echolocation. PLoS ONE *8*, e61998. 10.1371/journal.pone.0061998.

S29. Ekdale, E.G., and Racicot, R.A. (2015). Anatomical evidence for low frequency sensitivity in an archaeocete whale: comparison of the inner ear of *Zygorhiza kochii* with that of crown Mysticeti. J. Anat. *226*, 22–39. 10.1111/joa.12253.

S30. Spoor, F., Garland, T., Krovitz, G., Ryan, T.M., Silcox, M.T., and Walker, A. (2007). The primate semicircular canal system and locomotion. Proc. Natl. Acad. Sci. U.S.A. *104*, 10808–10812. 10.1073/pnas.0704250104.

S31. Spoor, F., and Thewissen, J.G.M. (2008). Comparative and functional anatomy of balance in aquatic mammals. In Sensory Evolution on the Threshold, Adaptations in Secondarily Aquatic Vertebrates, J.G.M. Thewissen, and S. Nummela, eds. (University of California Press), pp. 257–284. 10.1525/9780520934122-017.